

学位論文（要約）

Seismicity Patterns before and after the 2011 Tohoku
Earthquake in the Japan Trench Subduction Zone

（日本海溝域における
2011年東北地方太平洋沖地震前後の地震活動）

平成29年5月 博士（理学）申請

東京大学大学院理学系研究科

地球惑星科学専攻

仲谷 幸浩

学位論文（要約）

Seismicity Patterns before and after the 2011 Tohoku
Earthquake in the Japan Trench Subduction Zone

（日本海溝域における
2011年東北地方太平洋沖地震前後の地震活動）

平成29年5月 博士（理学）申請

東京大学大学院理学系研究科

地球惑星科学専攻

仲谷 幸浩

Abstract

The 2011 off the Pacific coast of Tohoku Earthquake (the Tohoku earthquake) occurred on March 11, 2011 in the Japan Trench subduction zone with a moment magnitude of 9.0, which was the largest earthquake ever recorded in Japan. Many studies using various types of data, such as teleseismic, geodetic, strong motion, and tsunami data, have proposed generally common source rupture models characterized by a large coseismic slip along an up-dip part of the plate interface and high-frequency ruptures along its down-dip edge. Both onshore and offshore seismic observation data before and after the Tohoku earthquake are available in and around its source area. However, most of previous studies of local seismicity using ocean bottom seismometer data have often focused only on manual relocation of hypocenters listed in the existing earthquake catalogs. Therefore, the location and frequency of offshore earthquakes with small magnitudes have yet to be elucidated especially after the Tohoku earthquake. Such less complete earthquake catalogs need to be improved to discuss frequency-magnitude distributions (FMDs) and the b -value of the Gutenberg-Richter law (G-R law) which is considered to be related to the differential stress. This thesis contributes to understanding the spatiotemporal variations of the FMD in the Japan Trench subduction zone before and after the occurrence of the Tohoku earthquake and to discussion on possible physical properties that cause such variations.

First of all, I developed an automated method for detection and location of local earthquakes including small-magnitude ones. The method is composed of the amplitude-based trigger algorithm and the waveform coherence analysis. I applied the method to onshore and offshore seismic data in the Japan Trench subduction zone

before and after the 2011 Tohoku earthquake and extracted hypocenters as seismic sources of energy release. As a result of application of the newly developed method, I obtained a more complete earthquake catalog whose magnitudes of completeness (M_c) for the pre- and post-Tohoku periods are approximately 2 and 3, respectively, as being derived as minimum magnitudes which can maximize the goodness of fitting test assuming the G-R law within the magnitude range of M_c and above. The resulting detection rate in comparison to a conventional detection and location system is high even for the period immediately after the Tohoku earthquake. Focal depths are constrained around the plate interface and the error of epicenters is about 20 km estimated by comparison to the existing catalog and by experiments using synthetic seismic wavelets.

For the pre-Tohoku period, from October 2007 to June 2008, the results show seismicity boundary along 39°N. Locations of the low seismicity are in agreement with that of the aseismic area where the presence of fluid along the plate interface has been suggested by previous studies. In contrast, the seismic area is observed just south of the aseismic area around 39°N, corresponding to the down-dip side of the coseismic slip zone of the Tohoku earthquake. For the post-Tohoku period, first three months after the Tohoku earthquake, the resulting number of earthquakes is about 1.8 times as many as that of the Japan Meteorological Agency (JMA) catalog data within a band of 5 km on both sides (above and below) of the plate interface. The seismicity distribution shows coincidence between low-seismicity area and the coseismic slip zone, except near the Japan Trench. This relationship is also identified by negative correlation between the cumulative seismic moment release and the amount of coseismic slip. On the other hand, active aftershock clusters are located along the down-dip edge of the coseismic rupture region. It is one of the important contributions of this thesis to constraining the extent of

the source area of the Tohoku earthquake in terms of seismicity and indicating the stress increase in its surrounding area.

Finally, I investigated the spatiotemporal variations of FMDs before and after the Tohoku earthquake. The remarkable result is that the b -value, which is the relative amount of small to large earthquakes, is low in wide areas corresponding to low M_c immediately after the Tohoku earthquake, comparing to the previous study using the JMA catalog data. Under the assumption that the frequency of earthquakes is characterized by the G-R law and the magnitude-dependent detection rate, the statistical analysis shows that the breakdown of the G-R law occurs in these areas for the post-Tohoku period. The deviation from the G-R law is confirmed in the magnitude range greater than ~ 4 , where the observed cumulative number of earthquakes shapes a convex curve. This thesis first reveals such breakdown of the G-R law for aftershocks of the 2011 Tohoku earthquake by including small-magnitude offshore earthquakes. In the area that experienced high frequency radiation at the coseismic slip, a substantial decrease in the b -value from 1.16 to 0.64 is observed from before to after the Tohoku earthquake. Such change in the fraction of earthquakes with a magnitude of ~ 2 might be occurred due to changes in the stress field and/or frictional properties along the plate interface. The areas adjacent to the northern and southern limits of the coseismic slip zone show low b -value for the post-Tohoku period or decrease in the b -value from before to after the Tohoku earthquake. Such feature can be explained by increase of differential stress originated from the main shock in its surrounding area. This thesis revealed the regionalities of the FMDs using entire range of magnitudes, and the results provide constraints on relationship between the FMDs and source region and its rupture process of the 2011 Tohoku earthquake.

Contents

1. General Introduction	1
2. Data and Array Configuration.....	9
2.1 Data.....	9
2.2 Study Region and Observation Period	11
3. Detection and Location Method.....	29
3.1 Introduction	29
3.2 Overview of Detection and Location Scheme.....	32
3.3 Event Detection Process by STA/LTA Algorithm	33
3.4 Semblance Calculation and Source Extraction Processes	35
3.5 Synthetic Tests.....	39
3.6 Magnitude Determination and Correction.....	42
4. Seismicity before and after the 2011 Tohoku Earthquake	75
4.1 Newly Obtained Earthquake Catalog	75
4.2 Comparison of Earthquake Catalog with Previous Studies.....	77
4.3 Seismicity for the pre-Tohoku Period.....	83
4.4 Seismicity for the post-Tohoku Period	85
5. Frequency-Magnitude Relation of Seismicity	109
5.1 Review of Previous Studies.....	109
5.2 Frequency-Magnitude Distribution and the <i>b</i> -value.....	112
5.3 Statistical Evaluation of Frequency-Magnitude Distribution.....	116

6. General Discussion	131
6.1 Spatiotemporal Variation of Frequency-Magnitude Distribution	131
6.2 Future Studies	134
7. Conclusions	141
Acknowledgments.....	143
References	145

1. General Introduction

The Japan Trench subduction zone is one of the most seismically active regions in the world. The Pacific plate is subducting beneath the northeastern Japan at a convergence rate of approximately 8–9 cm/year [DeMets *et al.*, 1994], and seismicity around the plate interface has been active [e.g., Igarashi *et al.*, 2001]. Under such tectonic and seismic environments, the 2011 off the Pacific coast of Tohoku Earthquake (hereafter, the 2011 Tohoku earthquake) occurred on March 11, 2011 with a moment magnitude (M_w) of 9.0, which was the largest earthquake ever recorded by modern instruments in Japan. Figure 1.1 shows seismic and tectonic environments of the Japan Trench subduction zone. Due to the availability of dense onshore seismic and geodetic data and developments of seafloor observation instruments, a number of studies have reported on various aspects of the 2011 Tohoku earthquake.

Ide *et al.* [2011] inverted teleseismic waveform data of the main shock at Global Seismographic Network stations, and first suggested that its rupture process is characterized by two modes; a large coseismic slip along a shallow part of the plate interface and high-frequency ruptures along the down-dip edge. Many other studies using various types of data, such as strong motion data, geodetic data, tsunami waveform data, and their combined data [e.g., Yoshida *et al.*, 2011; Iinuma *et al.*, 2012; Satake *et al.*, 2013; Yokota *et al.*, 2011], also proposed that the source rupture models share common features. In particular, Iinuma *et al.* [2012] incorporated onshore Global Navigation Satellite System (GNSS) observations and all available seafloor geodetic data, including the observed horizontal and vertical seafloor coseismic displacements [Sato *et al.*, 2011], into inversion analysis and derived the coseismic slip with high

spatial resolution even at the shallow part of the plate interface (Figure 1.1). Their accurate results revealed that more than 50-m slip occurred near the Japan Trench. Bathymetry differences before and after the Tohoku earthquake, which were derived from multibeam surveys across the trench and a 3-D elastic finite element model, also confirmed such a large slip during the main shock [Sun *et al.*, 2017; Fujiwara *et al.*, 2011].

After the occurrence of the 2011 Tohoku earthquake with such an anomalously large slip, static stress changes in and around the source region have been estimated by stress tensor inversions and tests of the Coulomb failure hypothesis using focal mechanisms of earthquakes [e.g., Hasegawa *et al.*, 2011; Toda *et al.*, 2011] and that changes are important factors to trigger subsequent aftershocks [e.g., Das and Henry, 2003]. Here I introduce several previous studies associated with aftershock activities of the Tohoku earthquake. Asano *et al.* [2011] discussed stress release and concentration originated from the main shock by determining focal mechanisms of earthquakes from 2003 to two months after the Tohoku earthquake off northeastern Japan. They estimated centroid moment tensors (CMTs) of the earthquakes by using onshore broadband seismometer data, and examined spatiotemporal variations of the CMTs of interplate and intraplate earthquakes. Kato and Igarashi [2012] investigated the spatial distribution of the 1-year middle-sized aftershock sequences ($M > 4$) in and around the source region, particularly focusing on the interplate type earthquakes. Nakamura *et al.* [2016] classified small earthquakes ($M > 3$) into normal, thrust, interplate, strike-slip, and other faulting types based on cross-correlation coefficients of the waveforms and 3-D rotation of the focal mechanisms [Kagan, 1991a] by referring to events from the existing catalogs of repeating earthquakes and focal mechanism data from 1984 to 2013 in the Japan Trench subduction zone. These previous studies share results in which active

normal faulting aftershocks were mainly observed in the hanging wall and near the trench axis, thrust faulting events occurred within the subducting slab in the down-dip region, and few interplate events were detected in the large coseismic slip zone, while interplate earthquakes were dominant for the period before the Tohoku earthquake. Such activities reflected the stress drop in the source region and change in the stress regime in the Japan Trench subduction zone before and after the Tohoku earthquake.

In addition to the above onshore-based seismic observations, seafloor aftershock observations have been extensively conducted in and around the source region [Shinohara *et al.*, 2011, 2012; Obana *et al.*, 2012, 2013]. These experiments contributed to precisely locating hypocenters of aftershocks because of sufficient station coverage in the offshore region. Shinohara *et al.* [2011, 2012] relocated events in the Japan Meteorological Agency (JMA) earthquake catalog with high spatial resolution (< 5 km along horizontal direction and < 3 km along depth) by measuring *P*- and *S*-wave arrival times on waveforms recorded by ocean bottom seismometers (OBSs). Shinohara *et al.* [2011] determined the initial hypocenters by the maximum-likelihood estimate algorithm with a Bayesian approach [Hirata and Matsu'ura, 1987] and a 1-D velocity structure, and then relocated them by the double-difference method [Waldhauser and Ellsworth, 2000] in order to improve the accuracy of relative locations of hypocenters. Suzuki *et al.* [2012] carried out a similar approach to relocate earthquakes for a sequence of foreshocks, the main shock, and aftershocks of the 2011 Tohoku earthquake using OBSs deployed off Miyagi. Although such OBS observations of local earthquakes have been conducted over the past decades and a large number of results have been obtained from them, most of the previous studies of seismicity using OBS data have focused only on relocation of hypocenters listed in the existing earthquake catalogs. In other words, previous studies have often circumvented identification of earthquakes that

are not listed in the catalogs due to the high background noise originated from continual occurrence of earthquakes and the manual detection methods over continuous seismic waveforms. Recent methods of automatic detection and location of seismic activities associated with the 2011 Tohoku earthquake should be applied so as to take advantage of using OBSs that can record small offshore earthquakes which are not listed in the existing catalogs. Such a more complete catalog including small earthquakes can contribute to determining the frequency-magnitude distribution of earthquakes whose slope is considered to be negatively correlated to differential stress [e.g., Scholz, 2015] and to constraining the stress release/redistribution caused by the large coseismic slip.

Next, I also describe seismicity results for the period prior to the Tohoku earthquake. Earthquake activities in the Japan Trench subduction zone have been high even for the pre-Tohoku period as stated above. The characteristic spatial distribution of seismicity patterns has also been observed by both onshore and offshore seismic observations [e.g., Igarashi *et al.*, 2001; Nishizawa *et al.*, 1992]. Fujie *et al.* [2002] first revealed negative correlation between seismicity around 39°N and intensity of the plate interface reflections by a seismic survey off Sanriku in 1996 along a profile, and suggested that such aseismic region of strong anti-correlation between seismicity and intense *PP* reflection is related to the existence of fluid along the plate interface. Mochizuki *et al.* [2005] conducted an additional seismic survey in 2001 in the same region and confirmed that such correlation holds true for several along-strike profiles indicating spatially distribution of fluid along the plate interface (Figure 1.1). Therefore, the fluid migration along the plate interface may be characterized by examining persistence of low seismicity region even after the occurrence of the 2011 Tohoku earthquake.

On the basis of these backgrounds, I placed the following four objectives of this

study. The first objective is to detect and locate earthquakes including small offshore ones using both onshore and offshore seismic data. The second objective is to reveal spatiotemporal patterns of seismicity around the plate interface before and after the 2011 Tohoku earthquake. The third and the final fourth objectives are to obtain a more complete earthquake catalog from the above results and to elucidate its characteristics of frequency-magnitude relation.

In Chapter 2, I describe the seismic observation data used in this study, especially detailing three seafloor observations including their observation periods. There exist only few studies which have conducted such an extensive seismicity analysis using both onshore and offshore seismic waveform data. This chapter also contains settings of detection and location method specified in the following chapter.

In Chapter 3, I first provide a brief overview of previously developed approaches for detection and location of earthquakes. Then, I introduce an automated method to detect and locate earthquakes including small ones, originally proposed by Nakatani *et al.* [2015]. This method employs the array-based waveform stacking technique so as to deal with high seismic activities just after the 2011 Tohoku earthquake and to illuminate seismic sources of energy release. Magnitude determination and correction processes are also included in the method of this study. In order to evaluate the accuracy of hypocenters, I perform experiments using synthetic seismic wavelets and actual station coverage.

In Chapter 4, I explain a new catalog of earthquakes detected by applying the method as described in Chapter 3 to the continuous waveform data before and after the 2011 Tohoku earthquake. Characteristics of the catalog is described in comparison with that of the previous studies. On the basis of this new earthquake catalog, I discuss seismicity results with regard to spatiotemporal variations of earthquake frequency,

temporal changes in the cumulative number of earthquakes, and the cumulative seismic moment release.

In Chapter 5, the resultant seismicity is characterized in terms of frequency-magnitude relation. First, I review conventional approaches for interpreting frequency-magnitude distribution. Then, differences in the parameters of the frequency-magnitude distribution between this study and the previous studies are discussed. Finally, quantitative evaluation of the frequency-magnitude distributions is conducted through introduction of the statistical model, and the differences between the observed and the modeled frequency of earthquakes are quantitatively described.

In Chapter 6, I discuss the spatial variations of the frequency-magnitude distribution of earthquakes according to the results of Chapter 5. In addition, its temporal change from before to after the 2011 Tohoku earthquake is also investigated. Relationship between these characteristics of the frequency-magnitude relation and other seismological information, such as the co- and post-seismic slip zones of the 2011 Tohoku earthquake, and seismic structure around the plate interface are examined. Ongoing and future studies are also included in this chapter.

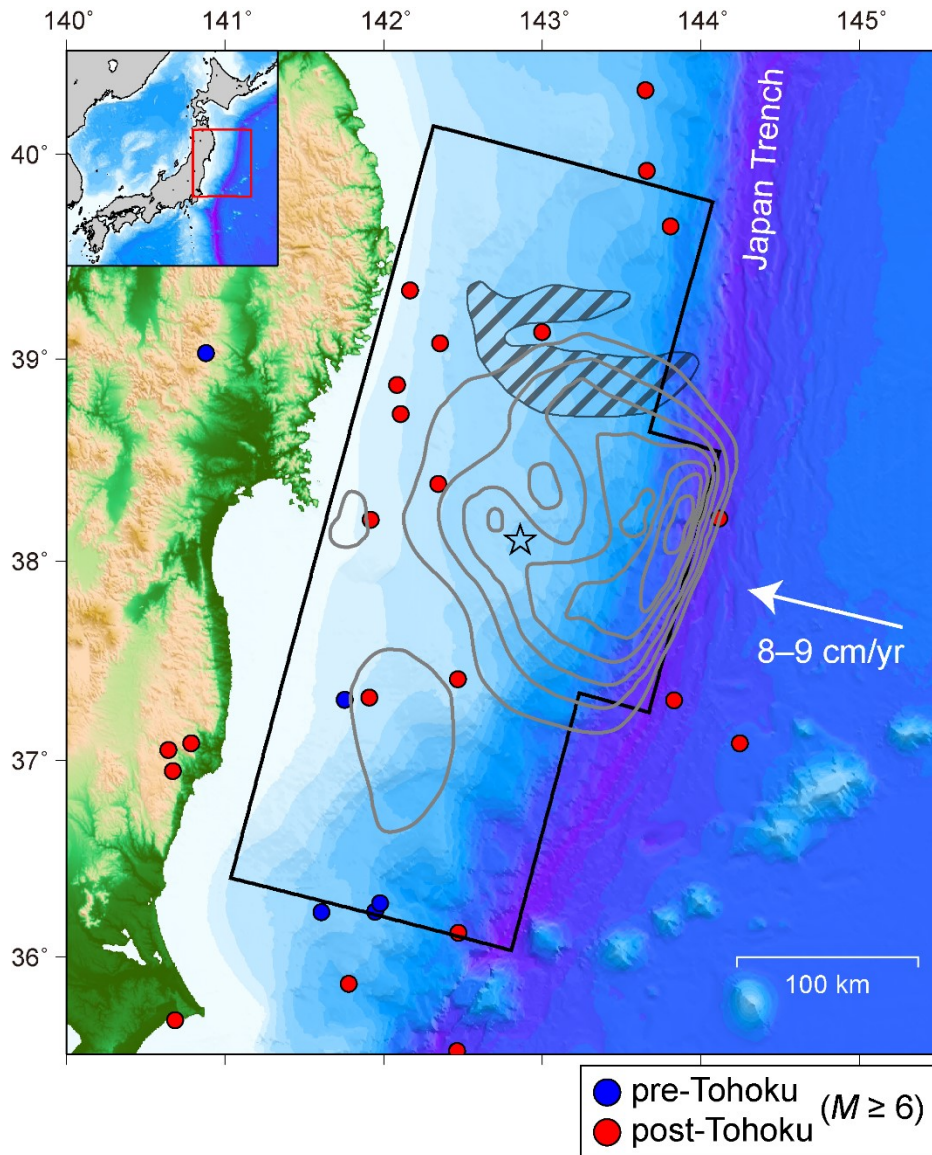


Figure 1.1. Tectonic and seismic features in the Japan Trench subduction zone and the study region (black). The white arrow shows the direction of subduction of the Pacific plate. Gray contours show the coseismic slip distribution of the 2011 Tohoku earthquake (outermost contour, 10 m; interval, 10 m) [Iinuma *et al.*, 2012]. The star indicates its epicenter. A hatching area denotes aseismic region described in Mochizuki *et al.* [2005]. Red and blue circles are epicenters of earthquakes with magnitudes larger than 6 determined by JMA during the observation periods before (10/16/2007–06/17/2008) and after (03/20/2011–06/06/2011) the Tohoku earthquake, respectively. A red rectangle in the inset shows the region corresponding to the main panel.

2. Data and Array Configuration

In this chapter, I describe the seismic observation data used in this study and the array configurations including both onshore and offshore stations within the study region for detection and location of earthquakes using an array technique.

2.1 Data

In this study, I used both onshore and offshore seismic waveform data. The onshore seismograph network, Hi-net [Okada *et al.*, 2004], is operated by National Research Institute for Earth Science and Disaster Resilience (NIED). Each seismic station consists of three-component velocity sensors with a natural frequency of 1 Hz and a sampling rate of 100 Hz (red squares in Figures 2.1–2.3).

The offshore seismic data was collected during several temporary observations using pop-up type OBSs. For the period of analysis before the 2011 Tohoku earthquake, from October 2007 to June 2008, I used a set of OBS data off Sanriku from the Japan and Kuril Trenches observation project (1-Hz velocity sensors with 200-Hz sampling rate) [e.g., Yamada *et al.*, 2009], and data from recurrent seafloor observations off Miyagi (1-Hz velocity sensors with 200-Hz sampling rate). Those OBS stations are shown in Figure 2.1 by orange hexagons and blue squares, respectively.

The period after the occurrence of the 2011 Tohoku earthquake is further divided into two sub-periods. The first sub-period spanned from late March 2011 to middle April 2011, and the second sub-period from late April 2011 to early June 2011. For both sub-periods, I made use of the OBS data acquired by extensive seafloor aftershock observations [Shinohara *et al.*, 2011, 2012] in addition to the recurrent OBS

observations off Miyagi. Most of these OBSs were equipped with 4.5-Hz velocity sensors, and data from the aftershock observations were sampled at 100, 128 or 200 Hz, whereas those from the recurrent observations off Miyagi were sampled at 100 or 125 Hz (Table 2.1). The OBS stations for the aftershock observations are shown by orange hexagons as well as those for the recurrent observations off Miyagi shown by blue squares in Figures 2.2 and 2.3. All of the above OBSs have three components and recorded continuous waveform data at station intervals of about 20–25 km. The detailed information of each station is compiled in Table 2.1.

2.2 Study Region and Observation Period

As I will discuss in the next chapter, this study employs an array technique for seismicity analyses. The target region is in and around the large coseismic slip zone of the Tohoku earthquake [Iinuma *et al.*, 2012]. In order to detect and precisely locate earthquakes in the offshore region, the number of OBS stations should be sufficiently large because determination of hypocenters in this study is via waveform stacking among the stations. On the other hand, each size of the array should be similarly dimensioned and be limited because waveform coherence among the stations is a critical factor for hypocenter determination. From the distribution configuration of all the OBS stations, I required the number of OBS stations in each array to be at least 15. This number was arbitrarily selected based on the comparable number of stations in Nakatani *et al.* [2015] which performed a seismicity analysis using OBS data employing almost the same technique, although the station interval is shorter than that of this study. After all, I divided the study region into three (Regions 1, 3, and 5, color solid rectangles in Figures 2.1–2.3). Each set of arrays consists of stations within the respective region and a few of those in the adjacent regions. I also considered two additional regions (Regions 2 and 4, color dashed rectangles in Figures 2.1–2.3) each of which covers the halves of mutually neighboring regions in order to evaluate robustness of results about a choice of a target region for analyses; putting boundaries may introduce considerable artifacts from the boundary effect.

For the arrays as defined above, I finally determined periods of analysis based on the availability of observation data (Figures 2.4 and 2.5). The average periods are about six months in 2007–2008, and about two months immediately after the 2011 Tohoku earthquake.

Table 2.1. Information of the stations used in this study for (a) the pre-Tohoku period, (b) the first, and (c) the second sub-periods of aftershock observations of the 2011 Tohoku earthquake. All the stations of each observation are listed from north to south.

(a) Station	Longitude	Latitude	Height (m)	Sampling Rate [Hz]	Natural Frequency [Hz]
ML46	142.75795	39.99858	-1081	200	1.0
ML30	143.33422	39.88103	-1748	200	1.0
ML38	143.07306	39.87100	-1426	200	1.0
ML07	143.73397	39.84925	-3004	200	1.0
ML19	143.52286	39.77399	-2162	200	1.0
ML45	142.77311	39.75215	-1069	200	1.0
ML29	143.31113	39.70196	-2188	200	1.0
ML06	143.71219	39.67133	-2879	200	1.0
ML37	143.04521	39.64879	-1656	200	1.0
ML18	143.49898	39.59571	-2605	200	1.0
ML44	142.77345	39.55344	-1334	200	1.0
ML28	143.28816	39.52296	-2169	200	1.0
ML49	142.50889	39.45955	-1012	200	1.0
ML36	143.01606	39.42412	-1833	200	1.0
ML17	143.47704	39.41719	-2950	200	1.0
ML27	143.26595	39.34319	-2022	200	1.0
ML43	142.74444	39.32874	-1602	200	1.0
ML04	143.66678	39.31395	-3253	200	1.0
ML16	143.45411	39.23870	-2698	200	1.0
ML03	143.64588	39.13406	-3622	200	1.0
ML42	142.71583	39.10526	-1226	200	1.0
ML15	143.43210	39.06046	-2692	200	1.0
ML48	142.45300	39.01280	-1135	200	1.0
ML26	143.22014	38.98578	-2212	200	1.0
ML35	142.96023	38.97665	-1493	200	1.0
ML02	143.62222	38.95492	-2870	200	1.0
ML41	142.68897	38.88220	-1251	200	1.0
ML14	143.41011	38.87985	-2320	200	1.0

ML25	143.19820	38.80710	-2007	200	1.0
ML47	142.42500	38.78930	-1029	200	1.0
ML34	142.93228	38.75444	-1540	200	1.0
ML13	143.38700	38.70086	-2216	200	1.0
ML40	142.66016	38.66017	-1285	200	1.0
ML24	143.17524	38.62809	-2166	200	1.0
ML33	142.90530	38.53125	-1557	200	1.0
ML12	143.36514	38.52296	-2407	200	1.0
ML23	143.15429	38.44994	-2390	200	1.0
ML11	143.34351	38.34675	-2827	200	1.0
ML32	142.87730	38.30732	-1352	200	1.0
ML01	143.53249	38.23712	-3323	200	1.0
ML10	143.36155	38.04252	-3460	200	1.0
ML22	143.08381	37.91221	-2099	200	1.0
LS02b	142.51572	38.91491	-1207	200	1.0
S04a	142.49842	38.49940	-1130	200	1.0
LS04b	142.69962	38.29794	-1411	200	1.0
S09	143.13472	38.19884	-2062	200	1.0
S03	142.40135	38.18443	-1058	200	1.0
S08a	142.75053	38.13524	-1531	200	1.0
S07a	142.79823	37.89967	-1320	200	1.0
N.KJSH	141.71200	40.08610	139	100	1.0
N.KZMH	141.54920	39.93980	469	100	1.0
N.IWZH	141.65200	39.80200	209	100	1.0
N.TROH	141.90870	39.74350	98	100	1.0
N.KANH	141.59770	39.64420	201	100	1.0
N.YMDH	141.93360	39.47340	-88	100	1.0
N.KASH	141.67750	39.46300	451	100	1.0
N.KMIH	141.82330	39.27410	-61	100	1.0
N.SMTH	141.39090	39.18090	513	100	1.0
N.RZTH	141.53200	39.03070	-22	100	1.0
N.KKWH	141.63770	38.92070	-38	100	1.0
N.FSWH	141.35120	38.86540	18	100	1.0
N.TOWH	141.32540	38.78600	-66	100	1.0
N.SZGH	141.44280	38.64160	-85	100	1.0
N.TAJH	141.07100	38.59070	-81	100	1.0

N.KAKH	141.34210	38.51580	-202	100	1.0
N.SNDH	140.99690	38.24000	-1198	100	1.0
N.KWSH	140.64050	38.18020	43	100	1.0
N.IWNH	140.84410	38.11330	-91	100	1.0
N.SISH	140.60270	38.00910	29	100	1.0
N.YMMH	140.89240	37.94110	-188	100	1.0

(b) Station	Longitude	Latitude	Height (m)	Sampling Rate [Hz]	Natural Frequency [Hz]
A01a	142.46508	39.92796	-702	100	4.5
A04a	143.28679	39.75599	-2096	100	4.5
A05	143.55984	39.69780	-2378	100	4.5
B02a	142.66111	39.65449	-907	100	4.5
B03a	142.93577	39.59786	-1548	100	4.5
C01a	142.30983	39.49411	-571	100	4.5
B05a	143.48286	39.48097	-2872	100	4.5
C03a	142.85852	39.38001	-1677	100	4.5
C04a	143.13194	39.32261	-1893	100	4.5
C05a	143.40497	39.26374	-2385	100	4.5
D03a	142.78101	39.16398	-1548	100	4.5
D04a	143.05487	39.10562	-1880	100	4.5
E02a	142.43051	39.00329	-1100	100	4.5
E04a	142.97894	38.88943	-1510	100	4.5
E06a	143.52368	38.77117	-2667	100	4.5
F03a	142.62922	38.72937	-1256	100	4.5
F06a	143.44829	38.55506	-2500	100	4.5
NS10	143.04949	38.50159	-2017	100	4.5
G05a	143.09990	38.39743	-2167	100	4.5
NS18	143.29836	38.31811	-2746	100	4.5
NS08	142.74818	38.13540	-1498	100	4.5
I06	143.22143	37.89517	-2658	128	4.5
J03	142.32618	37.85505	-892	128	4.5
J04	142.59241	37.77355	-1203	128	4.5
J06	143.14963	37.68654	-3259	128	4.5

K04	142.52921	37.58644	-1359	200	1.0
K05	142.80277	37.52852	-2443	128	4.5
K07	143.34871	37.40921	-5160	128	4.5
L04	142.44990	37.34882	-1018	128	4.5
L05	142.72988	37.31188	-2719	128	4.5
L06	143.00319	37.25183	-4431	128	4.5
M06	142.92956	37.00347	-4987	200	4.5
N04	142.31042	36.93500	-2664	200	4.5
N05	142.60881	36.91079	-3947	200	4.5
O04a	142.24049	36.71794	-2474	128	4.5
O05a	142.51715	36.65867	-4678	200	4.5
P03a	141.89327	36.55858	-2334	200	4.5
P05a	142.41760	36.40627	-3824	128	4.5
Q02a	141.54755	36.39796	-1706	128	4.5
Q03a	141.82151	36.34117	-2068	200	4.5
LS02	142.49997	38.91679	-1194	125	4.5
LS03	142.83307	38.76621	-1403	125	4.5
LS01a	142.46059	38.68408	-1112	125	4.5
S27	142.15009	38.60032	-545	125	4.5
S14a	142.74570	38.51379	-1459	125	4.5
S04	142.50041	38.50208	-1100	125	4.5
S21	142.00192	38.43190	-358	125	4.5
S01	142.11688	38.35023	-524	125	4.5
S15a	142.92760	38.31377	-1454	125	4.5
LS04	142.69956	38.29971	-1409	125	4.5
S22	141.98375	38.22922	-299	125	4.5
TO1	143.65558	38.21309	-4147	100	4.5
S09	143.13214	38.19742	-2041	100	4.5
S03a	142.39969	38.18343	-1052	125	4.5
S03b	142.39992	38.18211	-1056	125	4.5
S02	142.08274	37.98356	-538	125	4.5
N.IWZH	141.65200	39.80200	209	100	1.0
N.TROH	141.90870	39.74350	98	100	1.0
N.KANH	141.59770	39.64420	201	100	1.0
N.YMDH	141.93360	39.47340	-88	100	1.0
N.KASH	141.67750	39.46300	451	100	1.0

N.KMIH	141.82330	39.27410	-61	100	1.0
N.RZTH	141.53200	39.03070	-22	100	1.0
N.KKWH	141.63770	38.92070	-38	100	1.0
N.FSWH	141.35120	38.86540	18	100	1.0
N.TOWH	141.32540	38.78600	-66	100	1.0
N.KAKH	141.34210	38.51580	-202	100	1.0
N.KWSH	140.64050	38.18020	43	100	1.0
N.IWNH	140.84410	38.11330	-91	100	1.0
N.SISH	140.60270	38.00910	29	100	1.0
N.YMMH	140.89240	37.94110	-188	100	1.0
N.KMAH	140.59740	37.66360	104	100	1.0
N.MRUH	140.53800	37.48940	309	100	1.0
N.MKJH	140.72270	37.47030	408	100	1.0
N.KRYH	140.42640	37.35300	59	100	1.0
N.HTAH	140.57030	37.21690	364	100	1.0
N.YBKH	140.33860	37.20060	169	100	1.0
N.IWEH	140.97020	37.02640	-145	100	1.0
N.IWWH	140.58530	36.99510	474	100	1.0
N.KIBH	140.65440	36.88080	298	100	1.0
N.DGOH	140.31810	36.83690	8	100	1.0
N.THGH	140.57500	36.79550	404	100	1.0
N.JUOH	140.54840	36.69220	228	100	1.0
N.YMAH	140.39760	36.64050	-212	100	1.0

(c) Station	Longitude	Latitude	Height (m)	Sampling Rate [Hz]	Natural Frequency [Hz]
A01b	142.46706	39.92722	-715	100	4.5
A04b	143.28865	39.75620	-2082	100	4.5
B02b	142.66340	39.65338	-920	100	4.5
B03b	142.93820	39.59766	-1559	100	4.5
C01b	142.30937	39.49453	-587	100	4.5
B05b	143.48108	39.48042	-2875	100	4.5
C03b	142.85999	39.38160	-1682	100	4.5
C04b	143.13031	39.32372	-1906	100	4.5

C05b	143.40633	39.26314	-2374	100	4.5
D03b	142.78207	39.16460	-1536	100	4.5
D04b	143.05543	39.10694	-1877	100	4.5
D05	143.32938	39.04744	-2446	100	4.5
E02b	142.43030	39.00438	-1104	100	4.5
E04b	142.97814	38.88869	-1524	100	4.5
E05	143.25026	38.82947	-2219	100	4.5
E06b	143.52183	38.76981	-2564	100	4.5
F03b	142.62951	38.72822	-1256	100	4.5
F06b	143.45516	38.55531	-2546	100	4.5
G05b	143.09991	38.39402	-2151	100	4.5
I06	143.22143	37.89517	-2658	128	4.5
J03	142.32618	37.85505	-892	128	4.5
JI05	142.89841	37.81317	-1617	100	4.5
J04	142.59241	37.77355	-1203	128	4.5
K02	141.98004	37.70337	-481	100	4.5
J06	143.14963	37.68654	-3259	128	4.5
K04	142.52921	37.58644	-1359	200	1.0
K05	142.80277	37.52852	-2443	128	4.5
L02	141.95070	37.47461	-513	100	4.5
L03	142.18036	37.42631	-871	100	4.5
K07	143.34871	37.40921	-5160	128	4.5
L04	142.44990	37.34882	-1018	128	4.5
L05	142.72988	37.31188	-2719	128	4.5
L06	143.00319	37.25183	-4431	128	4.5
M03	142.06708	37.15136	-1263	100	4.5
N02	141.76153	37.04886	-579	100	4.5
M06	142.92956	37.00347	-4987	200	4.5
N04	142.31042	36.93500	-2664	200	4.5
N05	142.60881	36.91079	-3947	200	4.5
O02	141.69060	36.83122	-932	100	4.5
O03	141.96740	36.77450	-2438	100	4.5
O04b	142.24160	36.71955	-2496	100	4.5
P01	141.35847	36.67097	-509	100	4.5
O05b	142.51635	36.66061	-4710	100	4.5
P02	141.61912	36.61397	-1557	100	4.5

P03b	141.89383	36.55777	-2344	100	4.5
Q01	141.30505	36.50642	-858	100	4.5
P05b	142.41618	36.41055	-3778	100	4.5
Q02b	141.54652	36.39920	-1718	100	4.5
Q03b	141.82190	36.34087	-2106	100	4.5
Q04	142.09668	36.28237	-3634	100	4.5
Q05	142.37482	36.22722	-4919	100	4.5
LS02	142.49997	38.91679	-1194	125	4.5
LS03	142.83307	38.76621	-1403	125	4.5
LS01b	142.45476	38.68424	-1112	125	4.5
S27	142.15009	38.60032	-545	125	4.5
S17	143.24493	38.56303	-2269	125	4.5
S14a	142.74570	38.51379	-1459	125	4.5
S14b	142.74216	38.50967	-1460	125	4.5
S10b	143.03125	38.50277	-1972	125	4.5
S04	142.50041	38.50208	-1100	125	4.5
S21	142.00192	38.43190	-358	125	4.5
S01	142.11688	38.35023	-524	125	4.5
S18b	143.29845	38.31734	-2778	125	4.5
S15a	142.92760	38.31377	-1454	125	4.5
S15b	142.92552	38.31189	-1457	125	4.5
LS04	142.69956	38.29971	-1409	125	4.5
S22	141.98375	38.22922	-299	125	4.5
TO1	143.65558	38.21309	-4147	100	4.5
BT2	143.78852	38.20950	-5760	100	4.5
BT1	143.65982	38.20875	-4130	100	4.5
S09	143.13214	38.19742	-2041	100	4.5
S03b	142.39992	38.18211	-1056	125	4.5
S08	142.75024	38.13280	-1528	125	4.5
S02	142.08274	37.98356	-538	125	4.5
N.IWZH	141.65200	39.80200	209	100	1.0
N.TROH	141.90870	39.74350	98	100	1.0
N.KANH	141.59770	39.64420	201	100	1.0
N.YMDH	141.93360	39.47340	-88	100	1.0
N.KASH	141.67750	39.46300	451	100	1.0
N.KMIH	141.82330	39.27410	-61	100	1.0

N.RZTH	141.53200	39.03070	-22	100	1.0
N.KKWH	141.63770	38.92070	-38	100	1.0
N.FSWH	141.35120	38.86540	18	100	1.0
N.TOWH	141.32540	38.78600	-66	100	1.0
N.KAKH	141.34210	38.51580	-202	100	1.0
N.KWSH	140.64050	38.18020	43	100	1.0
N.IWNH	140.84410	38.11330	-91	100	1.0
N.SISH	140.60270	38.00910	29	100	1.0
N.YMMH	140.89240	37.94110	-188	100	1.0
N.KMAH	140.59740	37.66360	104	100	1.0
N.MRUH	140.53800	37.48940	309	100	1.0
N.MKJH	140.72270	37.47030	408	100	1.0
N.HTAH	140.57030	37.21690	364	100	1.0
N.IWEH	140.97020	37.02640	-145	100	1.0

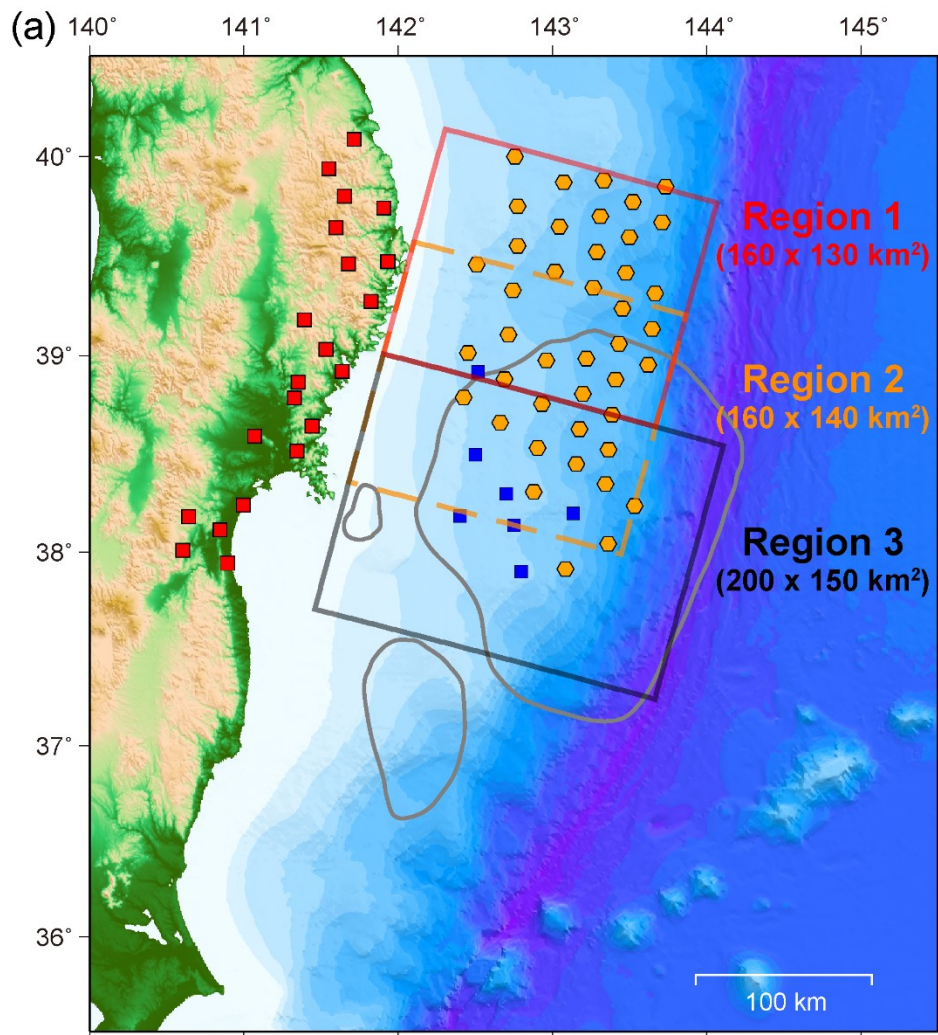


Figure 2.1. Station distribution before the 2011 Tohoku earthquake, from October 2007 to June 2008, in (a) total, (b) Region 1, (c) Region 2, and (d) Region 3. Each color rectangle shows the region for the array analysis. Colored symbols indicate the stations used in the corresponding periods and regions. Red, orange, and blue symbols denote the stations of NIED Hi-net, the Japan and Kuril Trenches observation project, and the recurrent seafloor observations off Miyagi, respectively. Gray contours outline the source region producing 10-m coseismic slip [Iinuma *et al.*, 2012].

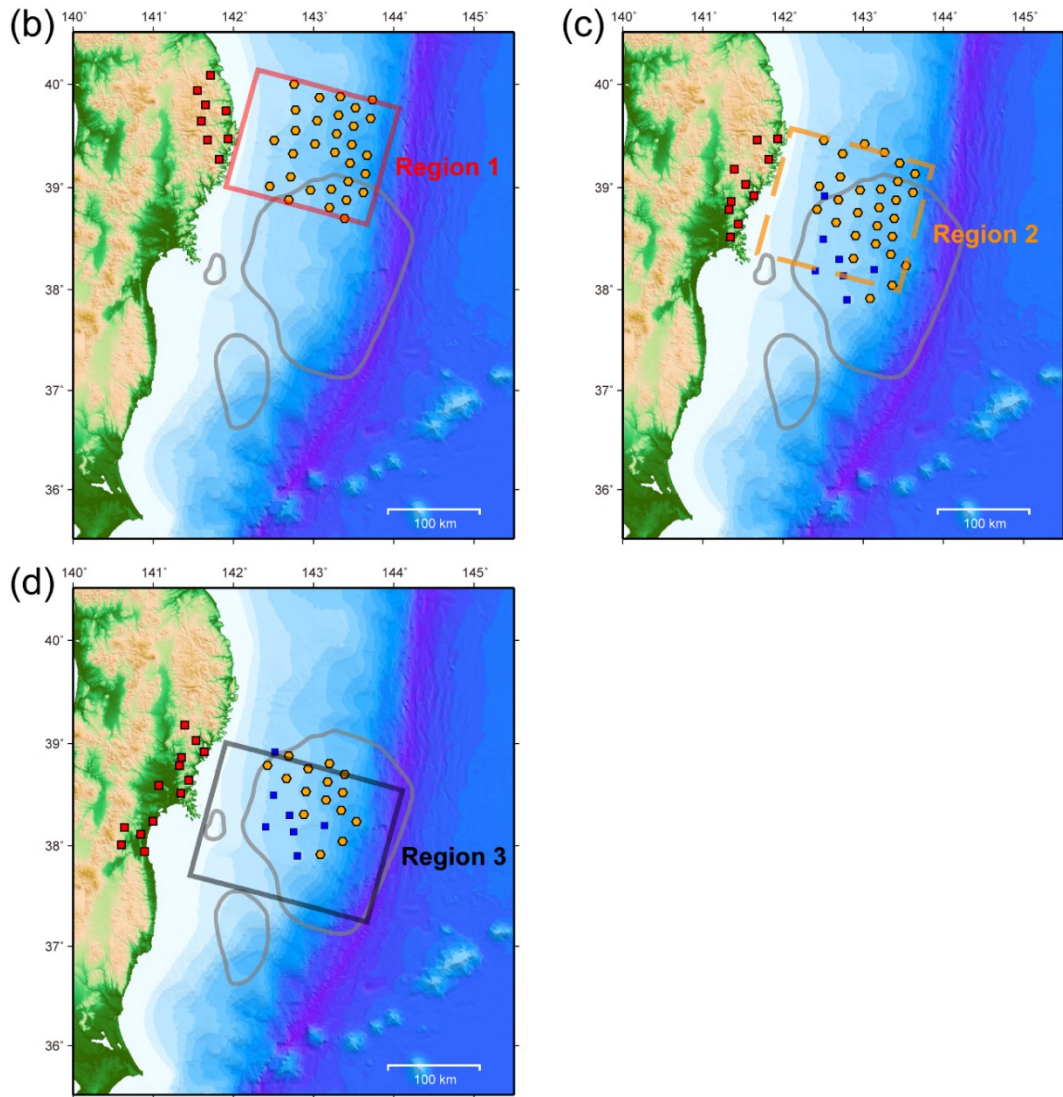


Figure 2.1. (continued).

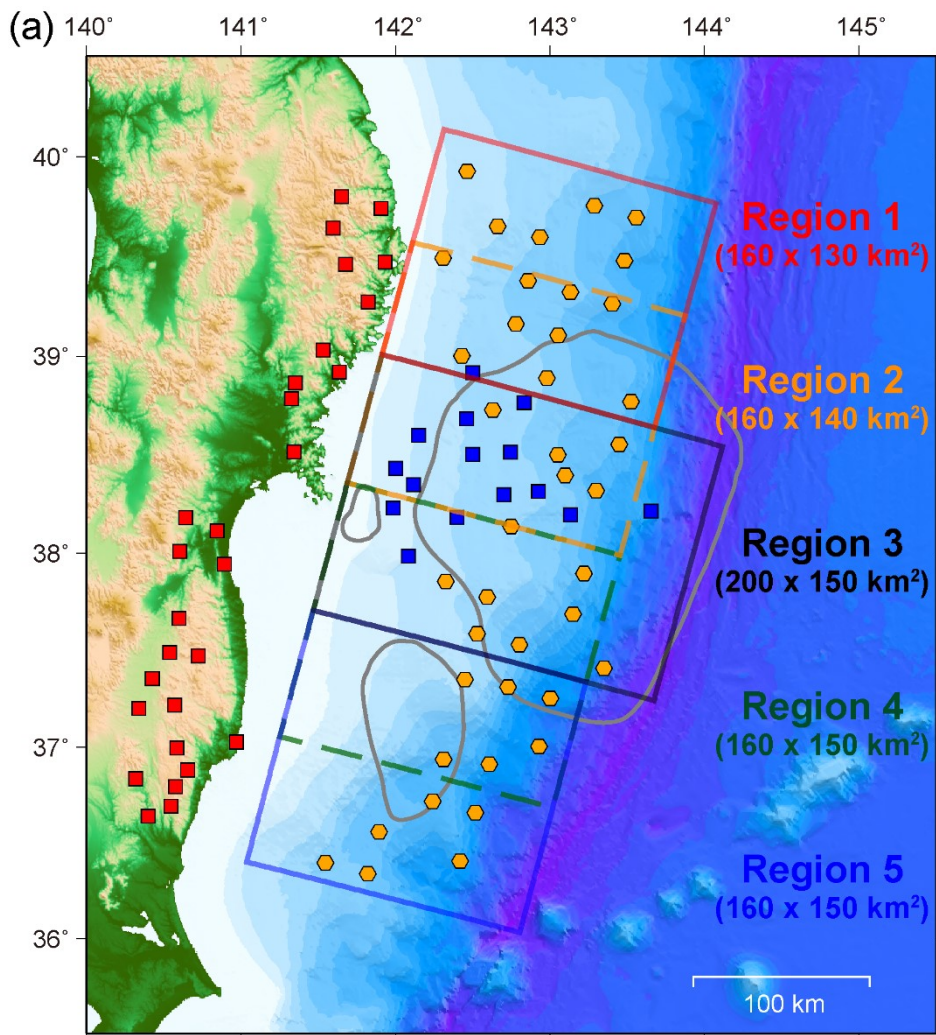


Figure 2.2. Station distribution for the first period of aftershock observation of the 2011 Tohoku earthquake in (a) total, (b) Region1, (c) Region 2, (d) Region 3, (e) Region 4, and (f) Region 5. Orange hexagons show the stations of the extensive seafloor aftershock observations [Shinohara *et al.*, 2011, 2012]. Other notations are the same as in Figure 2.1.

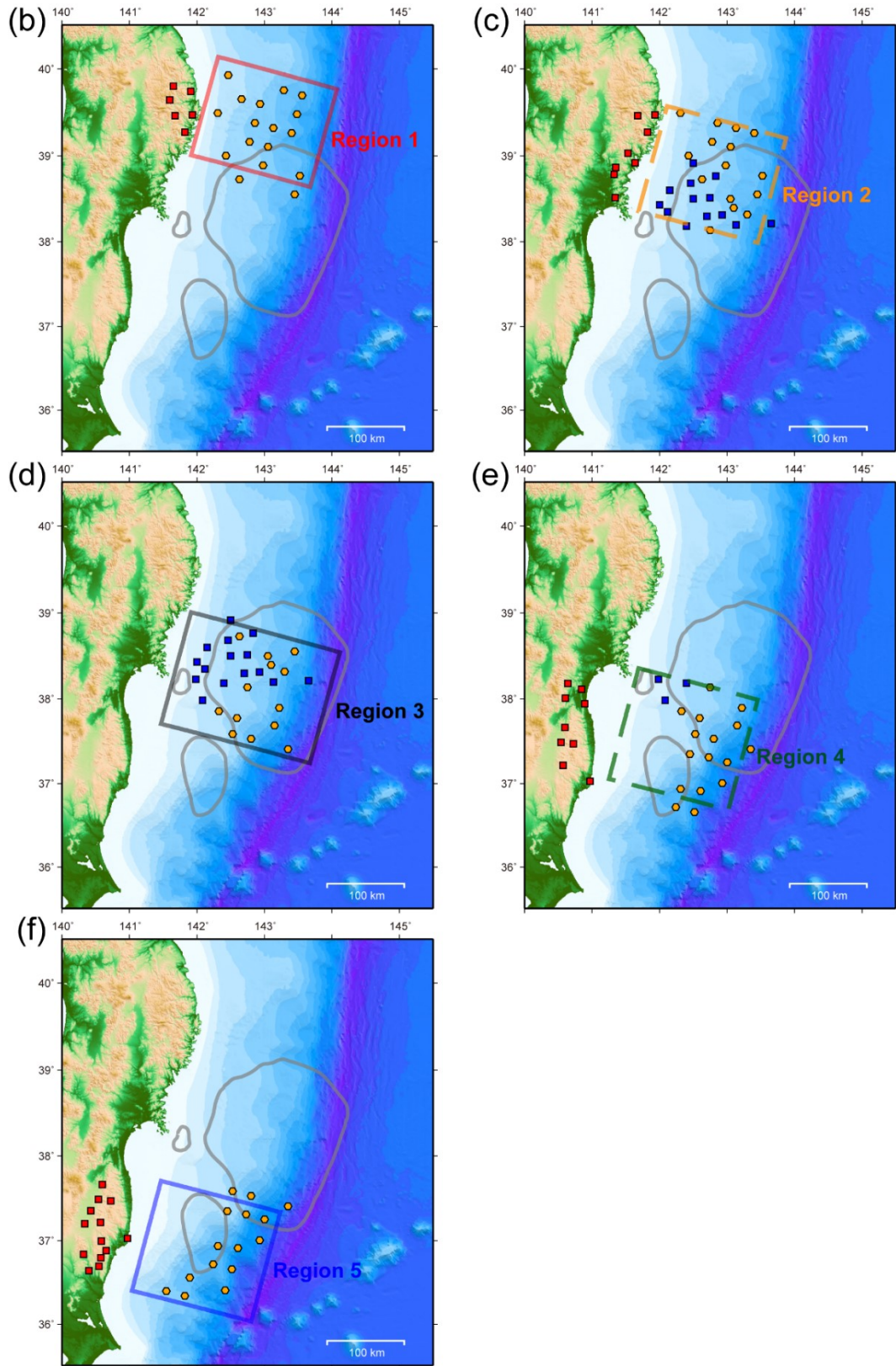


Figure 2.2. (continued).

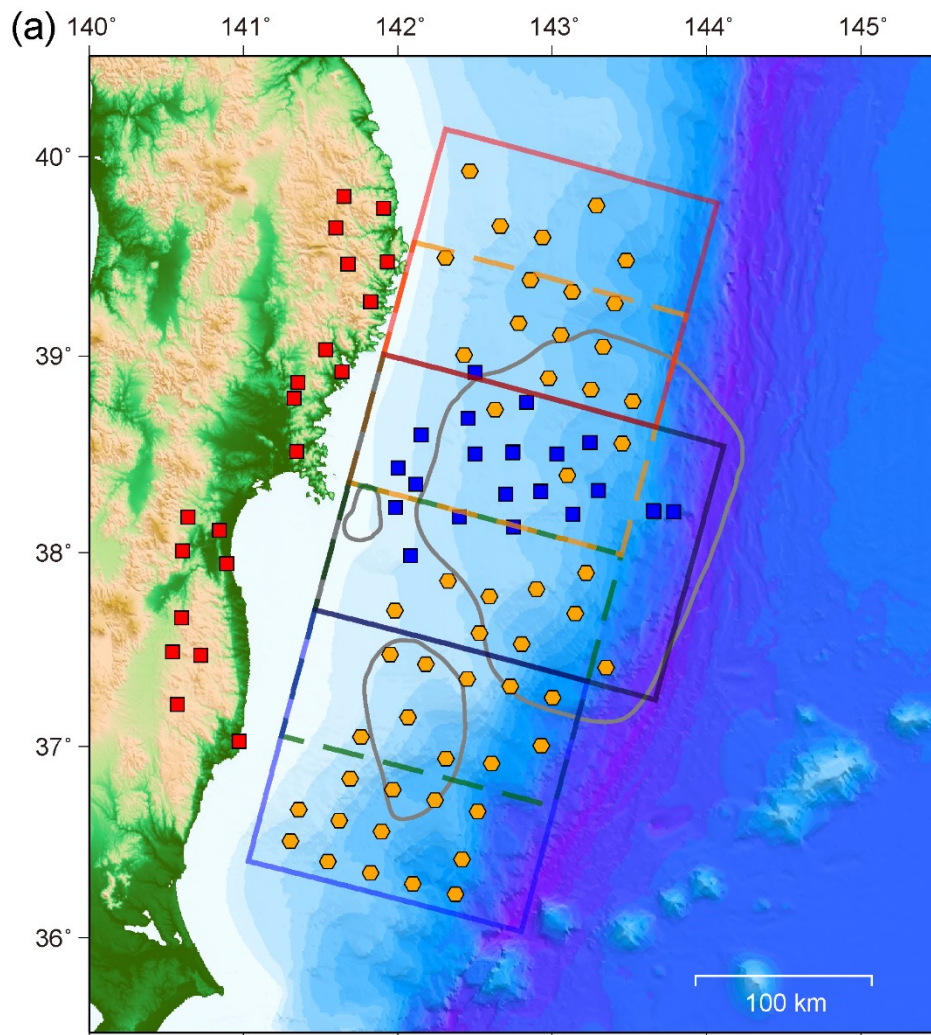


Figure 2.3. Station distribution for the second period of aftershock observation of the 2011 Tohoku earthquake in (a) total, (b) Region1, (c) Region 2, (d) Region 3, (e) Region 4, and (f) Region 5. All notations are the same as in Figure 2.2.

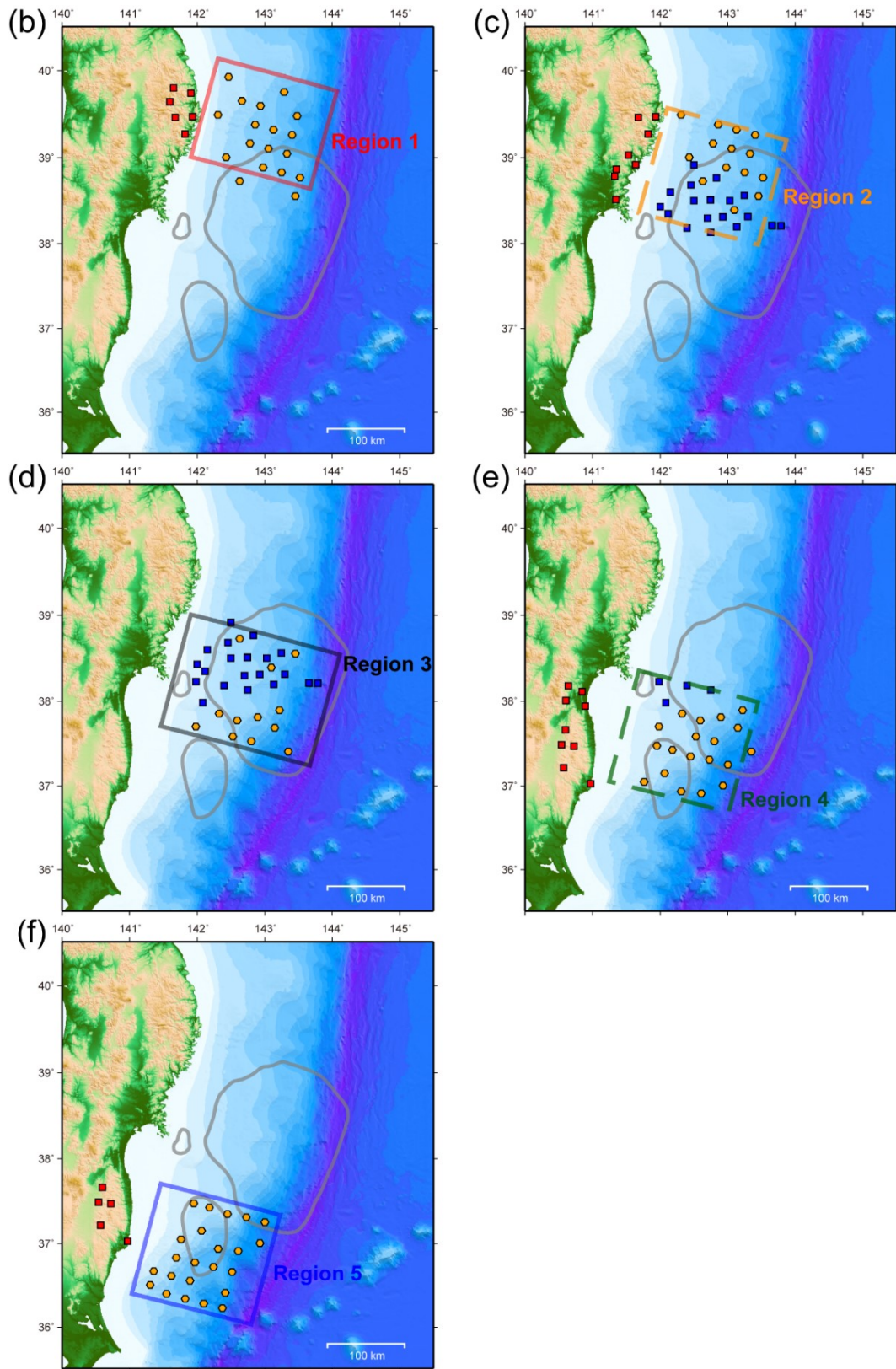


Figure 2.3. (continued).

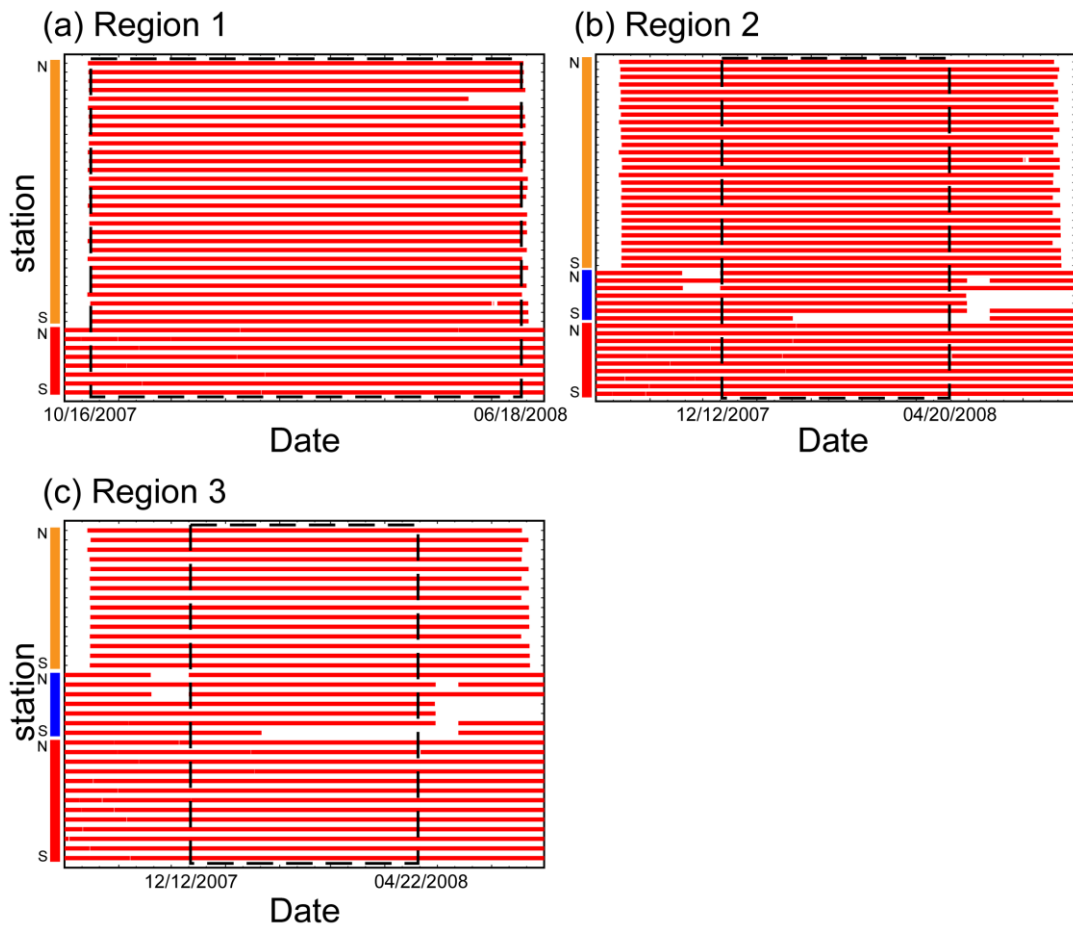


Figure 2.4. Observation periods of the stations before the 2011 Tohoku earthquake in (a) Region 1, (b) Region 2, and (c) Region 3 labeled from north to south. Red, orange, and blue vertical bars along the vertical axis correspond to the stations of NIED Hi-net, the Japan and Kuril Trenches observation project, and the recurrent seafloor observations off Miyagi, respectively. Each black dashed window indicates the periods of analysis.

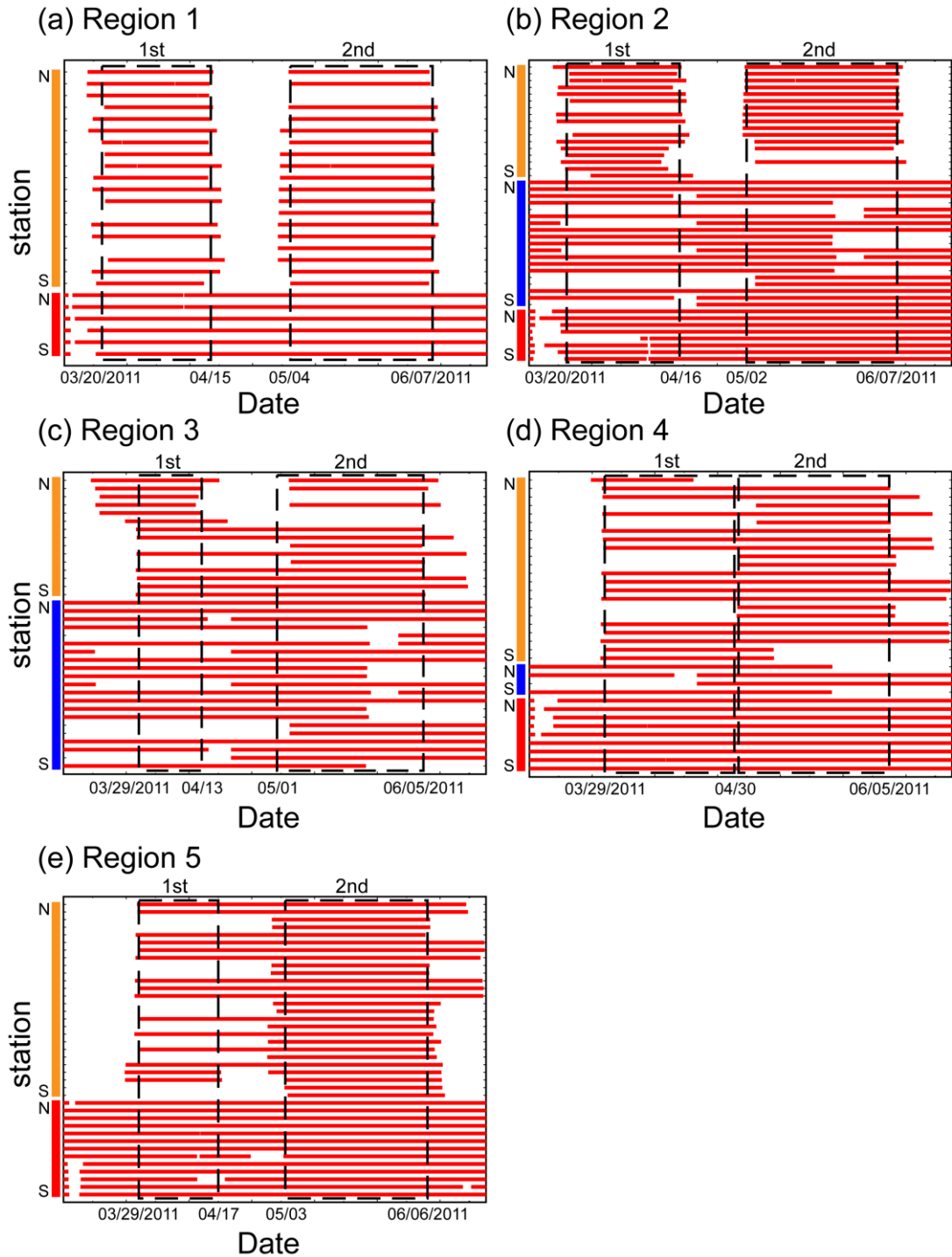


Figure 2.5. Observation periods of the stations after the 2011 Tohoku earthquake in (a) Region 1, (b) Region 2, (c) Region 3, (d) Region 4, and (e) Region 5 labeled from north to south. Orange vertical bars along the vertical axis correspond to the stations of the extensive seafloor aftershock observations [Shinohara *et al.*, 2011, 2012]. Other notations are the same as in Figure 2.4.

3. Detection and Location Method

In this chapter, I explain the method for detection and location of earthquakes and evaluation of validity of its application to earthquakes around the plate interface. A part of contents in this chapter is based on Nakatani *et al.* [2015].

3.1 Introduction

The most common way to detect and locate earthquakes was first introduced by Geiger [1910, 1912] with the following basic procedures. First, arrival times of seismic phases (basically P and/or S waves) of multiple earthquakes are manually/automatically picked at each single station. Then, the phase picks are mutually associated at multiple stations about possible common earthquakes. Finally, source locations of the earthquakes are determined so that the residuals between theoretical and observed traveltimes are minimized. Such traditional methods have been commonly employed for marine seismic observations using OBSs [e.g., Shinohara *et al.*, 2005; Hino *et al.*, 2006; Yamada *et al.*, 2011]. However, when seismicity is extremely high, such as during aftershock sequences of large earthquakes, the conventional event location method incorporating phase picking of small earthquakes and event association among stations is too laborious for elucidating the whole context of seismicity. In fact, as I will describe in Section 4.1, the number of primary event detections including both seismic events and noise through continuous waveform data at each region and sub-period after the Tohoku earthquake counts more than tens of thousands. Due to such unrealistic workloads on detection and location processes, the source parameters of aftershocks determined by Shinohara *et al.* [2011, 2012] are limited so that only events listed in the

JMA catalog (~1000 events) were relocated.

In the last few decades, several methods for automated detection and location have been proposed, and are confirmed to be valid in dealing with the above problems. One of the automated method is based on migration techniques using observed waveforms directly or characteristic functions calculated from the original waveforms. By stacking the waveforms or characteristic functions of an event at multiple stations of an array by changing delay times, one can search for its source as the point of maximum energy summation. Consequently, any phase picking and visual event identification are not required through the stacking techniques as described in the following examples. Liao *et al.* [2012] improved Source Scanning Algorithm (SSA) developed by Kao and Shan [2004] and applied it to the aftershock sequences of the 2006 Pingtung earthquake, Taiwan. SSA calculates a brightness function, which comes from stacking absolute normalized amplitudes at multiple stations of an array, and extracts the hypocenter as the point of the maximum brightness from its spatiotemporal distribution. An envelope correlation method, which was first proposed by Obara [2002] to determine the location of nonvolcanic deep tremors in the southwestern Japan, is also an effective way to detect and locate ordinary earthquakes. This method is based on measuring traveltimes difference between two stations by cross-correlating envelope waveforms. By using the envelope correlation method, Ide [2010] successfully detected and located 95% of ordinary earthquakes ($M > 1$) listed in the JMA catalog in the Nankai subduction zone, Japan. Instead of the original observed waveforms, Grigoli *et al.* [2013] calculated time series of the ratio between the Short-Term Average and Long-Term Average (STA/LTA) using both P and S waves as a characteristic function. Introducing such characteristic functions leads to the enhancement of the observed signals for detection and location processes. In addition, higher-order statistics, such as kurtosis and skewness, have

recently been introduced to phase arrival identification algorithms [e.g., Saragiotis *et al.*, 2002; Baillard *et al.*, 2014]. For example, Poiata *et al.* [2016] adopted kurtosis as a characteristic function of P waves. Their results show the validity of the method by application to real aftershock observation data in Central Chile. Because of large computational time, the above three examples, Liao *et al.* [2012], Grigoli *et al.* [2013], and Poiata *et al.* [2016], applied their methods only to short-term data for one week, a few hundreds of events, and one hour, respectively. In contrast, Nakatani *et al.* [2015] employed both STA/LTA algorithm and semblance analysis for event detection from continuous long-term (~ 1 year) OBS waveform data including aftershock sequences. They successfully determined several thousands of aftershocks using envelope waveforms of P waves in feasible computational time.

3.2 Overview of Detection and Location Scheme

I provide here a brief description of the method for event detection and location with reference to Nakatani *et al.* [2015]. In this study, three main processes of the stacking method are carried out through the following: (1) Event detection process by STA/LTA algorithm (Section 3.3), (2) semblance calculation process (Section 3.4), and (3) source extraction process (Section 3.4). Figure 3.1 shows a schematic illustration of the method to detect and locate earthquakes from the continuous waveform data.

In the first process, I detect non-stationary signals from the continuous waveform data by applying the STA/LTA triggering algorithm, and then assign a value of 1 for through event duration (on time) or 0 otherwise (off time) at each station. By multiplying the original waveforms by the on-and-off time sequences, waveforms of seismic events are extracted.

In the second process, I calculate semblance values in space and time by stacking waveforms of seismic events at multiple stations of the array. Here the first process contributes to reduction of computational time for event identification owing to skipping the semblance calculation during the event intervals.

In the third process, the source parameters of the origin time and the hypocenter are determined through searching for the time step and the location which gives the maximum semblance values. Details of each process are described in the later sections.

3.3 Event Detection Process by STA/LTA Algorithm

The STA/LTA triggering algorithm, which was first proposed by Allen [1978], is a useful method to detect non-stationary signals making use of temporal changes in the ratio of Short-Term Average to Long-Term Average of the absolute amplitudes at the station. This study adopted the STA/LTA algorithm to detect seismic events. I first determined parameters of the STA/LTA calculation so that the algorithm successfully detects coherent signals so as to minimize miss-detection of true earthquakes. In particular, I adjusted the values of the following parameters; the window lengths for calculations of STA and LTA, a threshold for STA/LTA trigger, and criteria for terminating the time window for the triggered event. In order to determine these parameters for each array, I tried several sets to a 1-hour vertical-component waveform data which includes the largest number of events listed in the JMA catalog. Here, waveforms in a frequency band of 2–15 Hz (resampled at 40 Hz) were used for the calculation, according to the observed dominant frequency of earthquakes (Figure 3.2). As a result, I selected the following set of values for all the arrays; the STA window length of 4 seconds, the LTA window length of 20 seconds, and the thresholds of STA/LTA ratio of 1.5 and 1.2 before and after the Tohoku earthquake, respectively. These parameters maximize detection of the JMA events, and avoid miss-interruption during the events (Figure 3.3). For comparison, the same or similar STA and LTA window lengths have been applied to OBS records (1-Hz velocity sensors) of other previous studies; the STA of 4 seconds and the LTA of 20 seconds for the Hikurangi subduction zone, New Zealand [Haijima, 2015], and the STA of 2 seconds and the LTA of 20 seconds for the southern part of the Japan Trench subduction zone [Nakatani *et al.*, 2015]. In terms of window placement, the STA window operates on more recent data

than the LTA window, and the STA window starts one data sample after the end of LTA window. This window placement gives better statistical independence between the STA and the LTA than the overlapping windows do [Withers *et al.*, 1998].

Figure 3.4 shows temporal change in STA/LTA ratio for the example time series. Rapid increases in the STA/LTA ratio corresponding to the *P*-wave arrival times can be confirmed at each event. The criteria for placing an end of the detected event is the time when the mean absolute amplitudes and the maximum amplitudes of a segment 2 seconds before the current time becomes lower than those of it before the detection time. If the duration time of an event exceeds 60 seconds, an end to the triggered event is forcedly placed so as to detect as many small earthquakes which may follow as possible. Results of the application of the STA/LTA triggering algorithm to a 1-hour waveform data recorded by both Hi-net and OBS stations are shown in Figure 3.5. With the selected parameters, the STA/LTA trigger (blue bars) certainly works for non-stationary signals as well as all *P*-wave arrival times of the events listed in the JMA catalog (red circles). On the basis of these conditions, I carried out the STA/LTA calculations with continuous vertical-component waveforms at each station and assigned a value of 1 through for event duration (on time) or 0 otherwise (off time).

By referring to the above results of STA/LTA calculations, I generated on-and-off time sequences of events for each station. Then, I extracted vertical-component envelope waveforms of events at each station by multiplying original envelope waveforms (bandpass filtered; 1–5 Hz; resampled at 16 Hz) by the on-and-off time sequences (Figure 3.1).

3.4 Semblance Calculation and Source Extraction Processes

In this process, I performed event identification via waveform stacking among the stations of the array using the envelope waveforms of events generated in the previous section as a kind of characteristic functions. In my techniques, I adopted a semblance value [Neidell and Taner, 1971] as a measure of waveform coherence. The semblance value at k th grid is defined as follows:

$$S_k = \frac{\sum_{i=-(M-1)/2}^{(M-1)/2} \left[\sum_{j=1}^N (A_j(t_i + dt_{kj}) - A_{j, \text{avg}}) \right]^2}{N \sum_{i=-(M-1)/2}^{(M-1)/2} \left[\sum_{j=1}^N (A_j(t_i + dt_{kj}) - A_{j, \text{avg}})^2 \right]}, \quad (1)$$

where N is the number of stations of an array, M is the number of time samples in a time window, $A_j(t)$ is the envelope amplitude recorded at the j th station at time t , and dt_{kj} is the travelt ime difference between the reference station of the array and the j th station for the k th source grid. $A_{j, \text{avg}}$ is the average envelope amplitude in each time window. Subtraction of the average from the original envelope amplitude enables to avoid all amplitudes to be positive leading to misidentification of energy release. Here semblance values will equal to 1 if envelope waveforms at all the stations of the array are identical and $1/N$ if envelope waveforms are perfectly random. Figure 3.6 shows an example of the semblance calculation for an event listed in the JMA catalog with the magnitude of 3.3. From the spatial distribution of semblance values projected onto the plate interface at the time which gives the maximum semblance values during the event, the location of semblance peak is in good agreement with that of Shinohara *et al.* [2012] (Figure 3.6b). Note that I introduced two conditions into this semblance calculation process due to computational costs. One is to impose depth grids of the source on the plate interface. That technically means that I used travelt ime difference tables, dt_{kj} , only along the plate

interface. The other condition is to execute semblance calculation only at the time step when the STA/LTA triggering is on (equals to non-zero envelope amplitudes) at more than 70% of the stations. Under these conditions, semblance calculations (without any processes) for 1-month continuous waveforms of about 30 stations take about 20 hours on average incorporating parallel computation using a Tesla C2070 Graphics Processing Unit.

For the traveltimes calculation, I used the Japan Integrated Velocity Structure Model (JIVSM) [Koketsu *et al.*, 2008, 2012] explicitly including the Pacific plate structure. Typical *P*-wave velocity of each layer of JIVSM is summarized in Table 3.1. *P*-wave traveltimes between the stations and the source grids along the plate interface were calculated by a fast marching method (FMTOMO package) [Rawlinson *et al.*, 2006] which is a grid based eikonal solver using wavefront tracking scheme in 3-D media [de Kool *et al.*, 2006]. Results of the traveltimes calculation at example stations are shown in Figure 3.7. Because incorrect depth of the Pacific plate of JIVSM can result in the wrong locations of hypocenters, I verified the accuracy of the plate interface depth by comparing with that of the model compiled by previous marine seismic observations using OBSs [Nakahigashi *et al.*, personal communication]. The depth differences between two models in the study region are up to 5 km which is not significant and is negligible for the sake of the following discussion (Figure 3.8), and therefore the depth of the Pacific plate of JIVSM is reasonable to use without modification.

Semblance values also depend on a frequency band of waveforms and a window length to calculate. I selected a preferable pair of them by calculating semblance values with several sets of bandpass filtered envelope waveforms and window lengths. For these trial experiments, I referred to three earthquake catalogs in Region 1 for the

second sub-period after the Tohoku earthquake; (1) repeating earthquakes (REs) determined by Uchida and Matsuzawa [2013], (2) the F-net (broadband seismograph network operated by NIED) events with variance reduction (VR) of larger than 0.8 determined by using at least 3 stations, and (3) earthquakes classified by their focal mechanisms by Nakamura *et al.* [2016] using waveform similarity with (1) and (2) as described in Chapter 1. The total number of reference events is 89, and their magnitudes are as low as 3. From the results of the average spatiotemporal maximum semblance values using each set of parameters, I determined a frequency band of waveforms to be 1–5 Hz and a length of time window to be 2 seconds (with a 1-second overlap) (Figure 3.9). This set of the frequency band of waveforms and the length of time window is reasonably selected so that they satisfy the following criteria: the time window should be sufficiently short to focus on *P*-wave onset phases for semblance calculations, and also should be long enough to cover some cycles of the wavelength.

Next, I examined a horizontal grid spacing of the source based on a Fresnel zone. According to Yilmaz [2001], the vertical resolution of seismic data is quantified by Rayleigh’s quarter-wavelength criteria defined as:

$$\lambda^{\text{vertical}} = \frac{\lambda}{4} = \frac{v}{4f_c}, \quad (2)$$

where λ , v , and f_c are a wavelength, a velocity, and a dominant frequency of the seismic event. Here I introduced the *P*-wave velocity in the uppermost layer (except water layer) of JIVSM (~ 2 km/s) and the *P*-wave dominant frequency which was assumed to be the frequency band (1–5 Hz) used in this study. Because the horizontal resolution is about twice worse than the vertical one [Yilmaz, 2001], the horizontal grid spacing, Grid^{H} , for the semblance calculation is required to satisfy the following condition:

$$\begin{aligned}
\text{Grid}^H &\geq \lambda^{\text{horizontal}} \sim 2\lambda^{\text{vertical}} \\
&= 2 \times \frac{2 \text{ km/s}}{4 \times 1-5 \text{ Hz}} = 0.2-1 \text{ km}.
\end{aligned} \tag{3}$$

I therefore adopted the horizontal grid spacing for the semblance calculation of 1 km.

With the above settings, the semblance values at each time step (here 1 second) at all grids (here 1 km \times 1 km along the plate interface) were calculated. Figure 3.10 shows an example time series of the maximum semblance values, S_{max} , within all the grids at each time step. The time series of S_{max} consists of zero and non-zero sequences according to the on-off states of the STA/LTA algorithm at the stations as described in the previous section. Here I assumed that there is only one event during a sequence of non-zero S_{max} . A time t_0 and a location (x, y, z) which have the maximum S_{max} during a sequence of non-zero S_{max} were extracted as values corresponding to a timing of the P -wave onset at the reference station of the array and the hypocenter, respectively. After the calculation of an origin time t using t_0 and the theoretical traveltime between the reference station and the hypocenter, I finally obtained the source parameters (x, y, z, t) for the event.

3.5 Synthetic Tests

As shown in Figures 2.1–2.3 of the station distributions, the station density varies among regions and observation periods. Such variable station density may result in low spatial resolution of hypocenters in some areas through hypocenter determination process. In addition, because I incorporated tables of traveltimes between stations and points along the plate interface in the semblance calculation, the accuracy of hypocenters could also be affected if true hypocenters are not exactly on the plate interface.

In order to evaluate the accuracy of epicenters, I conducted synthetic tests while source signature is represented by a Ricker wavelet (Figure 3.11a). The amplitude $A(t)$ of the Ricker wavelet at time t is defined as:

$$A(t) = \left(1 - 2\pi^2 f_p^2 t^2\right) e^{-\pi^2 f_p^2 t^2}, \quad (4)$$

where f_p is the peak frequency of the wavelet. Because I applied 1–5 Hz bandpass filter to waveforms of the real data for the semblance calculation process, I prepared a synthetic envelope waveform of equation (4) with $f_p = 3$ Hz at each station (Figure 3.11b). Then, I shifted the waveforms in the time domain by delay times calculated at each station for varying focal depth z_s relative to the plate interface by -10 (in the hanging wall), 0 (on the plate interface), and 10 km (in the slab). Finally, I stacked the synthetic envelope waveforms among the stations and backprojected their semblance values using traveltimes assuming that the hypocenters were on the plate interface.

When the initial hypocenters are on the plate interface ($z_s = 0$ km), the resultant epicenters well coincide with their true locations. When the initial hypocenters are off the plate interface ($z_s = -10, 10$ km), most of the results also show good agreement between the initial and resultant epicenters in the central area of each region. On the

other hand, some resultant epicenters deviate from their true locations near the boundaries of each region with a relatively low station coverage, especially in the down-dip side of the study region. Figure 3.12 shows distribution of those resultant epicenters derived by the synthetic tests. The error of these epicenters is estimated at most 20 km from these results. In the following chapters, I will discuss the seismicity by taking into account the above synthetic results.

In addition to the epicentral accuracy, it is significant to evaluate the detectability of earthquakes off the plate interface. Such evaluation will provide a depth resolution of earthquakes which are detected and located by the automated method of this study. I therefore investigated the maximum semblance values according to the focal depth. The procedure of this test is the same as that of the above test except that white Gaussian noise was added to the original synthetic Ricker wavelets. Figure 3.13 shows the setting of the synthetic test and the variations in the maximum semblance values corresponding to the initial epicenters and focal depths from the plate interface. When the initial hypocenters are off the plate interface ($|z_s| = 5, 10$ km), the average maximum semblance values over all the epicenters rapidly decrease by more than about 30–40% from those of the initial hypocenters on the plate interface ($z_s = 0$ km), regardless of the signal-to-noise ratio (Figures 3.13d, f, h, j, l, and n). These results indicate that the distance in the depth direction from the plate interface is a critical factor to sort out the detected events via the threshold setting of the semblance value. In contrast, if the initial hypocenters are the closest to the trench, the resulting maximum semblance values remain high with little change regardless of the initial focal depths (red lines in Figures 3.13e, g, i, k, m, and o) because the traveltimes among stations pairs do not vary with focal depths in the shallow part of the Japan Trench subduction zone.

From the results of these synthetic tests, I conclude that the method of this study

focuses on the detection and location of earthquakes around the plate interface except for the area near the trench. In other words, undetected events by this study can be characterized as ones which occurred off the plate interface (> 5 km).

3.6 Magnitude Determination and Correction

After the detection and location processes, I determined magnitudes of the identified events regarding a current calculation formula of the JMA velocity magnitude [Funasaki *et al.*, 2004] as follows:

$$M_i = \frac{1}{0.85} \log_{10} A_z + \beta_v(\Delta, H) + C_v, \quad (5)$$

where A_z is the maximum amplitude in the vertical-component velocity waveform in 10^{-5} m/s at the i th station, β_v is the distance attenuation term as a function of the epicentral distance Δ in km and the focal depth H in km, and C_v is the correction term about the station types. I searched for the maximum amplitudes in the non-filtered vertical seismograms from 5 seconds before the P -wave onsets to $20 + r/8$ seconds after the onsets, where r is the hypocentral distance. The value of β_v is empirically determined using B-spline functions so that the JMA velocity magnitudes are consistent with the JMA displacement magnitudes [Katsumata, 2007]. As for the correction term, JMA empirically assigns a value of 0.43 for the Hi-net stations and 0.11 for OBS stations to C_v , while the station-specific correction is also required to accurately determine magnitudes. In particular, because OBSs are deployed just above thick unconsolidated seafloor sediments, magnitudes determined from OBS records tend to be overestimated due to large amplifications. I therefore conducted the station-specific correction of the magnitudes at each station by comparing with those listed in the JMA catalog as discussed below.

For the sake of the magnitude correction, I referred to the JMA magnitudes of target events. For the pre-Tohoku period, I used all the events with magnitudes greater than 2 in the JMA catalog. For the post-Tohoku period, I used events listed in the catalog of Shinohara *et al.* [2011, 2012] in which hypocenters of selected earthquakes

from the JMA catalog were relocated using the same OBS data with this study so that I can measure amplitudes of common events at the stations. Then, I assumed a linear relationship between magnitudes M_i at the i th station derived from equation (5) and those of the JMA catalog (M_{JMA}) for common events as below:

$$M_i = aM_{\text{JMA}} + b, \quad (6)$$

and determined the regression coefficient a and the constant value b at each station by the least squares method (Figure 3.14a–d). The standard deviations of a and b were also determined. The events whose magnitudes deviated by more than 0.5 magnitude units from the regression line were removed for the calculation of the coefficients, a and b , and then the regression analysis was repeated again. Examples of the coefficients, a and b , in Region 1 for the pre-Tohoku period are shown in Figure 3.14e. Even for the Hi-net stations, small differences in magnitudes between M_i and M_{JMA} are also confirmed due to the station-specific biases (Figure 3.14d). On average of the Hi-net stations, M_i is almost an equivalent to M_{JMA} in all the periods before the magnitude correction (Figure 3.14f). On the other hand, overestimation of the magnitude is remarkable with OBS records (Figure 3.14g). Therefore, the resultant magnitudes using waveform data from both OBS and Hi-net stations before the correction are also overestimated (Figure 3.14h). The magnitude correction parameters for each station are listed in Table 3.2.

After the above determination of the correction parameters, four steps for the entire magnitude determination and correction were carried out. First, the initial magnitudes of all the identified events at each station were obtained by using equation (5), and corrected by using the (a, b) parameters of the station as follows:

$$M_{i, \text{corr}} = \frac{M_i - b}{a}, \quad (7)$$

where $M_{i, \text{corr}}$ is the corrected magnitude at the i th station. Figure 3.14i shows the result

of this initial correction of the magnitudes (correction for Figure 3.14h) in Region 1 for the second sub-period after the Tohoku earthquake. Second, the mean of the corrected magnitudes among all the stations for each event were calculated. Third, the stations whose corrected magnitudes, $M_{i, \text{corr}}$, deviated by more than 0.5 from the mean magnitude were eliminated from the magnitude correction. Finally, the conclusive mean and standard deviation of the corrected magnitudes among the selected stations were recalculated. If the conclusive standard deviation σ_M was less than 0.35 and the number of stations N_{sta} used to calculate was not less than 3, the conclusive mean magnitude M_{mean} was assigned to the event. These criteria will be applied at Step 3 in Section 4.1.

Table 3.1. Typical *P*-wave velocity of each layer in JIVSM.

	Typical <i>P</i>-wave velocity
Sea water	1.5 km/s
Sediment layer	~2 km/s
Sedimentary rock	~4 km/s
Upper crust	5.5–5.8 km/s
Lower crust	6.4 km/s
Continental mantle	7.5 km/s
Oceanic layer 2	5.4 km/s
Oceanic layer 3	6.5 km/s
Oceanic mantle	8.1 km/s

Table 3.2. Parameters of the magnitude correction for (a) the pre-Tohoku period, (b) the first, and (c) the second sub-periods of aftershock observations of the 2011 Tohoku earthquake. All the stations of each observation are listed from north to south.

(a) Station	Region 1		Region 2		Region 3	
	<i>a</i>	<i>b</i>	<i>a</i>	<i>b</i>	<i>a</i>	<i>b</i>
ML46	0.876	0.641	–	–	–	–
ML30	1.008	0.407	–	–	–	–
ML38	0.880	0.659	–	–	–	–
ML07	1.015	0.691	–	–	–	–
ML19	1.013	0.642	–	–	–	–
ML45	0.913	0.748	–	–	–	–
ML29	1.050	0.464	–	–	–	–
ML06	1.006	0.691	–	–	–	–
ML37	0.916	0.612	–	–	–	–
ML18	1.015	0.751	–	–	–	–
ML44	1.027	0.694	–	–	–	–
ML28	0.982	0.598	–	–	–	–
ML49	0.834	0.864	0.517	2.037	–	–
ML36	0.985	0.635	0.833	1.070	–	–
ML17	1.006	0.992	–	–	–	–
ML27	1.068	0.440	0.924	0.900	–	–
ML43	0.897	0.791	0.778	1.240	–	–
ML04	1.032	0.703	–	–	–	–
ML16	1.040	0.769	1.043	0.675	–	–
ML03	0.955	1.458	1.069	1.031	–	–
ML42	0.940	0.822	0.871	0.904	–	–
ML15	1.030	0.689	1.017	0.587	–	–
ML48	0.842	1.064	0.827	0.914	–	–
ML26	0.985	0.671	0.989	0.640	–	–
ML35	0.986	0.539	0.961	0.545	–	–
ML02	0.949	0.903	0.894	1.042	–	–
ML41	0.894	0.809	0.892	0.572	0.710	1.240
ML14	0.954	0.763	0.972	0.686	–	–

ML25	0.969	0.720	1.023	0.528	0.831	1.105
ML47	–	–	0.990	-1.446	0.885	-1.051
ML34	–	–	0.898	0.534	0.781	1.001
ML13	0.890	0.940	0.963	0.720	0.778	1.310
ML40	–	–	0.932	0.401	0.831	0.827
ML24	–	–	0.993	0.593	0.874	0.979
ML33	–	–	1.032	0.263	0.877	0.692
ML12	–	–	1.000	0.532	0.883	0.863
ML23	–	–	1.067	0.496	0.958	0.799
ML11	–	–	0.951	0.884	0.855	1.135
ML32	–	–	0.981	0.484	0.970	0.519
ML01	–	–	0.772	1.396	0.790	1.407
ML10	–	–	0.873	1.028	0.868	1.052
ML22	–	–	0.896	0.909	0.949	0.801
LS02b	–	–	0.844	-1.123	0.775	-0.733
S04a	–	–	0.802	-1.106	0.809	-1.058
LS04b	–	–	0.995	-1.456	0.897	-1.161
S09	–	–	0.880	-0.789	0.934	-0.922
S03	–	–	0.764	-0.796	0.875	-1.125
S08a	–	–	1.008	-1.456	0.954	-1.428
S07a	–	–	–	–	1.040	-1.320
N.KJSH	1.016	-0.132	–	–	–	–
N.KZMH	0.999	0.039	–	–	–	–
N.IWZH	1.028	-0.139	–	–	–	–
N.TROH	0.937	-0.088	–	–	–	–
N.KANH	1.035	-0.017	–	–	–	–
N.YMDH	1.004	-0.186	1.028	-0.134	–	–
N.KASH	1.079	-0.239	1.043	-0.055	–	–
N.KMIH	0.974	0.153	1.013	0.103	–	–
N.SMTH	–	–	1.058	-0.014	1.030	0.108
N.RZTH	–	–	1.072	-0.116	1.010	0.027
N.KKWH	–	–	0.994	0.122	1.022	0.087
N.FSWH	–	–	1.018	-0.012	1.018	0.023
N.TOWH	–	–	1.033	0.024	1.034	0.008
N.SZGH	–	–	0.985	0.062	0.973	0.155
N.TAJH	–	–	–	–	0.985	0.260

N.KAKH	–	–	0.996	0.064	1.006	0.126
N.SNDH	–	–	–	–	0.985	0.110
N.KWSH	–	–	–	–	0.896	0.965
N.IWNH	–	–	–	–	0.875	0.725
N.SISH	–	–	–	–	0.756	1.184
N.YMMH	–	–	–	–	0.732	1.305

(b) Station	Region 1		Region 2		Region 3		Region 4		Region 5	
	<i>a</i>	<i>b</i>								
A01a	1.119	-0.482	–	–	–	–	–	–	–	–
A04a	1.039	-0.173	–	–	–	–	–	–	–	–
A05	0.987	0.442	–	–	–	–	–	–	–	–
B02a	1.122	-0.504	–	–	–	–	–	–	–	–
B03a	1.083	-0.362	–	–	–	–	–	–	–	–
C01a	1.078	-0.182	1.052	0.009	–	–	–	–	–	–
B05a	1.076	0.133	–	–	–	–	–	–	–	–
C03a	0.996	0.265	1.083	-0.046	–	–	–	–	–	–
C04a	1.115	-0.361	1.205	-0.717	–	–	–	–	–	–
C05a	1.106	-0.246	1.151	-0.441	–	–	–	–	–	–
D03a	1.099	-0.423	1.120	-0.488	–	–	–	–	–	–
D04a	1.033	0.161	1.118	-0.170	–	–	–	–	–	–
E02a	0.859	0.347	0.971	-0.152	–	–	–	–	–	–
E04a	0.975	-0.136	1.084	-0.527	–	–	–	–	–	–
E06a	0.833	0.453	1.041	-0.327	–	–	–	–	–	–
F03a	1.001	-0.053	1.087	-0.302	1.074	-0.361	–	–	–	–
F06a	0.943	0.325	1.157	-0.492	1.215	-0.683	–	–	–	–
NS10	–	–	1.218	-0.728	1.095	-0.188	–	–	–	–
G05a	–	–	1.145	-0.524	1.195	-0.692	–	–	–	–
NS18	–	–	1.073	-0.124	0.942	0.585	–	–	–	–
NS08	–	–	1.019	0.029	1.212	-0.826	0.922	0.134	–	–
I06	–	–	–	–	1.070	-0.342	0.939	0.023	–	–
J03	–	–	–	–	1.181	-0.840	0.879	-0.026	–	–
J04	–	–	–	–	1.031	-0.080	0.950	-0.066	–	–
J06	–	–	–	–	0.953	0.119	0.916	0.112	–	–
K04	–	–	–	–	1.208	-1.098	1.013	-0.442	0.873	0.214

K05	–	–	–	–	0.680	1.858	0.761	1.176	0.678	1.532
K07	–	–	–	–	1.048	-0.650	0.891	-0.125	0.788	0.346
L04	–	–	–	–	–	–	0.866	0.292	0.697	0.980
L05	–	–	–	–	–	–	0.561	2.162	0.613	1.919
L06	–	–	–	–	–	–	0.903	0.629	0.951	0.469
M06	–	–	–	–	–	–	0.826	0.763	0.900	0.446
N04	–	–	–	–	–	–	0.574	2.257	0.442	2.789
N05	–	–	–	–	–	–	0.713	1.590	0.690	1.703
O04a	–	–	–	–	–	–	1.007	-0.521	0.878	0.006
O05a	–	–	–	–	–	–	0.885	0.537	0.757	1.138
P03a	–	–	–	–	–	–	–	–	0.788	0.530
P05a	–	–	–	–	–	–	–	–	0.727	1.373
Q02a	–	–	–	–	–	–	–	–	0.834	0.430
Q03a	–	–	–	–	–	–	–	–	0.739	0.679
LS02	–	–	0.758	0.388	1.090	-0.986	–	–	–	–
LS03	–	–	0.981	-0.500	1.101	-1.031	–	–	–	–
LS01a	–	–	0.906	-0.529	1.162	-1.437	–	–	–	–
S27	–	–	0.893	-0.213	0.909	-0.190	–	–	–	–
S14a	–	–	1.094	-1.133	1.254	-1.668	–	–	–	–
S04	–	–	0.865	0.023	1.056	-0.851	–	–	–	–
S21	–	–	1.008	-0.893	1.240	-1.696	–	–	–	–
S01	–	–	1.000	-0.862	1.253	-1.771	–	–	–	–
S15a	–	–	1.085	-1.034	1.175	-1.259	–	–	–	–
LS04	–	–	0.997	-0.759	1.293	-2.002	–	–	–	–
S22	–	–	–	–	1.034	-1.065	0.931	-0.617	–	–
TO1	–	–	0.987	-0.899	1.317	-2.256	–	–	–	–
S09	–	–	1.180	-1.204	1.142	-0.901	–	–	–	–
S03a	–	–	0.965	-0.553	1.118	-1.205	1.000	-0.767	–	–
S03b	–	–	–	–	–	–	0.592	0.250	–	–
S02	–	–	–	–	1.086	-0.822	0.889	-0.207	–	–
N.IWZH	1.245	-0.969	–	–	–	–	–	–	–	–
N.TROH	1.228	-1.083	–	–	–	–	–	–	–	–
N.KANH	1.233	-0.778	–	–	–	–	–	–	–	–
N.YMDH	1.172	-0.732	1.236	-1.005	–	–	–	–	–	–
N.KASH	1.167	-0.617	1.219	-0.785	–	–	–	–	–	–
N.KMIH	1.019	0.084	1.142	-0.369	–	–	–	–	–	–

N.RZTH	–	–	1.205	-0.590	–	–	–	–	–	–
N.KKWH	–	–	1.227	-0.681	–	–	–	–	–	–
N.FSWH	–	–	1.171	-0.418	–	–	–	–	–	–
N.TOWH	–	–	1.268	-0.862	–	–	–	–	–	–
N.KAKH	–	–	1.153	-0.531	–	–	–	–	–	–
N.KWSH	–	–	–	–	–	–	1.030	0.632	–	–
N.IWNH	–	–	–	–	–	–	1.101	-0.088	–	–
N.SISH	–	–	–	–	–	–	1.074	0.204	–	–
N.YMMH	–	–	–	–	–	–	0.956	0.511	–	–
N.KMAH	–	–	–	–	–	–	1.138	-0.431	0.959	0.363
N.MRUH	–	–	–	–	–	–	1.195	-0.495	1.059	0.124
N.MKJH	–	–	–	–	–	–	1.181	-0.682	0.986	0.131
N.KRYH	–	–	–	–	–	–	–	–	1.057	0.072
N.HTAH	–	–	–	–	–	–	1.162	-0.496	1.124	-0.332
N.YBKH	–	–	–	–	–	–	–	–	0.954	0.554
N.IWEH	–	–	–	–	–	–	1.023	-0.204	0.949	0.136
N.IWWH	–	–	–	–	–	–	–	–	0.935	0.126
N.KIBH	–	–	–	–	–	–	–	–	0.918	0.116
N.DGOH	–	–	–	–	–	–	–	–	0.948	0.194
N.THGH	–	–	–	–	–	–	–	–	0.913	0.271
N.JUOH	–	–	–	–	–	–	–	–	0.939	0.107
N.YMAH	–	–	–	–	–	–	–	–	1.000	-0.099

(c) Station	Region 1		Region 2		Region 3		Region 4		Region 5	
	<i>a</i>	<i>b</i>								
A01b	0.973	1.116	–	–	–	–	–	–	–	–
A04b	0.956	1.375	–	–	–	–	–	–	–	–
B02b	0.955	1.283	–	–	–	–	–	–	–	–
B03b	1.065	0.846	–	–	–	–	–	–	–	–
C01b	0.944	1.530	0.968	1.450	–	–	–	–	–	–
B05b	0.876	1.726	–	–	–	–	–	–	–	–
C03b	0.898	1.703	0.944	1.493	–	–	–	–	–	–
C04b	0.967	1.215	0.955	1.228	–	–	–	–	–	–
C05b	0.883	1.700	0.873	1.677	–	–	–	–	–	–
D03b	0.962	1.386	0.937	1.420	–	–	–	–	–	–

D04b	0.935	1.251	0.938	1.279	–	–	–	–	–	–
D05	0.850	1.555	0.820	1.663	–	–	–	–	–	–
E02b	0.929	1.284	0.934	1.188	–	–	–	–	–	–
E04b	0.917	1.150	0.843	1.410	–	–	–	–	–	–
E05	0.847	1.737	0.824	1.811	–	–	–	–	–	–
E06b	0.820	1.612	0.838	1.592	–	–	–	–	–	–
F03b	0.946	1.027	0.927	1.199	0.929	1.328	–	–	–	–
F06b	0.853	1.614	0.848	1.688	0.851	1.721	–	–	–	–
G05b	–	–	0.836	1.391	0.940	1.130	–	–	–	–
I06	–	–	–	–	1.119	-0.446	1.035	-0.175	–	–
J03	–	–	–	–	1.028	-0.452	0.944	-0.200	–	–
JI05	–	–	–	–	1.008	0.962	0.942	1.273	–	–
J04	–	–	–	–	1.101	-0.336	0.904	0.172	–	–
K02	–	–	–	–	1.012	1.109	0.881	1.757	–	–
J06	–	–	–	–	1.045	-0.311	0.948	0.044	–	–
K04	–	–	–	–	0.904	0.027	1.156	-0.856	–	–
K05	–	–	–	–	1.159	-0.187	0.921	0.608	–	–
L02	–	–	–	–	–	–	0.870	0.070	0.926	-0.037
L03	–	–	–	–	–	–	0.755	0.474	0.844	0.292
K07	–	–	–	–	0.959	-0.317	1.008	-0.504	–	–
L04	–	–	–	–	–	–	0.875	0.320	0.958	0.079
L05	–	–	–	–	–	–	0.896	0.941	0.831	1.210
L06	–	–	–	–	–	–	0.921	0.536	0.960	0.507
M03	–	–	–	–	–	–	0.692	0.916	0.795	0.730
N02	–	–	–	–	–	–	0.853	0.599	0.756	1.017
M06	–	–	–	–	–	–	0.864	0.511	0.847	0.610
N04	–	–	–	–	–	–	0.681	1.889	0.595	2.235
N05	–	–	–	–	–	–	0.901	0.814	0.889	0.977
O02	–	–	–	–	–	–	–	–	1.071	0.683
O03	–	–	–	–	–	–	–	–	0.992	1.183
O04b	–	–	–	–	–	–	–	–	1.041	0.845
P01	–	–	–	–	–	–	–	–	0.959	0.905
O05b	–	–	–	–	–	–	–	–	0.726	3.037
P02	–	–	–	–	–	–	–	–	1.077	0.728
P03b	–	–	–	–	–	–	–	–	1.072	0.839
Q01	–	–	–	–	–	–	–	–	0.942	1.178

P05b	-	-	-	-	-	-	-	-	0.967	1.422
Q02b	-	-	-	-	-	-	-	-	0.994	0.848
Q03b	-	-	-	-	-	-	-	-	0.991	0.753
Q04	-	-	-	-	-	-	-	-	1.101	1.111
Q05	-	-	-	-	-	-	-	-	1.029	0.981
LS02	-	-	0.847	-0.136	0.849	-0.019	-	-	-	-
LS03	-	-	0.886	-0.120	0.800	0.084	-	-	-	-
LS01b	-	-	0.921	-1.211	0.911	-1.052	-	-	-	-
S27	-	-	0.805	0.004	0.740	0.303	-	-	-	-
S17	-	-	0.816	-1.006	0.681	-0.544	-	-	-	-
S14a	-	-	1.082	-1.556	1.289	-2.021	-	-	-	-
S14b	-	-	1.082	-1.555	1.291	-2.028	-	-	-	-
S10b	-	-	0.889	-1.244	0.832	-1.025	-	-	-	-
S04	-	-	0.907	-0.237	0.837	-0.062	-	-	-	-
S21	-	-	1.006	-0.810	1.093	-1.037	-	-	-	-
S01	-	-	0.867	-0.350	0.946	-0.501	-	-	-	-
S18b	-	-	0.856	-1.419	1.047	-1.860	-	-	-	-
S15a	-	-	1.201	-2.035	1.279	-2.127	-	-	-	-
S15b	-	-	1.201	-2.035	1.282	-2.143	-	-	-	-
LS04	-	-	0.890	-0.507	1.005	-0.840	-	-	-	-
S22	-	-	-	-	1.097	-1.073	0.884	-0.405	-	-
TO1	-	-	0.697	0.036	0.156	1.985	-	-	-	-
BT2	-	-	0.935	-0.487	1.106	-0.919	-	-	-	-
BT1	-	-	0.883	-0.704	0.948	-0.856	-	-	-	-
S09	-	-	0.875	-0.149	0.937	-0.180	-	-	-	-
S03b	-	-	0.990	-1.433	1.051	-1.645	0.935	-1.042	-	-
S08	-	-	0.922	-1.233	1.101	-1.701	0.917	-1.129	-	-
S02	-	-	-	-	0.920	-0.117	0.832	0.058	-	-
N.IWZH	1.058	-0.211	-	-	-	-	-	-	-	-
N.TROH	1.113	-0.550	-	-	-	-	-	-	-	-
N.KANH	1.059	-0.051	-	-	-	-	-	-	-	-
N.YMDH	1.130	-0.583	1.065	-0.448	-	-	-	-	-	-
N.KASH	1.057	-0.180	1.042	-0.189	-	-	-	-	-	-
N.KMIH	1.048	-0.034	1.035	-0.014	-	-	-	-	-	-
N.RZTH	-	-	1.058	-0.029	-	-	-	-	-	-
N.KKWH	-	-	1.065	-0.128	-	-	-	-	-	-

N.FSWH	-	-	1.083	-0.095	-	-	-	-	-	-
N.TOWH	-	-	1.058	-0.143	-	-	-	-	-	-
N.KAKH	-	-	1.031	-0.161	-	-	-	-	-	-
N.KWSH	-	-	-	-	-	-	1.056	0.559	-	-
N.IWNH	-	-	-	-	-	-	0.999	0.335	-	-
N.SISH	-	-	-	-	-	-	1.075	0.295	-	-
N.YMMH	-	-	-	-	-	-	0.879	0.864	-	-
N.KMAH	-	-	-	-	-	-	1.074	-0.166	1.187	-0.431
N.MRUH	-	-	-	-	-	-	1.082	-0.075	1.123	-0.104
N.MKJH	-	-	-	-	-	-	1.066	-0.250	1.176	-0.512
N.HTAH	-	-	-	-	-	-	1.043	-0.026	1.103	-0.210
N.IWEH	-	-	-	-	-	-	0.631	1.331	0.736	0.925

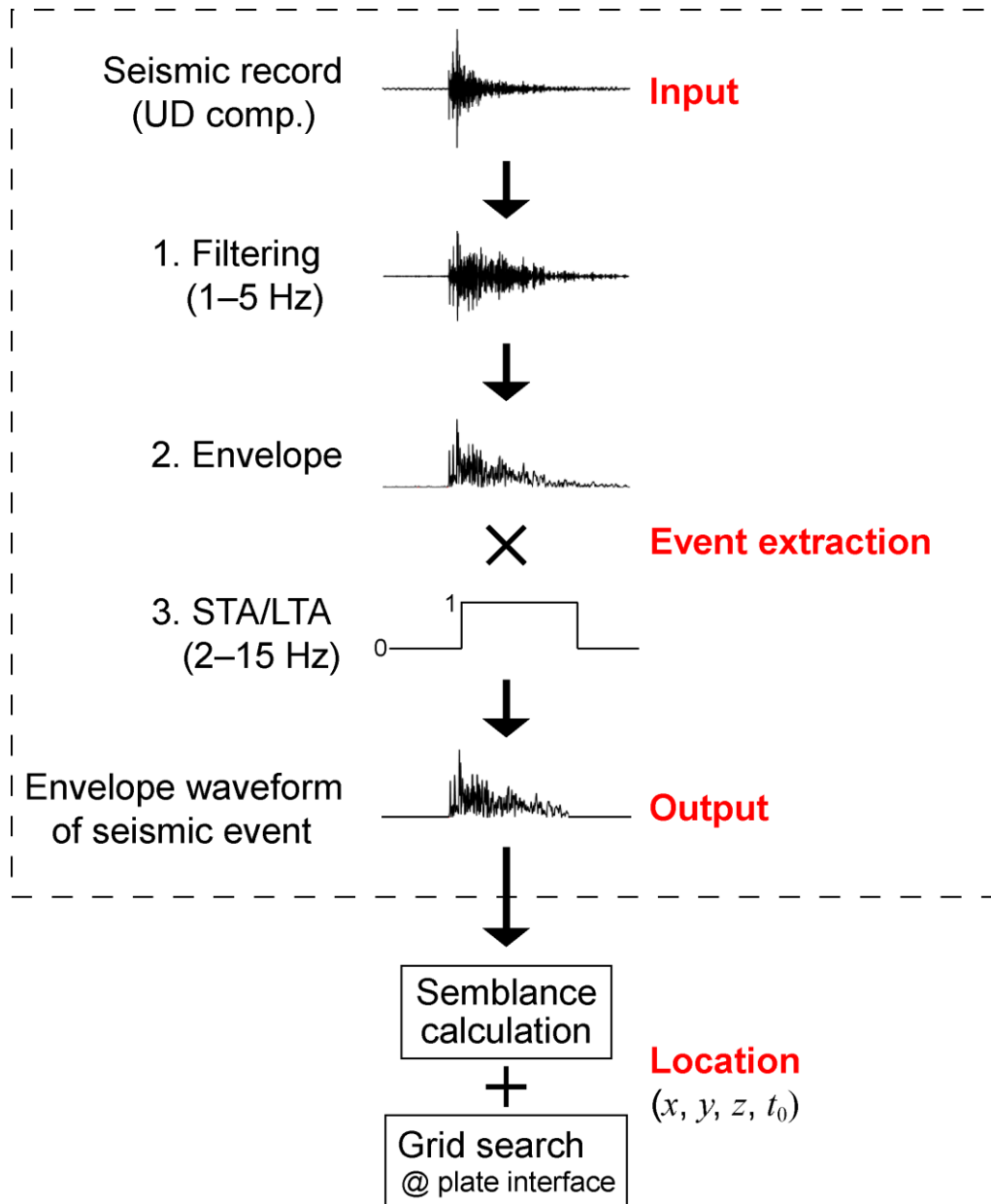


Figure 3.1. Diagram explaining the detection and location method applied to the continuous waveform data. Event extraction scheme which generates envelope waveforms of events as characteristic functions is enclosed in a dashed rectangle.

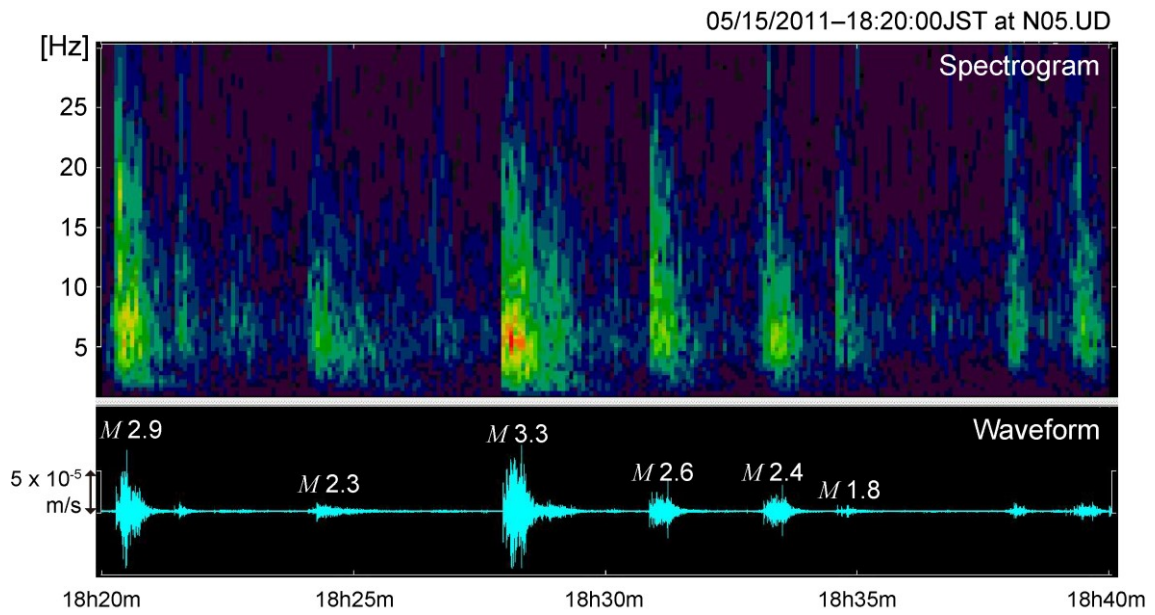


Figure 3.2. Time-frequency spectrogram (top) of an example raw vertical-component waveform recorded by an OBS (N05) station (bottom). Warmer colors in the spectrogram indicate larger amplitudes. Magnitudes of events listed in the JMA catalog are labeled at the corresponding waveforms of the events.

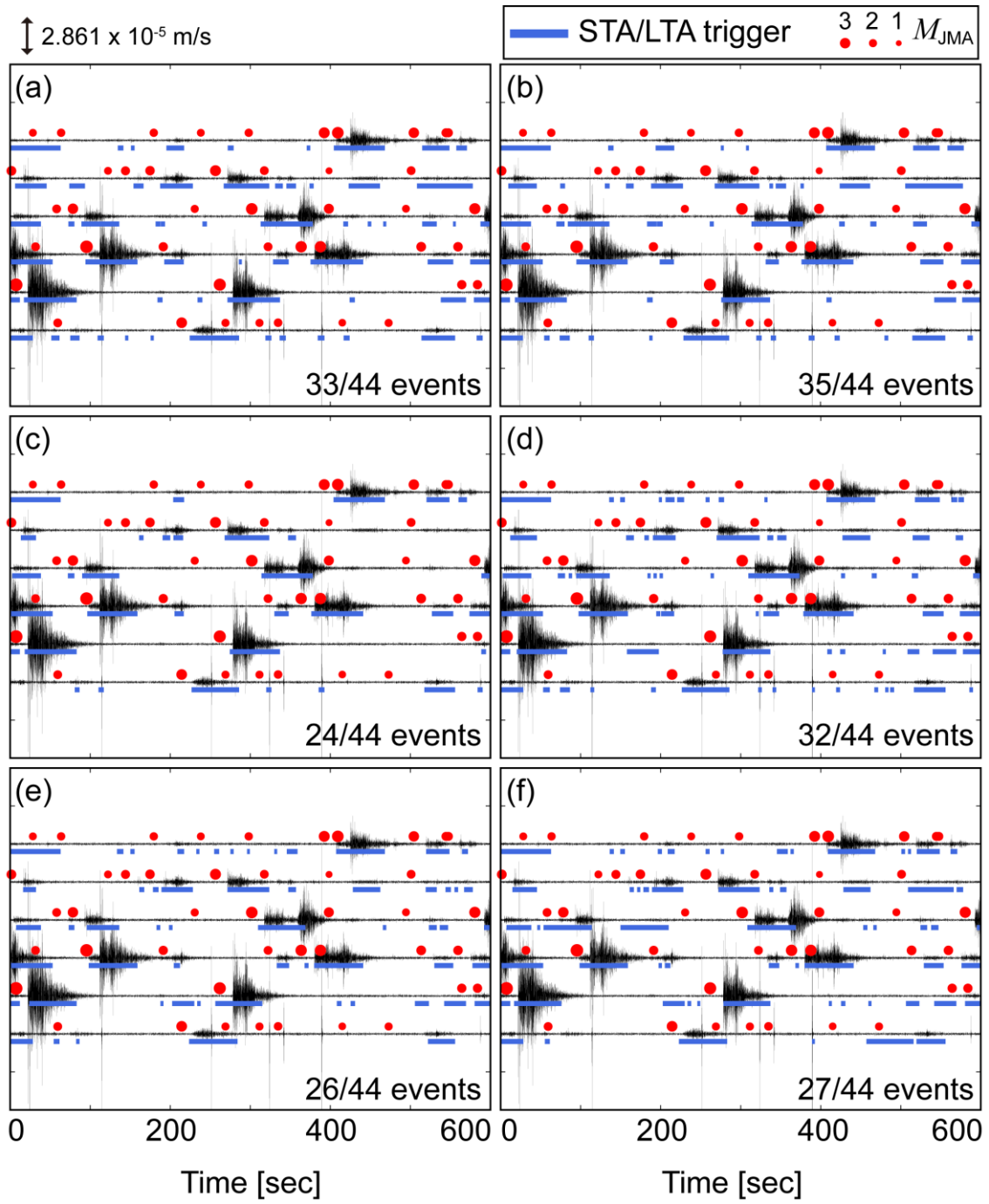


Figure 3.3. Example results of the STA/LTA algorithm for a 1-hour vertical-component waveform data (2–15 Hz) which includes the largest number of events listed in the JMA catalog recorded at an OBS (NS08) station in Region 3 for the first sub-period after the Tohoku earthquake. Each trace of the waveform is 10-minute long and the uppermost trace is the first 10 minutes. Red circles correspond to the origin times of 44 events listed in the JMA catalog. Diameters are proportional to the JMA magnitude. Blue bars show the duration of the STA/LTA trigger at the station. The number of detected events is shown in the lower right corner of each panel. Note that this is the result at an example station and the triggering of events was determined by more than 70% of the stations in the actual procedure. The STA window length, the LTA window length, and the threshold of STA/LTA ratio are (a) 5 seconds, 10 seconds, and 1.2, (b) 4 seconds, 20 seconds, 1.2, (c) 4 seconds, 20 seconds, 2.0, (d) 2 seconds, 20 seconds, 1.2, (e) 0.3 seconds, 60 seconds, 1.2, and (f) 0.2 seconds, 10 seconds, 1.2.

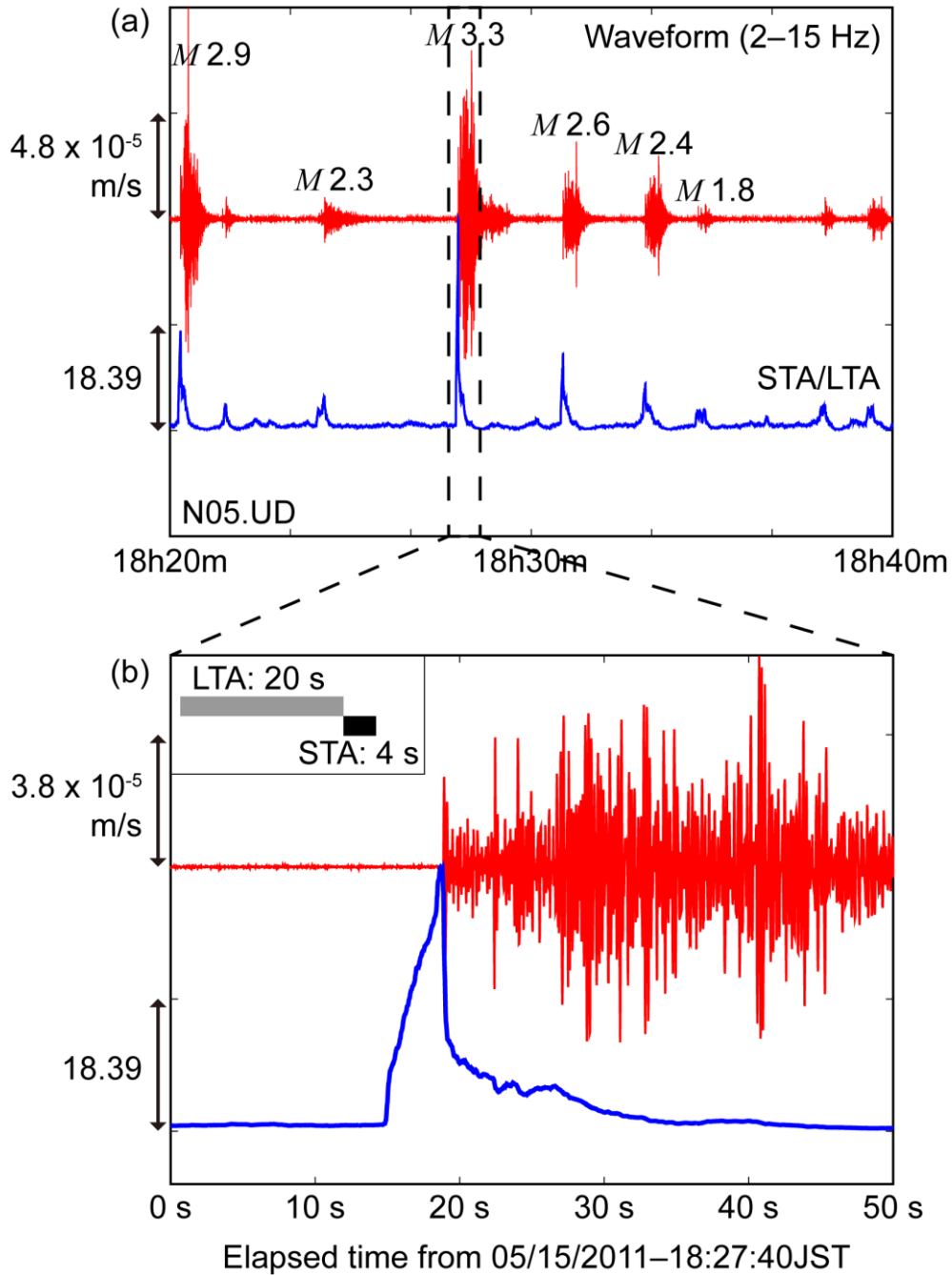


Figure 3.4. (a) An example bandpass filtered vertical-component waveform (red) and temporal change in STA/LTA ratio (blue) for the same time series in Figure 3.2. (b) An enlarged plot within the time window between the vertical dashed lines in panel (a). Inset shows the placement of the LTA and the STA windows in this study.

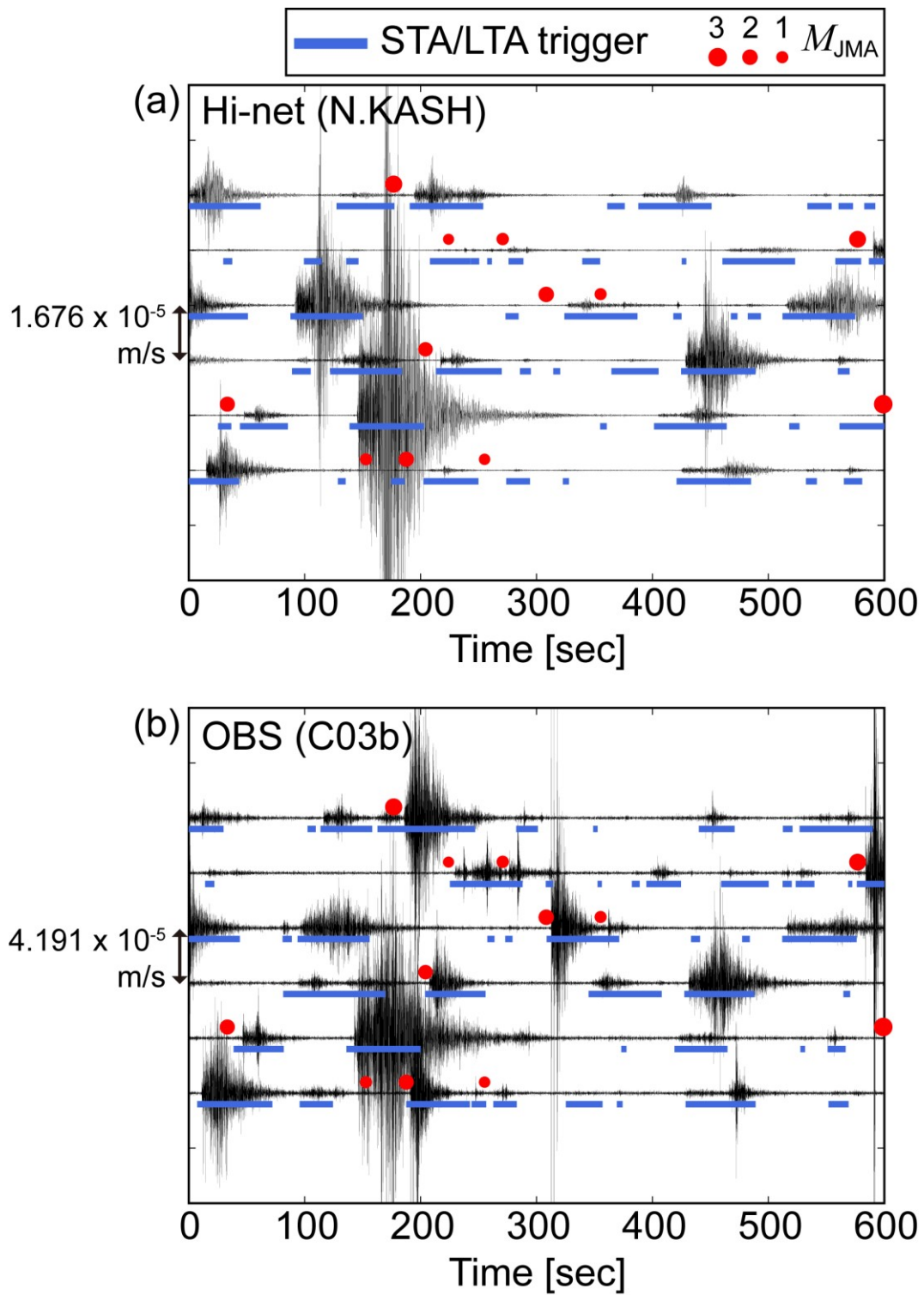


Figure 3.5. The same as in Figure 3.3 at (a) the Hi-net (N.KASH) and (b) an OBS (C03b) stations in Region 2 for the second sub-period after the Tohoku earthquake.

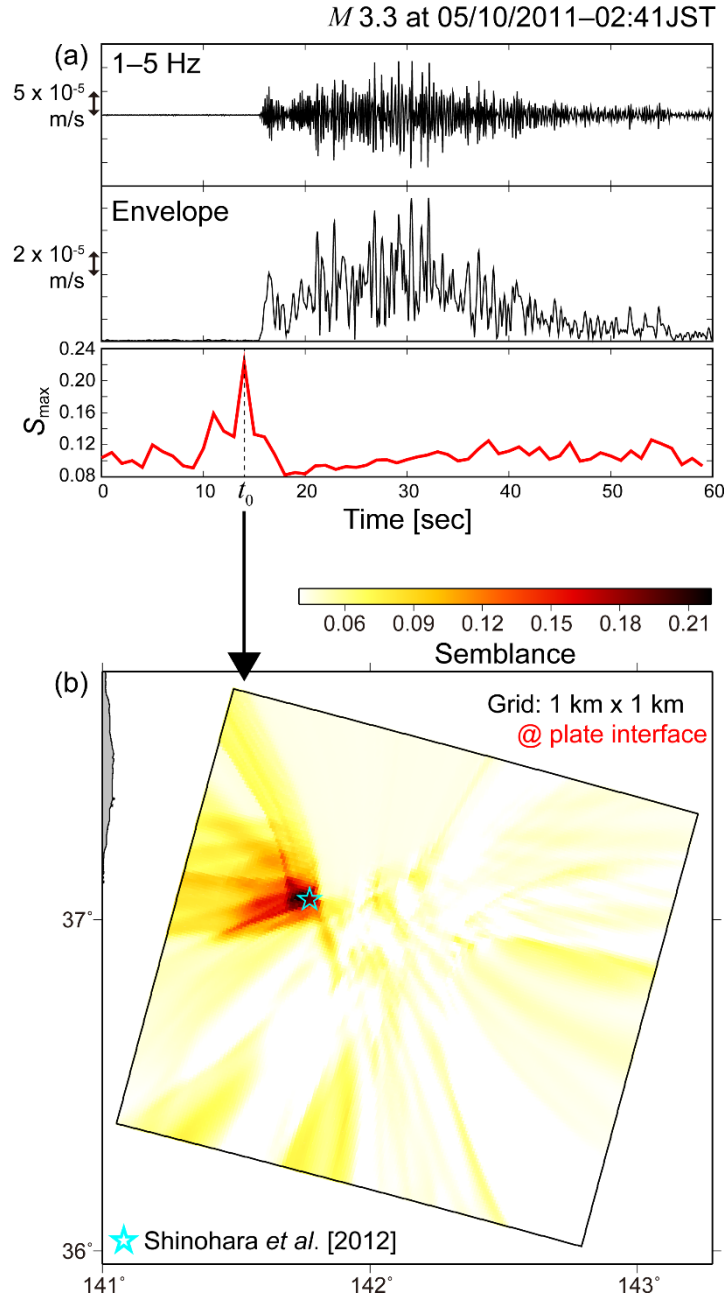


Figure 3.6. An example of the semblance calculation for an event listed in the JMA catalog with the magnitude of 3.3. (a) A bandpass filtered vertical-component waveform at the reference station of the array (top), the envelope waveform of the top panel (middle), and time series of the maximum semblance value (S_{\max}) (bottom). (b) Spatial distribution of the semblance values projected onto the plate interface at the time t_0 which gives the maximum S_{\max} during the event. The star shows the epicenter of the event determined by Shinohara *et al.* [2012].

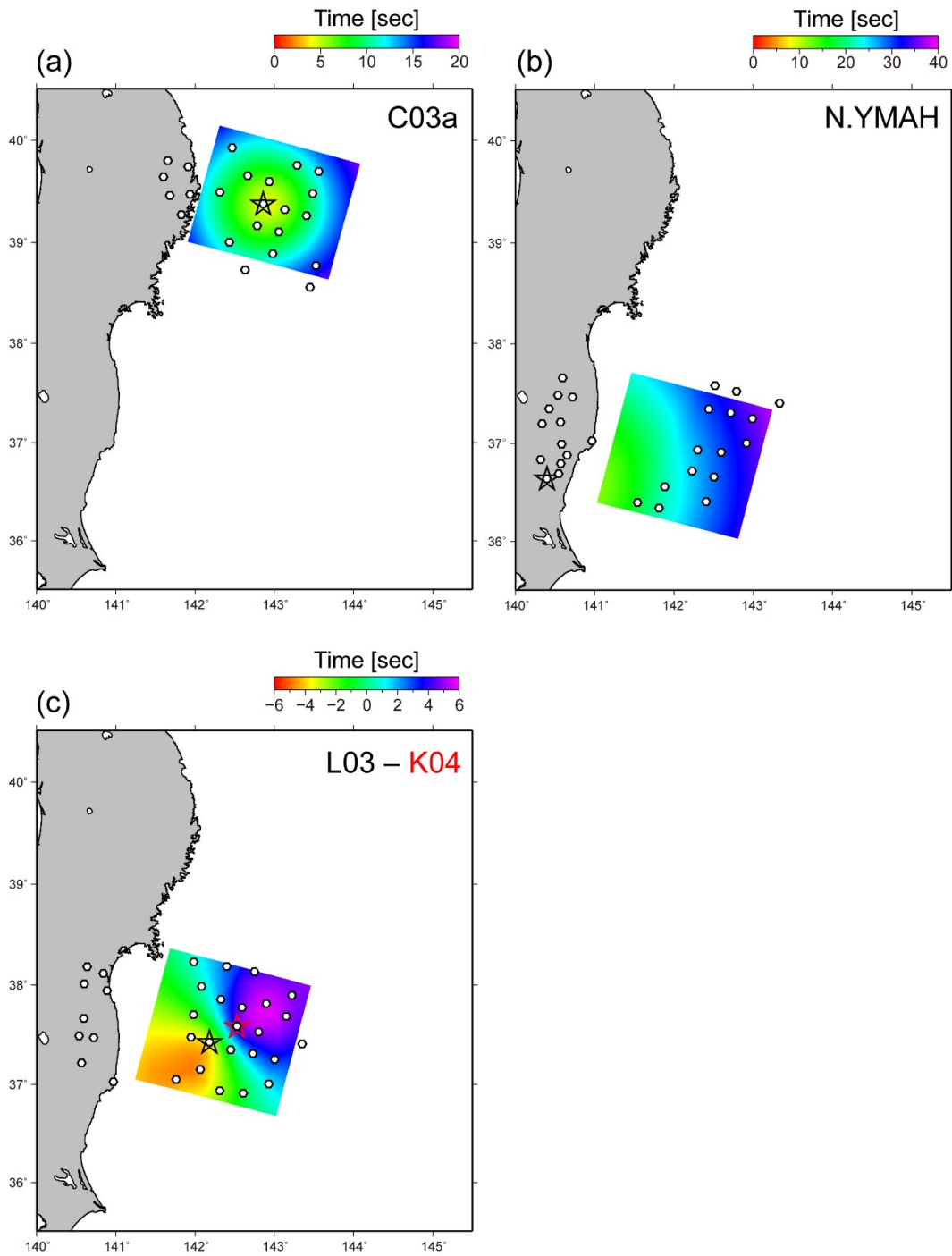


Figure 3.7. Example results of traveltime calculation at (a) an OBS (C03a) and (b) the Hi-net (N.YMAH) stations. (c) An example traveltime difference between the station (L03) and the reference station (K04) shown as a red star. Hexagons show the station distribution and black stars indicate the target stations.

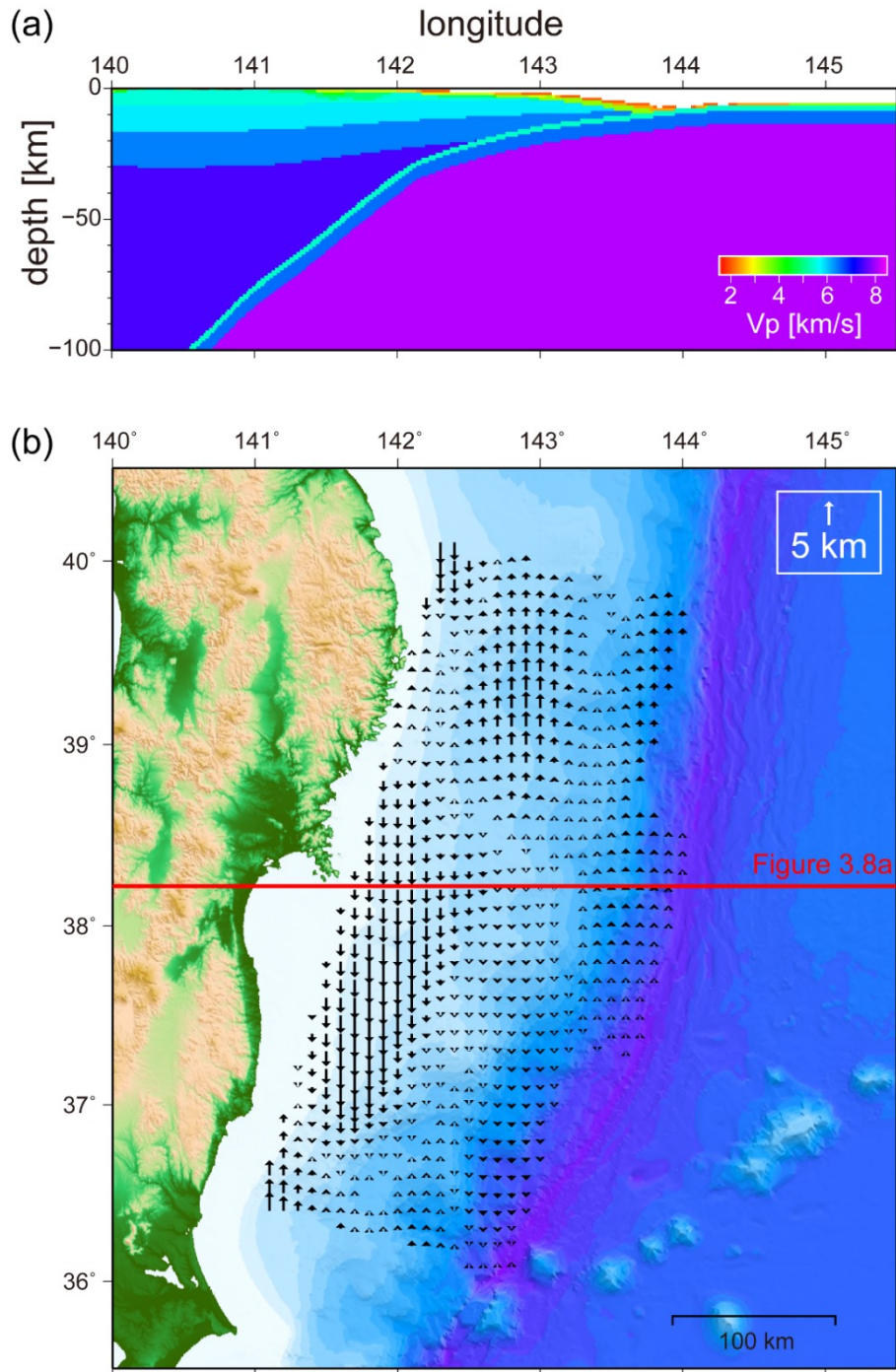


Figure 3.8. (a) P -wave velocity structure of JIVSM plotted in cross-section along a red line in panel (b). (b) Differences between depth of the Pacific plate of JIVSM and that of the model compiled by previous marine seismic observations using OBSs [Nakahigashi *et al.*, personal communication] in the study region (arrows).

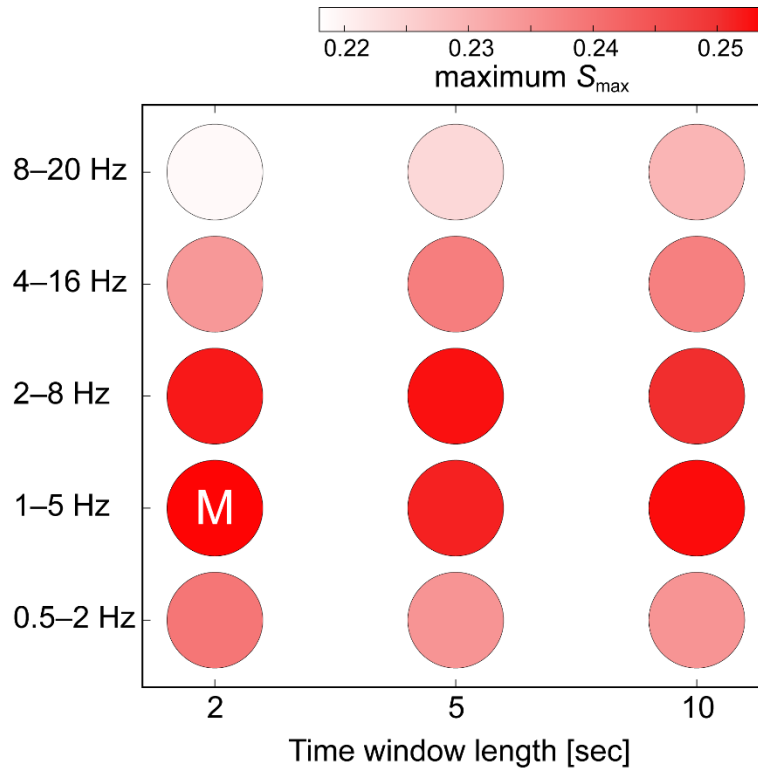


Figure 3.9. The average maximum S_{\max} values calculated by using several sets of a window length (the horizontal axis) and a frequency band of waveforms (the vertical axis) for 89 reference events described in Section 3.4. S_{\max} is the maximum semblance value within all the grids at each time step. Character “M” indicates the maximum value among the trials.

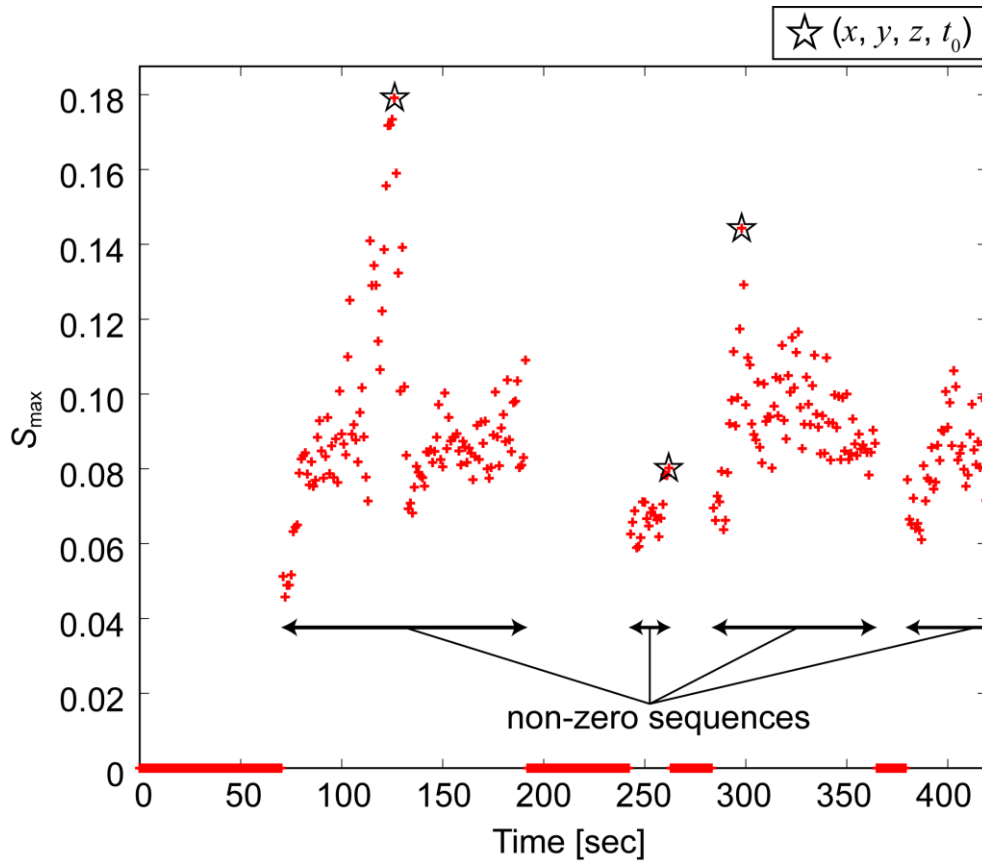


Figure 3.10. An example time series of the maximum semblance value (S_{\max}) within all the grids at each time step. The time series of S_{\max} consists of zero and non-zero (indicated by arrows) sequences according to the on-off states of the STA/LTA algorithm. The stars show the maximum S_{\max} during a sequence of non-zero S_{\max} corresponding to a timing of the P -wave onset t_0 at the reference station of the array and the hypocenter (x, y, z) .

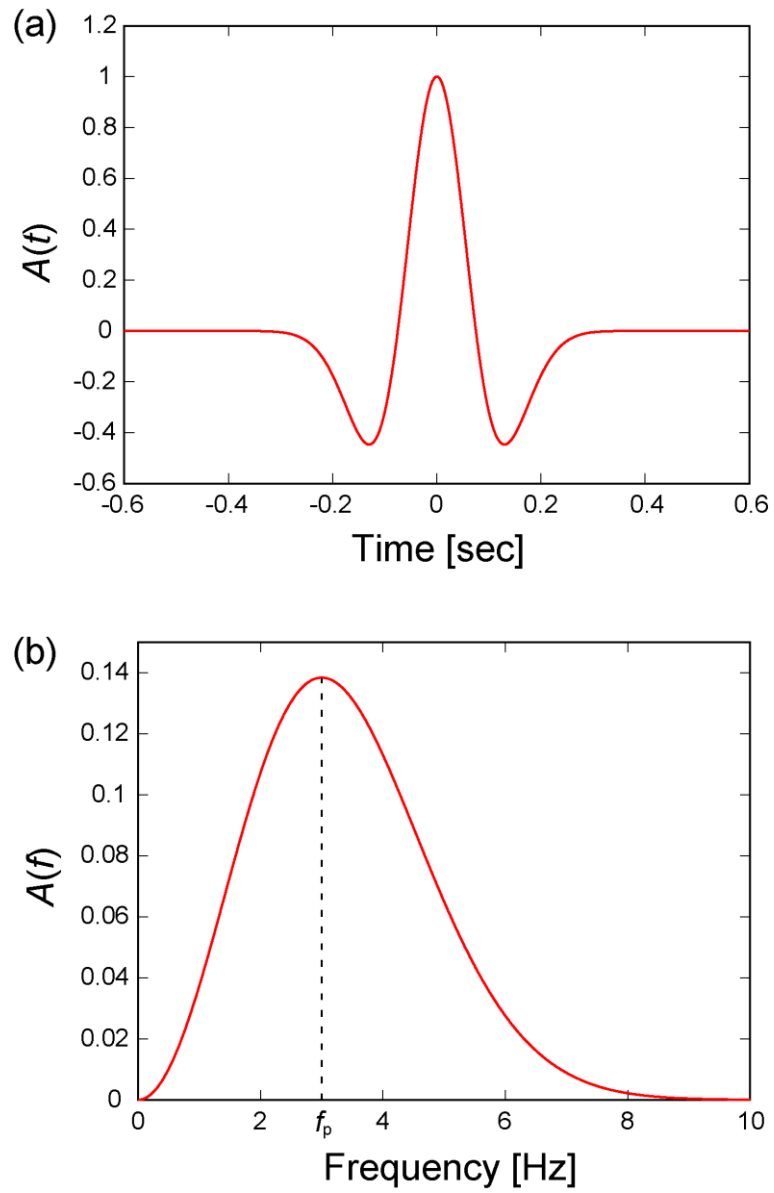
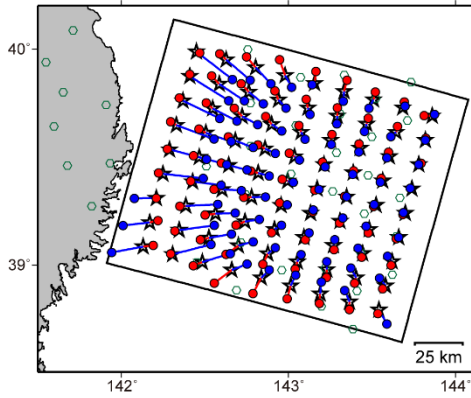


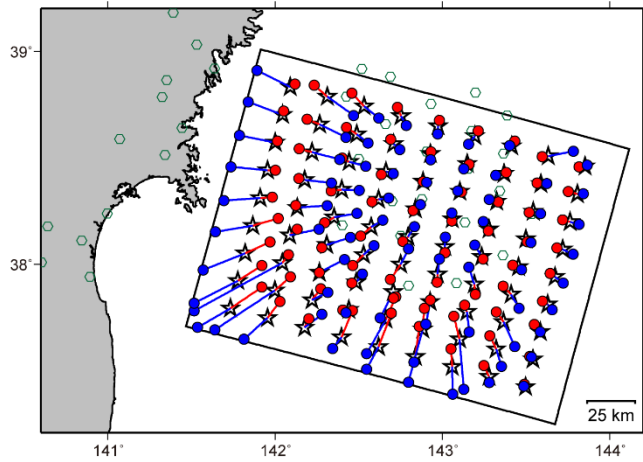
Figure 3.11. Representations of the Ricker wavelet in (a) time-domain and (b) frequency-domain. Peak frequency f_p is equal to 3 Hz in the synthetic tests.

The period before the Tohoku Eq.

(a) Region 1



(b) Region 3

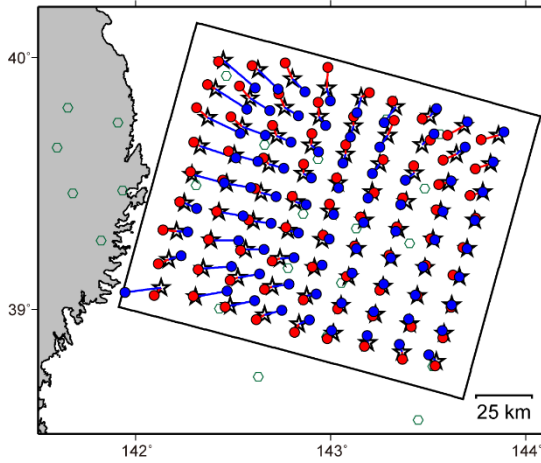


☆ initial epicenters
 $z_s = -10, +10$ km
in the hanging wall
in the slab

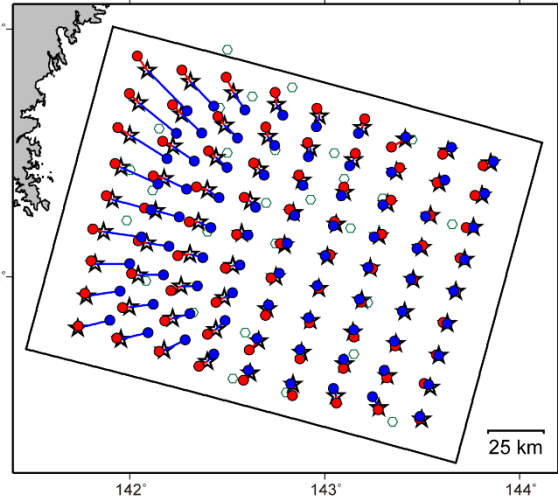
Figure 3.12. Distribution of the resultant epicenters of the synthetic tests for the period before the Tohoku earthquake in (a) Region 1 and (b) Region 3. The resultant epicenters are color coded according to the initial focal depths relative to the plate interface by -10 (shallower, red circles) and 10 km (deeper, blue circles). Black stars indicate the initial epicenters. The initial and resultant epicenters are connected with red and blue lines. Green hexagons show the station distribution.

The 1st sub-period after the Tohoku Eq.

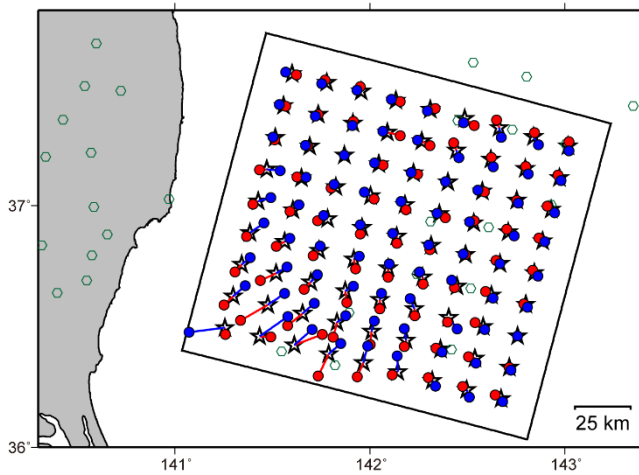
(c) Region 1



(d) Region 3



(e) Region 5

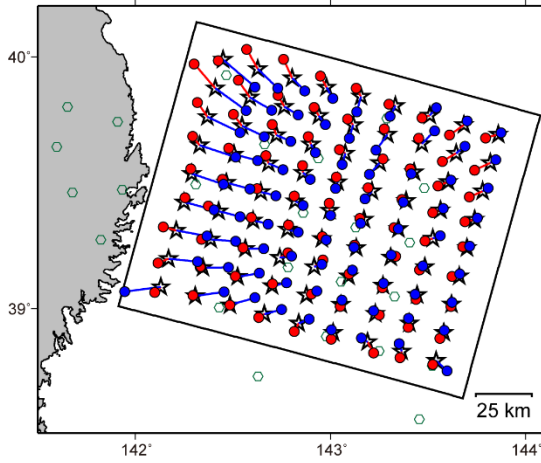


☆ initial epicenters
 $z_s = -10, +10$ km
 in the hanging wall
 in the slab

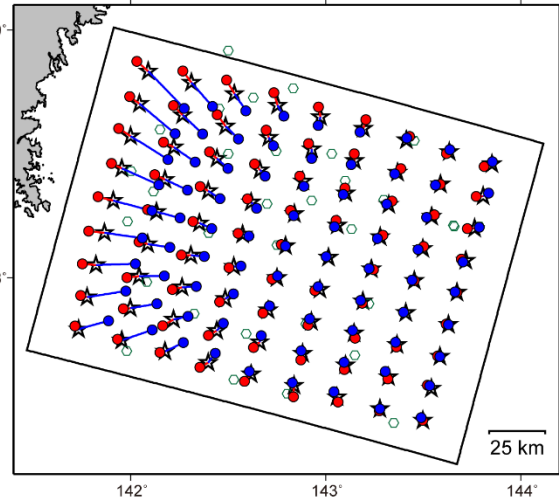
Figure 3.12. (continued) The same as in panel (a) for the first sub-period of aftershock observation of the Tohoku earthquake in (c) Region 1, (d) Region 3, and (e) Region 5.

The 2nd sub-period after the Tohoku Eq.

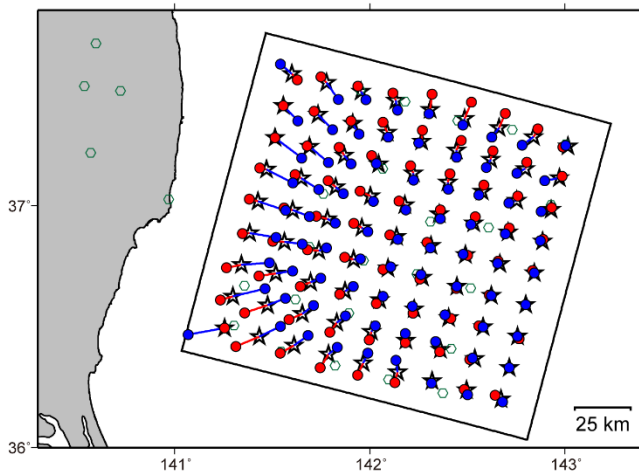
(f) Region 1



(g) Region 3



(h) Region 5



☆ initial epicenters
 $z_s = -10, +10$ km
in the hanging wall
in the slab

Figure 3.12. (continued) The same as in panel (c) for the second sub-period of aftershock observation of the Tohoku earthquake in (f) Region 1, (g) Region 3, and (h) Region 5.

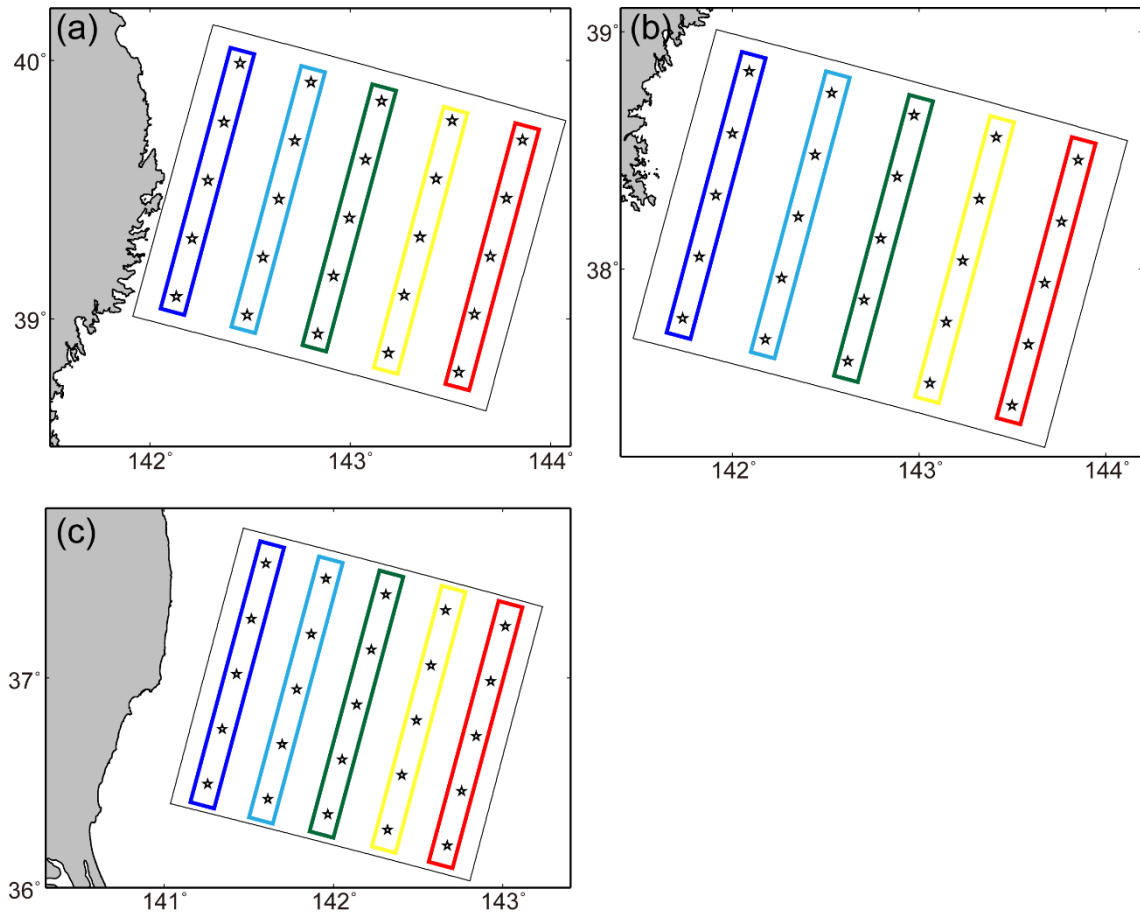


Figure 3.13. Distribution of the initial epicenters of the synthetic test on focal depth dependence on maximum semblance values in (a) Region 1, (b) Region 3, and (c) Region 5. Black stars indicate the initial epicenters. The initial hypocenters are grouped according to the distance from the trench axis (color rectangles).

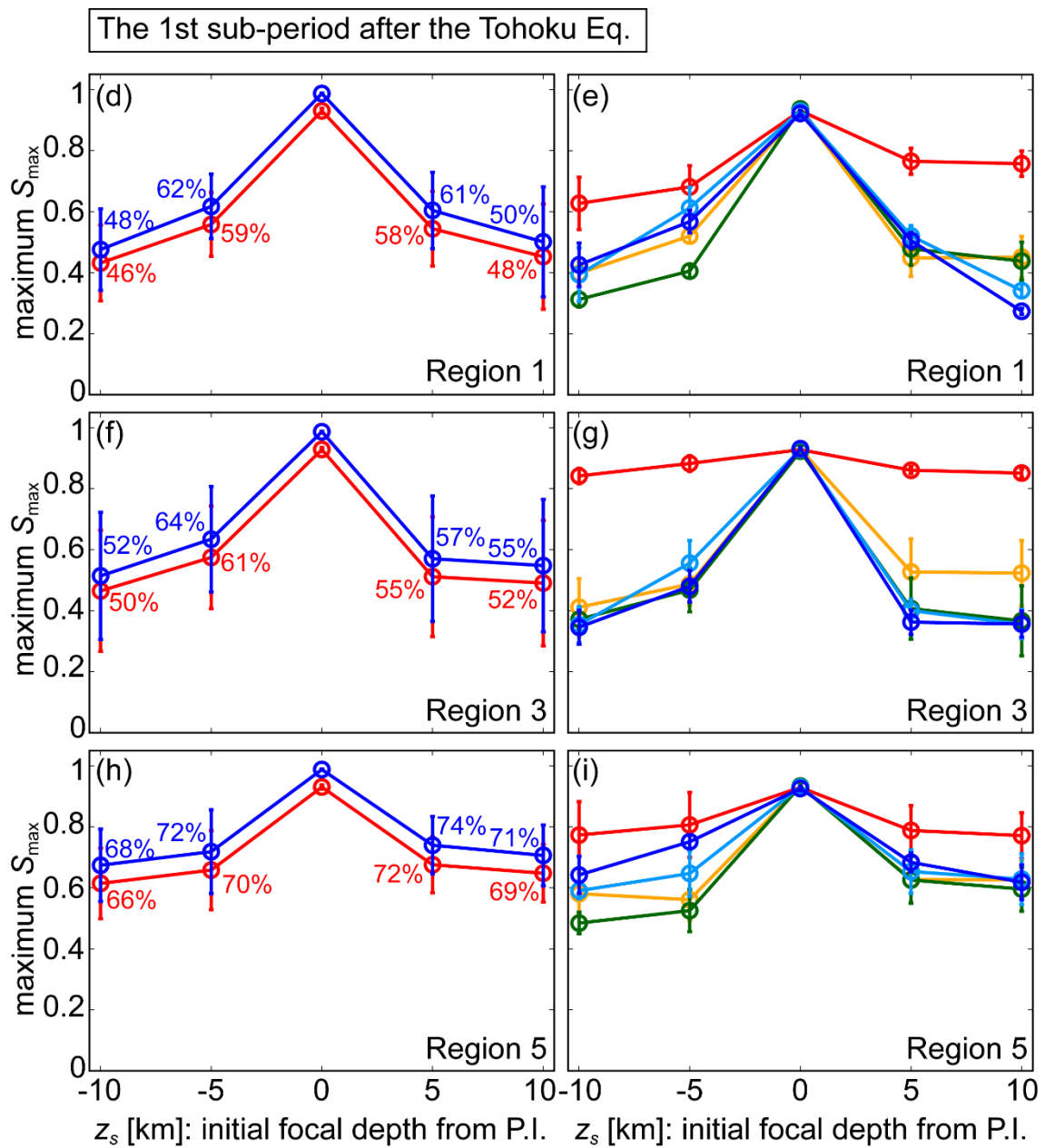


Figure 3.13. (continued) Results of the synthetic tests for the first sub-period after the Tohoku earthquake according to the initial focal depths in km from the plate interface. Left panels show the average maximum semblance values over all the epicenters. Blue and red lines correspond to the results when the signal-to-noise ratios are 5 and 2, respectively. Ratios of the maximum semblance values to those whose initial depths are just on the plate interface are labeled. Right panels show the average maximum semblance values over the group of epicenters in panels (a)–(c).

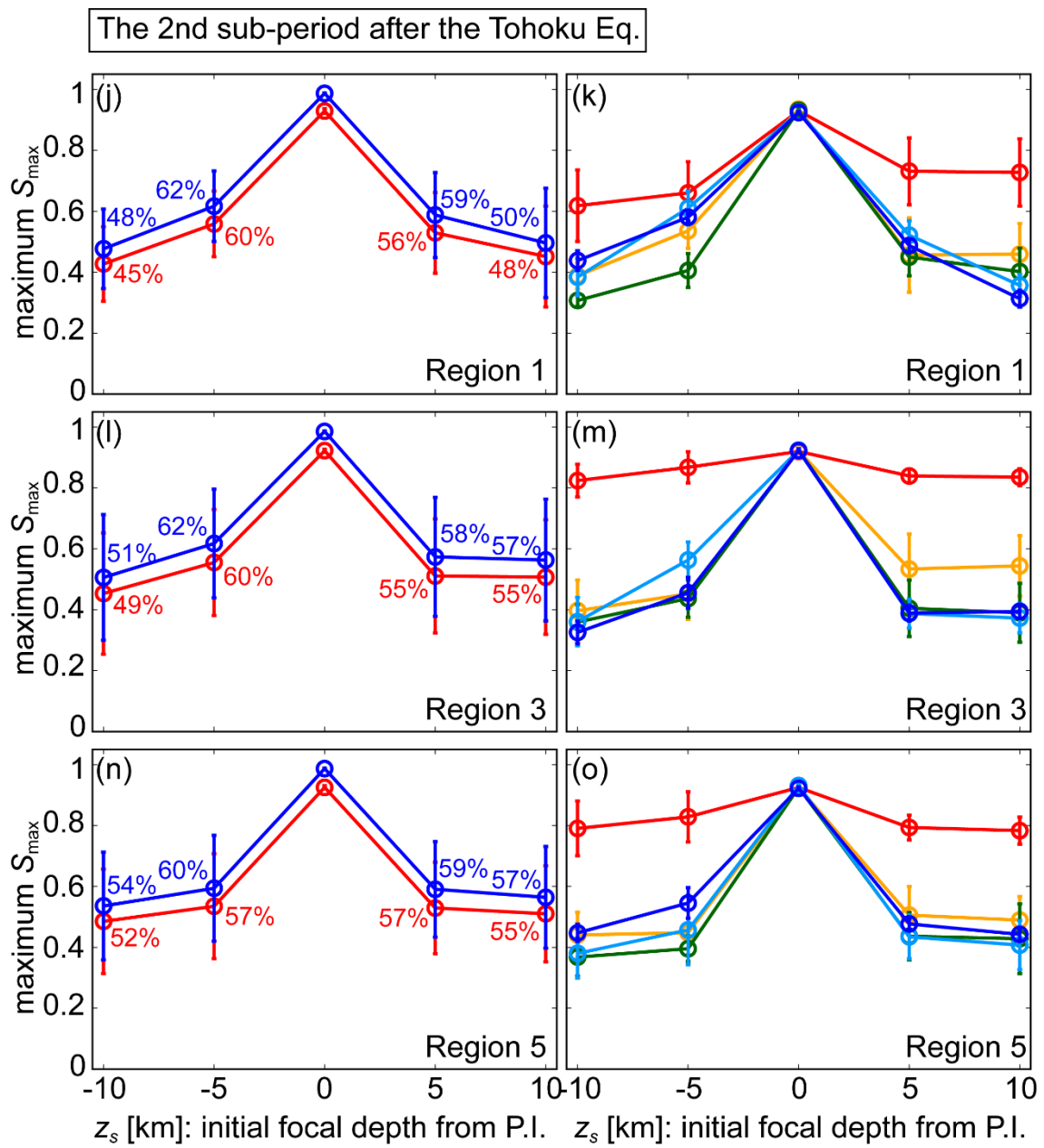


Figure 3.13. (continued) The same as in panels (d)–(i) for the second sub-period after the Tohoku earthquake.

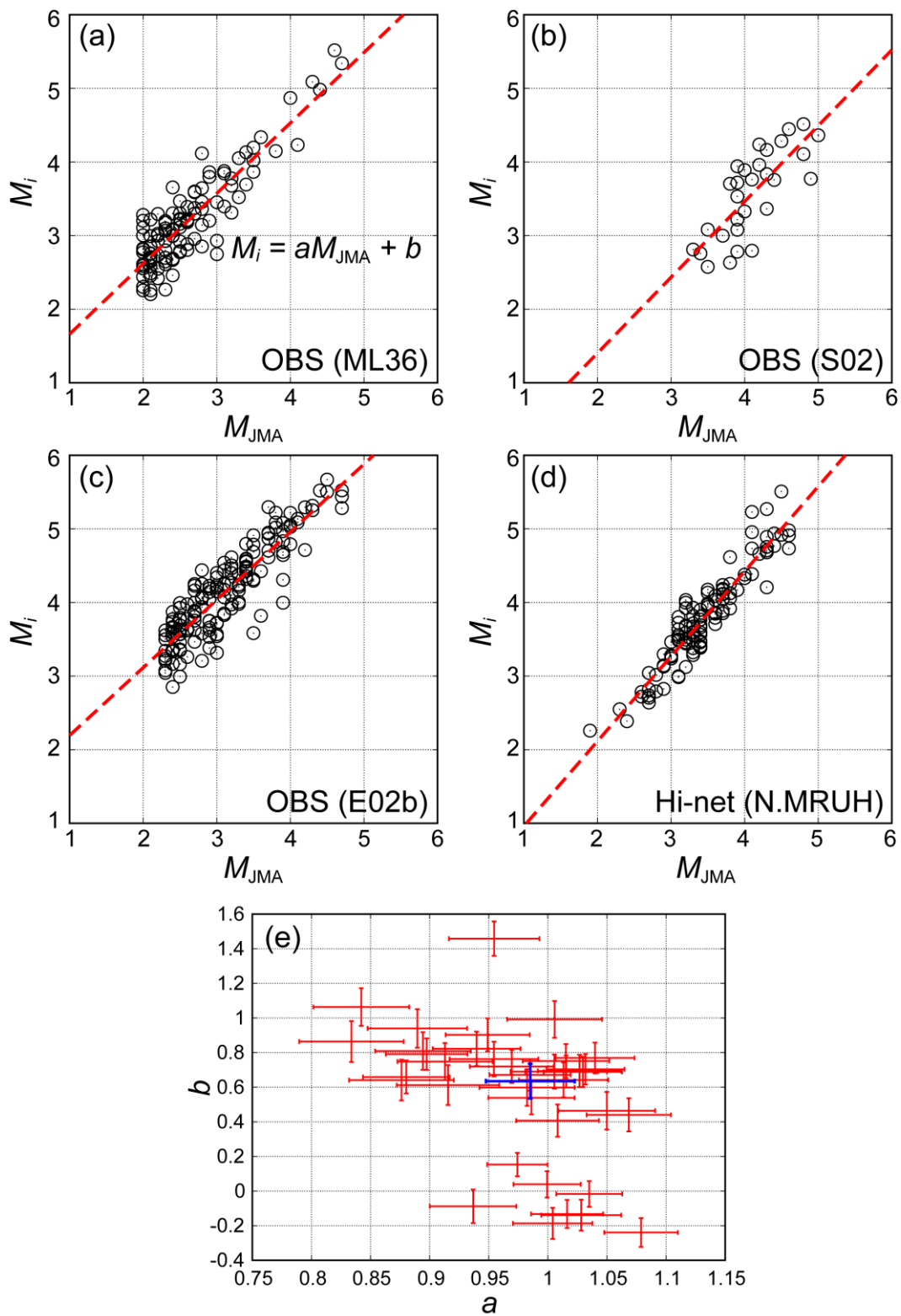


Figure 3.14. (a)–(d) Relationship between magnitudes derived from equation (5) at example OBS stations and the Hi-net station and those of the JMA catalog for common events (circles). Red dashed line shows the initial regression line with the coefficients a and b . (e) Plots of the coefficients, a and b , and their standard deviations for all the stations in Region 1 for the pre-Tohoku period. The blue plot shows the result at the same station used in panel (a).

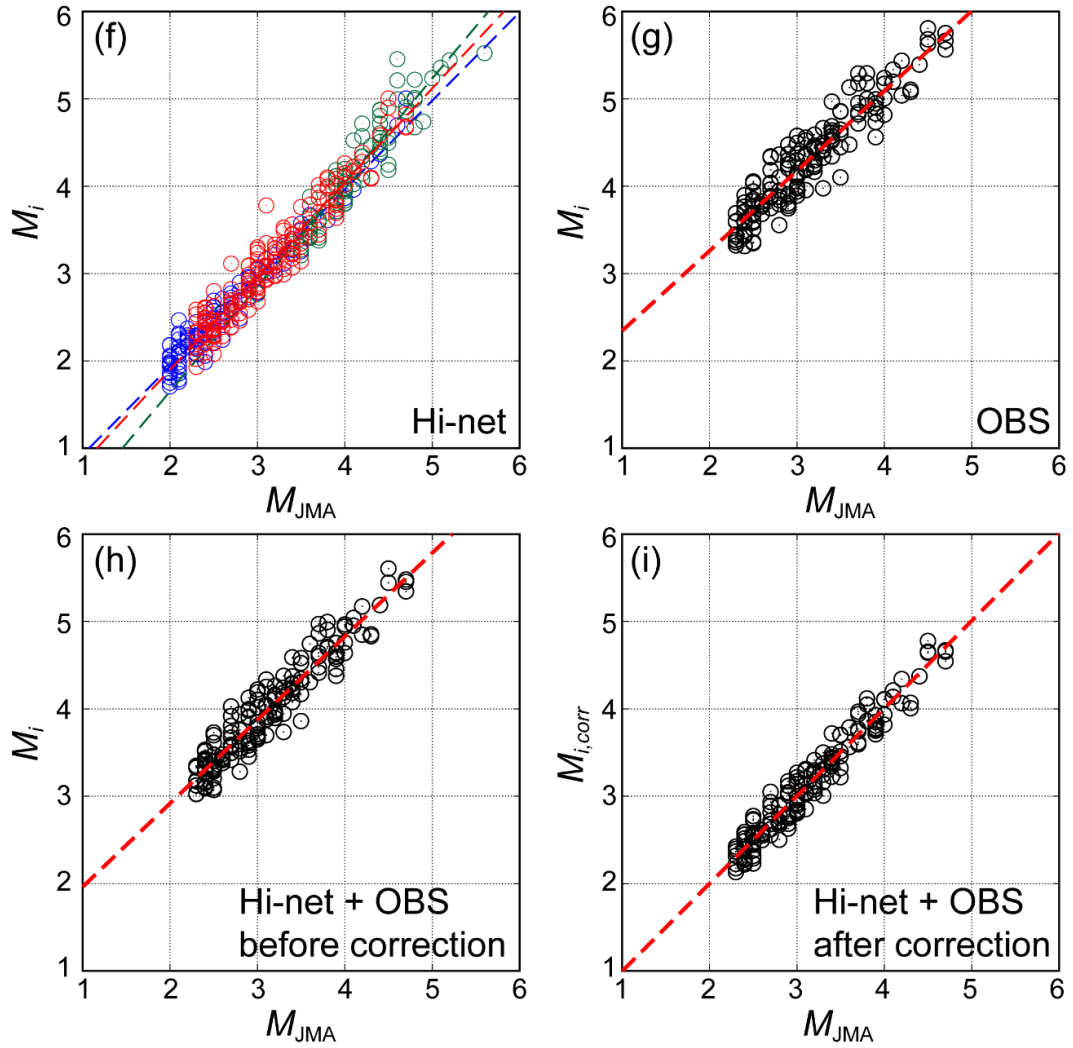


Figure 3.14. (continued) The same as in panel (a) for the mean of (f) all the Hi-net stations in Region 1 before (blue) and after (1st, green; 2nd, red) the Tohoku earthquake. The same as in panel (f) for (g) all the OBS stations, (h) both OBS and Hi-net stations before the magnitude correction, and (i) those after the magnitude correction in Region 1 for the second sub-period of aftershock observation.

4. Seismicity before and after the 2011 Tohoku Earthquake

4.1 Newly Obtained Earthquake Catalog

On the basis of the procedures described in the previous chapter, I obtained a new earthquake catalog. The following detailed steps were introduced through the development of the catalog for each region and period:

- Step 1: The source parameters (x, y, z, t) for all the detected events were obtained by the source extraction process in Section 3.4, where (x, y, z) is the hypocenter and t is the origin time. The mean magnitudes of the selected stations in the array, M_{mean} , were also calculated for each event by the magnitude determination process described in Section 3.6. Note that the current catalog includes both seismic events and events originated from noise because any threshold of semblance values or criteria of the magnitudes have not been introduced yet.
- Step 2: Events that occurred outside the target region may have semblance values larger than the threshold around the outermost margins with the peak values along the boundary of the region. Such unwanted events have been removed before introducing the magnitude criteria in the next step.
- Step 3: In order to ensure association of events at multiple stations about common events, the criteria of the magnitude determination, $\sigma_M < 0.35$ and $N_{\text{sta}} \geq 3$, as stated in Section 3.6 are employed here. This accurate magnitude determination can contribute to discussion on the frequency-magnitude relation in the next chapter.

Step 4: As the final step, events which have semblance values larger than thresholds should be extracted from the present catalog that includes noise events. This procedure has the same meaning of discarding noise events from the catalog. I determined the thresholds of the semblance values for each region and period (Table 4.1). The detailed process of this determination will be described in the next section. I extracted events from the present catalog according to the thresholds and used them as the final version of the earthquake catalog.

The number of events at all the above steps for the post-Tohoku period is summarized in Table 4.1. In Step 1, more than tens of thousands of events were detected in each region and for each sub-period of aftershock observation. Because such a large number of detected events make it difficult to conduct conventional event association at multiple stations, the method I developed in this study contributes to a better understanding of seismicity even immediately after the megathrust earthquake.

In order to verify that the final resultant events through the above steps are true earthquakes, I visually confirmed whether the semblance peaks correctly corresponded to the true seismic events. I selected 50 events at random from the earthquake catalog of the post-Tohoku period for this verification. The result of the sampling inspection shows that the maximum S_{\max} values successfully corresponded to vicinity of the P -wave arrival times in 45 events and that the other 5 events resulted in misdetection, where S_{\max} is the spatial maximum semblance values at each time step. All the magnitudes of these 5 miss-detected events were below 2.5, and it implies the detectability of earthquakes decreases with decreasing magnitudes. Figure 4.1 shows all the results of the 50 events in the sampling inspection.

4.2 Comparison of Earthquake Catalog with Previous Studies

One of the objectives of this study is to detect and locate earthquakes including small ones. It is necessary to compare the resultant earthquake catalog with the existing catalogs to ensure the validity of the applied method and to evaluate the detectability of small earthquakes.

First, search-and-match of the events between the catalog of this study and the reference catalogs was conducted in accordance with small differences in the origin times $< |10 \text{ s}|$ (a mandatory requirement), in the hypocenters, and in the magnitudes of the events. Here, I adopted the catalog in Step 1 for this comparison so as to maximize the number of matching events, and the reference catalogs are the same as in Section 3.4; repeating earthquakes determined by Uchida and Matsuzawa [2013], the F-net events ($VR \geq 80\%$, $N_{\text{sta}} \geq 3$), and events with known focal mechanisms in Nakamura *et al.* [2016]. This matching analysis shows that 92.1% (35/38 events), 88.6% (234/264 events), and 82.8% (303/366 events) of the earthquakes in the reference catalogs in Regions 1, 3, and 5 were detected and located by this study for the pre-Tohoku period, the first, and the second sub-periods after the Tohoku earthquake, respectively (Table 4.2a). The matching rates for the same periods in the additional regions (Regions 2 and 4) are 93.3%, 83.8%, and 95.3% (Table 4.2b). Looking closely at the types of the missed events, the F-net normal and strike-slip faulting events and thrust faulting events in Nakamura *et al.* [2016] occupied a relatively large portion of them. According to Nakamura *et al.* [2016], thrust faulting events from their catalog were predominantly deeper than the depth of the plate interface by ~ 10 km, although the depth constraint in the offshore area was poor due to the lack of OBS data. Therefore, the missed events of

this study can be characterized by their distant focal depths from the plate interface rather than by faulting types. This depth dependence of earthquake detection shows good coincidence with the results of the synthetic tests described in Section 3.5. On the other hand, such a high matching rate, except for events off the plate interface, indicates that the method of this study meets the performance standards to detect and locate earthquakes nearly around the plate interface. In addition to the matching rate, I investigated maximum S_{\max} values during the events listed in the same reference catalogs. The results of the mean values of the maximum S_{\max} for each focal mechanism is shown in Figure 4.2. The results of the repeating earthquakes and the F-net thrust faulting events show relatively high mean values of the maximum S_{\max} compared with those of the other faulting types for the post-Tohoku period, although the differences are within the standard deviation range. This trend can also correspond to the depths of the earthquakes in the same way as the above argument about the matching rate. From the results of this comparison, I determined the thresholds of the semblance values for each region and period so that they were low enough below the mean maximum S_{\max} values for all the focal mechanisms (Table 4.1). The resultant thresholds were introduced to Step 4 in the previous section.

Second, I carried out another search-and-match experiment between the catalog in Step 1 and that of Shinohara *et al.* [2011, 2012] in the same manner as the previous experiment. For aftershocks of the Tohoku earthquake within a band of 10 km on both sides of the plate interface listed in Shinohara *et al.* [2011, 2012], the matching rates of events in Regions 1, 3, and 5 are 82.4% (84/102 events) for the first sub-period and 79.7% (220/276 events) for the second sub-period. In the additional regions (Regions 2 and 4), the matching rates are 77.2% (first) and 80.9% (second). I also manually checked the reason for miss-detection or miss-location of the remaining 20% of the

events in this study. First of all, I confirmed that all these missed events were certainly detected by the STA/LTA triggering algorithm. Therefore, the failures certainly occurred during the semblance calculation process. On closer inspection, the missed events were classified roughly into two groups. One was a group of the events whose waveform coherence was too low among the stations of the array. As a result, the maximum S_{\max} values of the events were observed at the times off the true P -wave onsets with very low values, and therefore the resultant epicenters shifted from the true locations. Such low waveform coherence may not be able to be overcome because it originated from the quality of the original waveforms. The effective solution for this problem can be weighting the original waveforms for each station and/or incorporating characteristic functions rather than the original waveforms, and that will be an issue in the future work (see Section 6.2). The other group of the missed events was resulted from the assumption that there is only one event during a non-zero S_{\max} sequence (Figure 3.10). When multiple events were included in the same sequence, the method used in this study could select only the largest peak of the semblance values, which means that the matching rate of the events might be decreased.

In terms of the accuracy of epicenters, differences in epicentral locations between catalogs of this study and Shinohara *et al.* [2011, 2012] were investigated. The same aftershocks as used in the above matching analysis, which occurred within a band of 10 km on both sides of the plate interface, were selected for comparison. Differences in epicentral locations in each region and period are shown in Table 4.3. The overall mean distance is 15.7 km for 551 events. Therefore, while considering the results of the synthetic tests as described in the previous chapter (Figure 3.12), I estimate that earthquakes listed in the catalog of this study have errors in location of approximately 20 km.

Next, magnitude-dependence of the matched/missed events in the above matching analysis should also be checked in order to discuss frequency-magnitude relation of earthquakes in Chapter 5. Histograms of magnitude of the matched (red) and missed (blue) events are shown in Figure 4.3. Green circles denote the ratio of the number of matched events to that of all the events. In Figure 4.3a, using the same reference catalogs in Table 4.2a for the first sub-period after the Tohoku earthquake, the resultant ratio starts to decrease around $M \sim 5$ and is at almost stable value of 0.9 in the magnitude range of 3.5 to 5. In contrast, the matching ratio clearly decreases with decreasing magnitude in the range smaller than $M \sim 5$ for the second sub-period (Figure 4.3b). This result indicates that the detectability of earthquakes can be modeled as a function of magnitudes. Comparing with the events within a band of 10 km on both sides of the plate interface listed in Shinohara *et al.* [2011, 2012], the ratio seems to be unstable in the magnitude range of 2.5 to 4 (Figures 4.3c and 4.3d). Although there exist considerable variations of the matching ratio, these results suggest the magnitude-dependence of the detection of earthquakes. Therefore, the influence of such miss-detection on the frequency-magnitude distribution will be discussed in Chapter 5 by introducing a statistical model into the detection-rate.

Finally, in order to confirm the detection performance by another automated method and to evaluate the superiority of the method of this study in detection and location of earthquakes, I applied a conventional method to the seismic data of this study and compared results. As such a conventional method, I used the WIN system for automatic phase picking and location [Urabe and Tsukada, 1992]. In the WIN system, the following procedures were included: detecting seismic events by the STA/LTA algorithm, extracting waveforms of the events, automatically picking P - and S -wave arrival times using the autoregressive model [e.g., Takanami and Kitagawa, 1988], and

determining hypocenters by HYPOMH [Hirata and Matsu'ura, 1987] using a 1-D velocity structure. For the STA/LTA calculations, I selected the following set of parameter values with reference to those used in routine processing at Earthquake Research Institute, the University of Tokyo; the STA window length of 0.3 seconds, the LTA window length of 60 seconds (1000 seconds during the triggering), and the thresholds of STA/LTA ratio of 2.0 and 3.0 before and after the Tohoku earthquake. The triggering of an event starts when the STA/LTA ratio exceeds the threshold for more than 2 seconds and ended when the STA/LTA ratio falls below the threshold for more than 10 seconds. The waveforms of the detected event are then cut out from $T_{\text{on}} - 20$ seconds to $T_{\text{off}} + \sqrt{3}(T_{\text{off}} - T_{\text{on}})$ seconds, where T_{on} and T_{off} are the start and end times of the trigger, respectively. For the hypocenter determination, a 1-D velocity structure was extracted from Miura *et al.* [2003] which was used in Shinohara *et al.* [2012]. The available *P*- and *S*-wave station corrections which were determined from the OBS data of Shinohara *et al.* [2012] were also incorporated. In this analysis, the study region and the analysis period were not divided into any sub-regions and sub-periods. In other words, the period of analysis also included the term between the first and the second sub-periods of the aftershock observation so that more earthquakes are included in the data itself.

As a result of the automatic detection and location by the WIN system, I first examined the detectability of earthquakes listed in the existing earthquake catalogs. The search-and-match experiment between the catalogs was conducted in the same manner as described earlier in this section. Here the catalog of the WIN system contains both converged and non-converged events without any selection, and the repeating earthquakes and the F-net thrust faulting events are selected as the reference. The matching rates in the study region for the pre- and post-Tohoku periods were 86.1%

(31/36 events) and 20.3% (46/227 events), respectively. The detectability of earthquakes is decreased by 60% after the occurrence of the 2011 Tohoku earthquake, while that of this study remains high—more than 90% (Table 4.2a). Next, I checked the characteristics of the catalog by the WIN auto-picking in terms of the hypocenters and their frequency-magnitude distribution. Note that the following resultant hypocenters are converged ones and extracted within a band of 10 km on both sides of the plate interface. Figure 4.4 shows the hypocenter distribution and its frequency-magnitude distribution before and after the Tohoku earthquake. For the post-Tohoku period, despite absence of any magnitude corrections to the magnitudes determined by the WIN system, the non-cumulative distribution has a peak at $M \sim 2.5$ which is comparable to that of this study (red circles and crosses in Figure 4.4d). The true peak of the distribution of the result from the conventional method will be located at a lower magnitude than 2.5 after magnitude correction. However, the result of the matching analysis with the existing catalogs show a low matching rate ($\sim 20\%$) as described above. In addition, few seismic events were determined in most parts of Region 1 for the post-Tohoku period in spite of the fact that aftershocks occurred around the plate interface [e.g., Shinohara *et al.*, 2012] (Figure 4.4c). Such a large number of events with small magnitudes are considered to be resulted from misdetection of the background noise as seismic events. In conclusion, the conventional WIN system with automatic phase picking and location was not an effective method to deal with high seismic activities immediately after the 2011 Tohoku earthquake. In contrast, the method of this study can contribute to a better understanding of seismicity even immediately after the Tohoku earthquake.

4.3 Seismicity for the pre-Tohoku Period

本節については、5年以内に雑誌等で刊行予定のため、非公開。

本節については、5年以内に雑誌等で刊行予定のため、非公開。

4.4 Seismicity for the post-Tohoku Period

本節については、5年以内に雑誌等で刊行予定のため、非公開。

本節については、5年以内に雑誌等で刊行予定のため、非公開。

本節については、5年以内に雑誌等で刊行予定のため、非公開。

本節については、5年以内に雑誌等で刊行予定のため、非公開。

Table 4.1. The number of days, the thresholds of the semblance values, and the number of events at all the steps in the development of the earthquake catalog for the post-Tohoku period.

	Region	Number of Days	Semblance Threshold	Step 1	Step 2	Step 3	Step 4 (Final)
After 1st	1	26	0.185	40278	37065	36941	2262
	2	27	0.148	37077	35014	34887	2413
	3	15	0.182	19938	18948	18885	1896
	4	31	0.140	25809	24239	23678	2493
	5	19	0.150	22000	20742	19407	1398
After 2nd	1	34	0.186	43971	40814	40275	2246
	2	36	0.130	37487	35457	35298	2446
	3	35	0.156	36867	35662	35280	3861
	4	36	0.142	35522	33555	33098	2635
	5	34	0.142	36232	34596	33848	2150

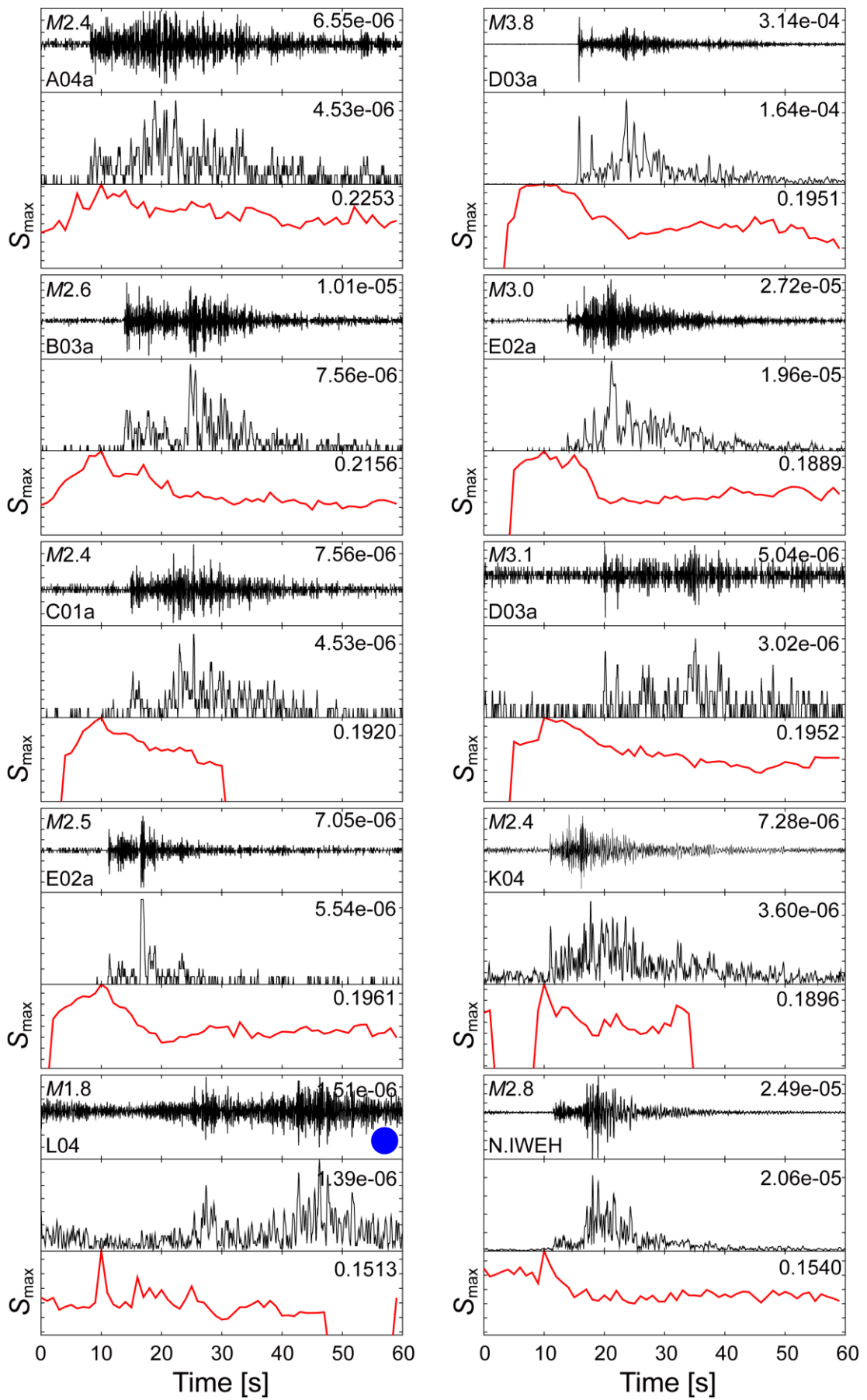
Table 4.2. The matching rates for the events in Step 1 of this study to those listed in the reference catalogs in (a) Regions 1, 3, and 5, and (b) Regions 2 and 4; repeating earthquakes in Uchida and Matsuzawa [2013] (RE), the F-net events ($VR \geq 80\%$, $N_{sta} \geq 3$) (Fnet), and events with known focal mechanisms in Nakamura *et al.* [2016] (Nkmr). Using the triangle diagrams [Frohlich, 1992], the reference events were classified into several faulting types; thrust (TF), normal (NF), strike-slip (SF), and other (OF) faulting types.

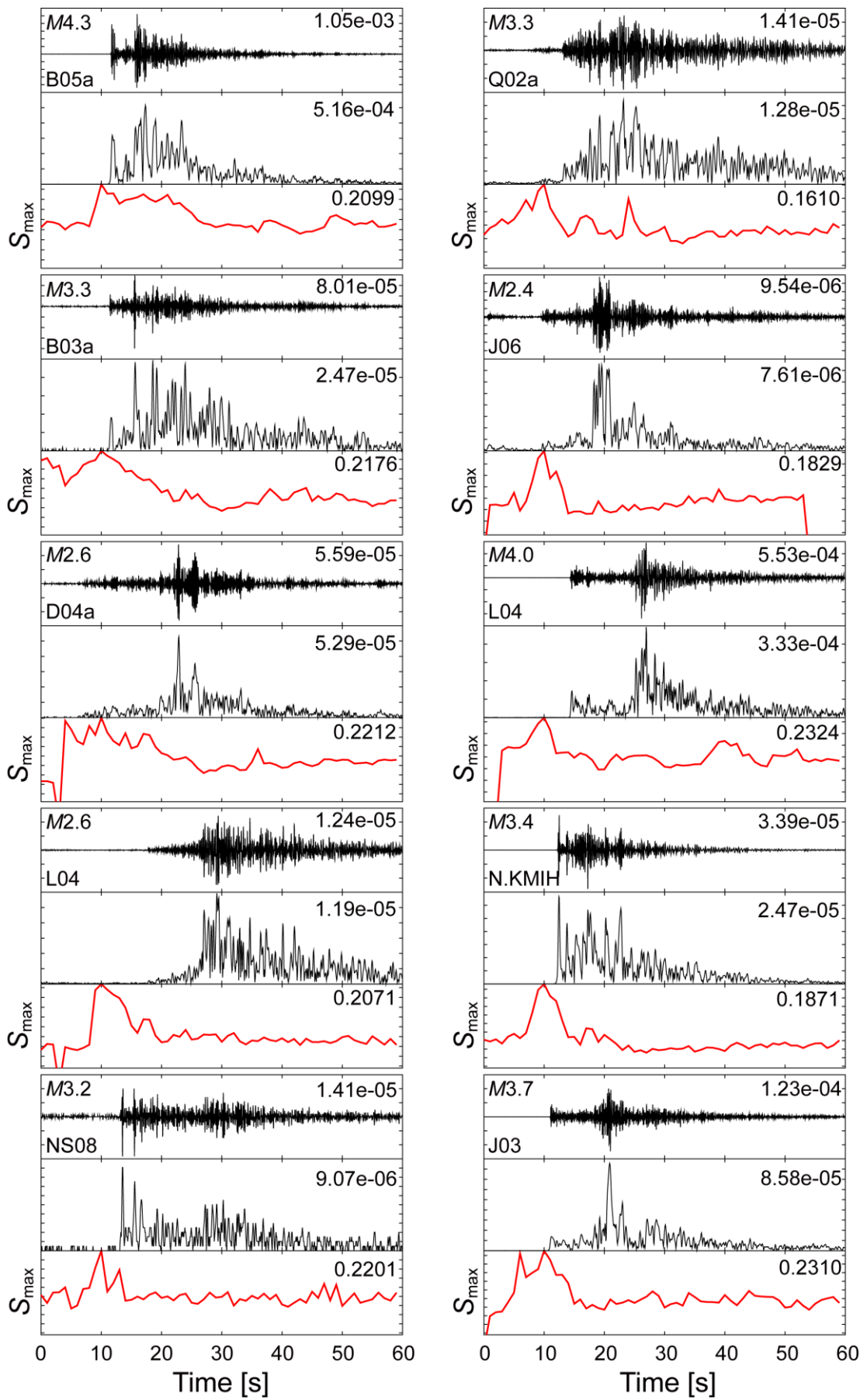
(a)	RE	Fnet TF	Fnet NF	Fnet SF	Fnet OF	Nkmr TF	Nkmr NF	Nkmr SF	Nkmr OF
Before	95% (20/21)	100% (7/7)	–	–	100% (2/2)	83% (5/6)	–	–	50% (1/2)
After 1st	92% (22/24)	98% (47/48)	86% (30/35)	100% (6/6)	90% (52/58)	76% (42/55)	82% (9/11)	100% (4/4)	96% (22/23)
After 2nd	96% (23/24)	92% (58/63)	78% (29/37)	71% (5/7)	80% (36/45)	81% (82/101)	71% (15/21)	67% (2/3)	82% (53/65)

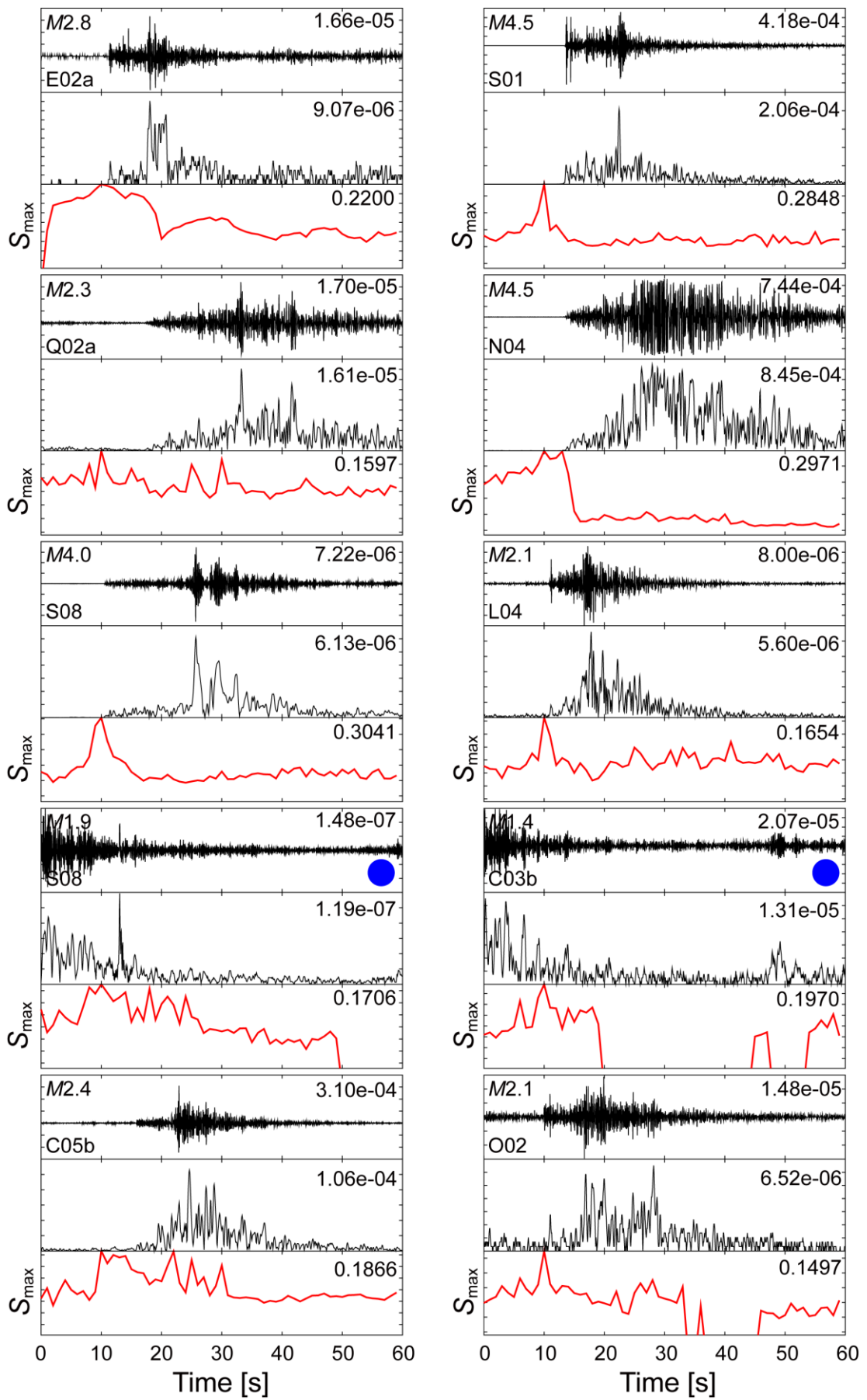
(b)	RE	Fnet TF	Fnet NF	Fnet SF	Fnet OF	Nkmr TF	Nkmr NF	Nkmr SF	Nkmr OF
Before	100% (8/8)	100% (4/4)	–	–	100% (1/1)	50% (1/2)	–	–	–
After 1st	93% (13/14)	80% (37/46)	85% (28/33)	33% (2/6)	94% (49/52)	73% (49/67)	100% (12/12)	100% (4/4)	90% (28/31)
After 2nd	100% (13/13)	100% (37/37)	92% (22/24)	50% (2/4)	97% (31/32)	92% (57/62)	100% (16/16)	100% (2/2)	97% (61/63)

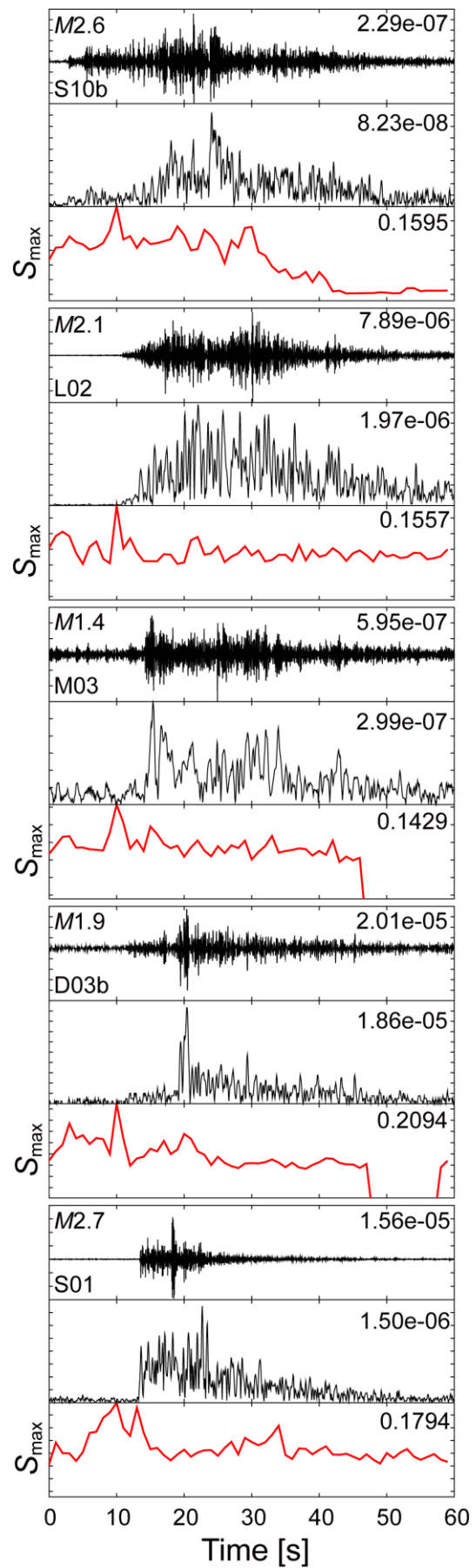
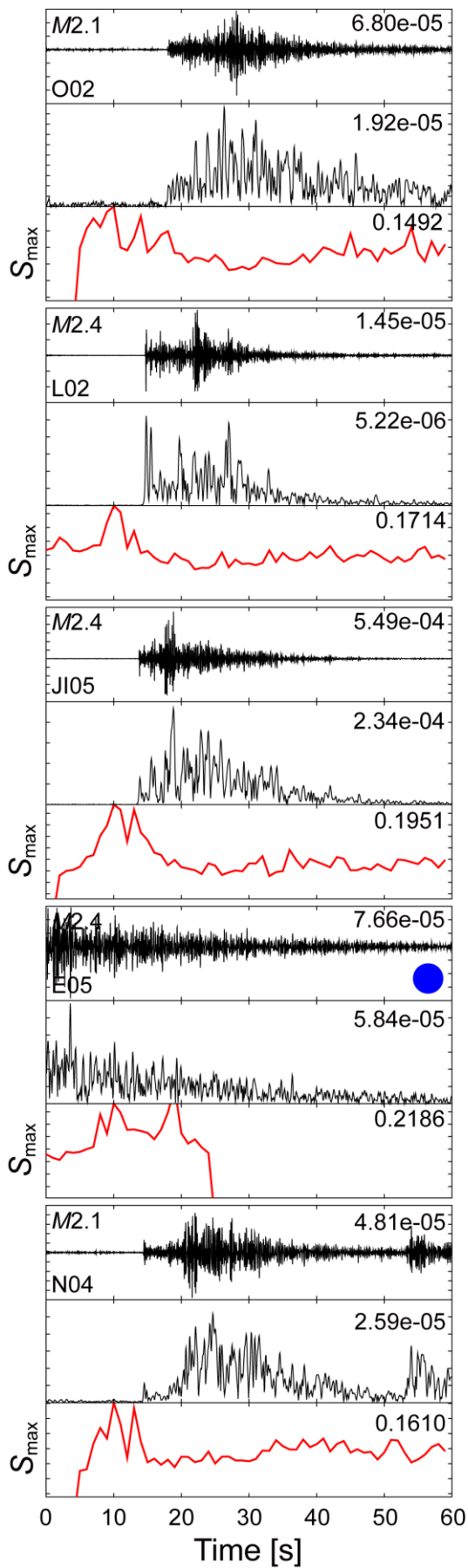
Table 4.3. Differences in epicentral locations between the catalog of this study and that of Shinohara *et al.* [2011, 2012]. The reference events are selected within a band of 10 km on both sides of the plate interface.

	After 1st		After 2nd	
	Number of Events	Mean Distance [km]	Number of Events	Mean Distance [km]
Region 1, 3, 5	84	20.4	220	14.5
Region 2, 4	78	15.5	169	15.2









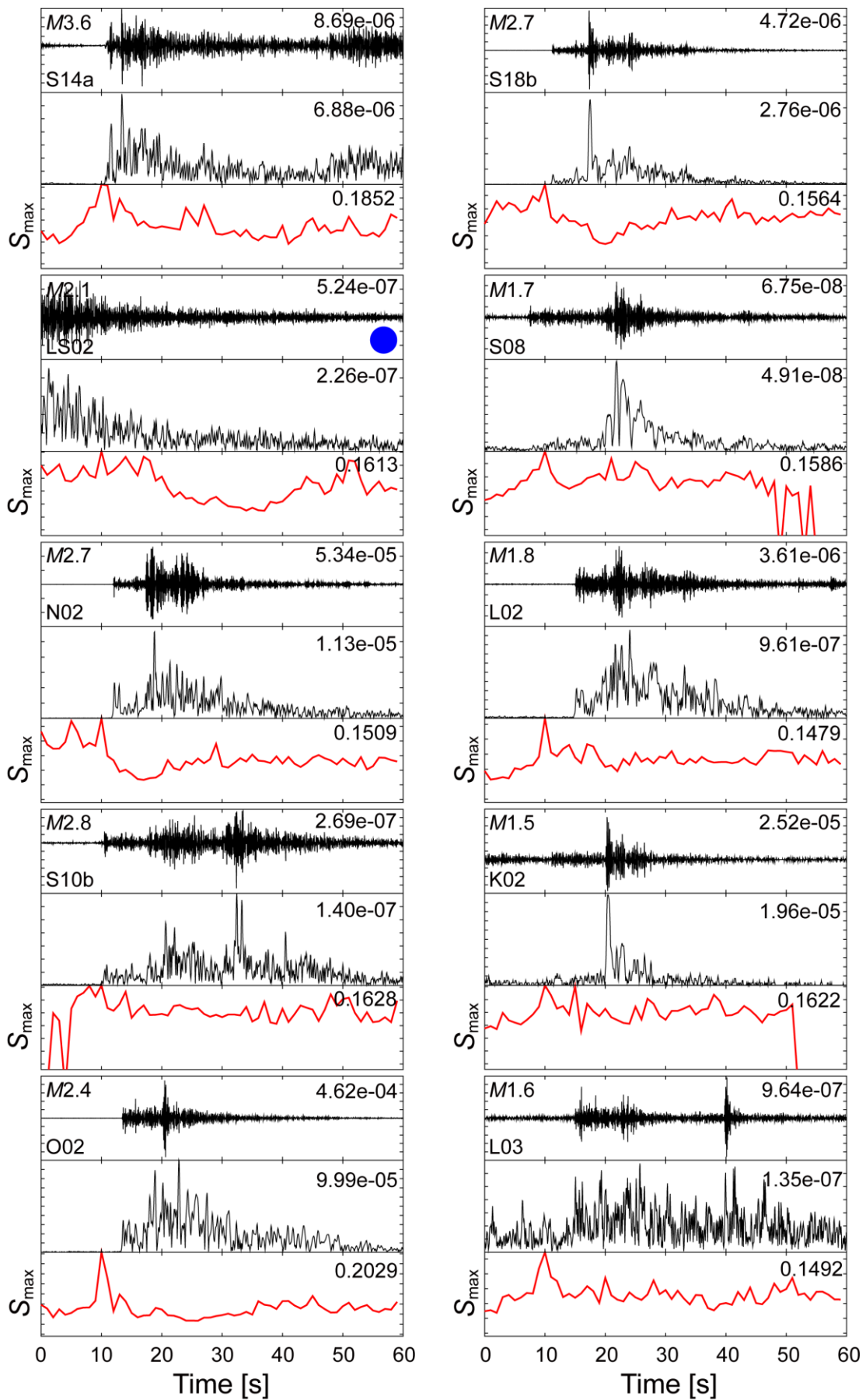


Figure 4.1. Randomly selected 50 events from the final earthquake catalog of this study. The 2–15 Hz bandpass filtered vertical-component waveform at the reference station of the array (top), the 1–5 Hz bandpass filtered envelope waveform at the same station (middle), and time series of the maximum semblance value (S_{\max}) (bottom). The absolute maximum amplitude in meters per second and the maximum S_{\max} are shown in the upper right corner of each time series. The magnitude and the name of the station are in the upper and lower left corners of each time series, respectively. A blue circle denotes a mis-detected event.

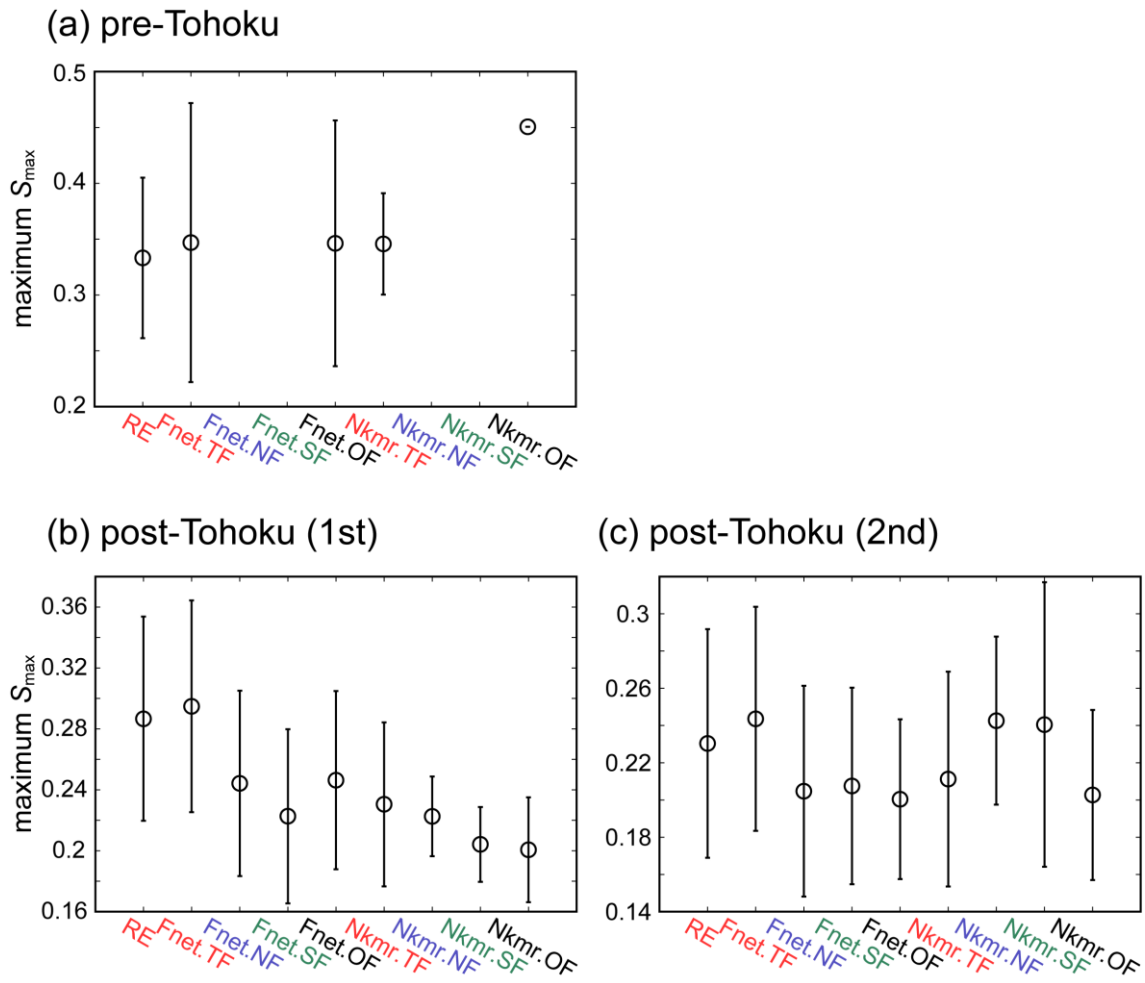


Figure 4.2. The mean values of the maximum S_{\max} for each focal mechanism in Regions 1, 3, and 5 in the matching experiments between the catalog in Step 1 of this study and the reference catalogs. The standard deviations of the values are shown as bars. Other notations are the same as in Table 4.2. Each panel shows the results for (a) the pre-Tohoku period, (b) the first, and (c) the second sub-periods of aftershock observation.

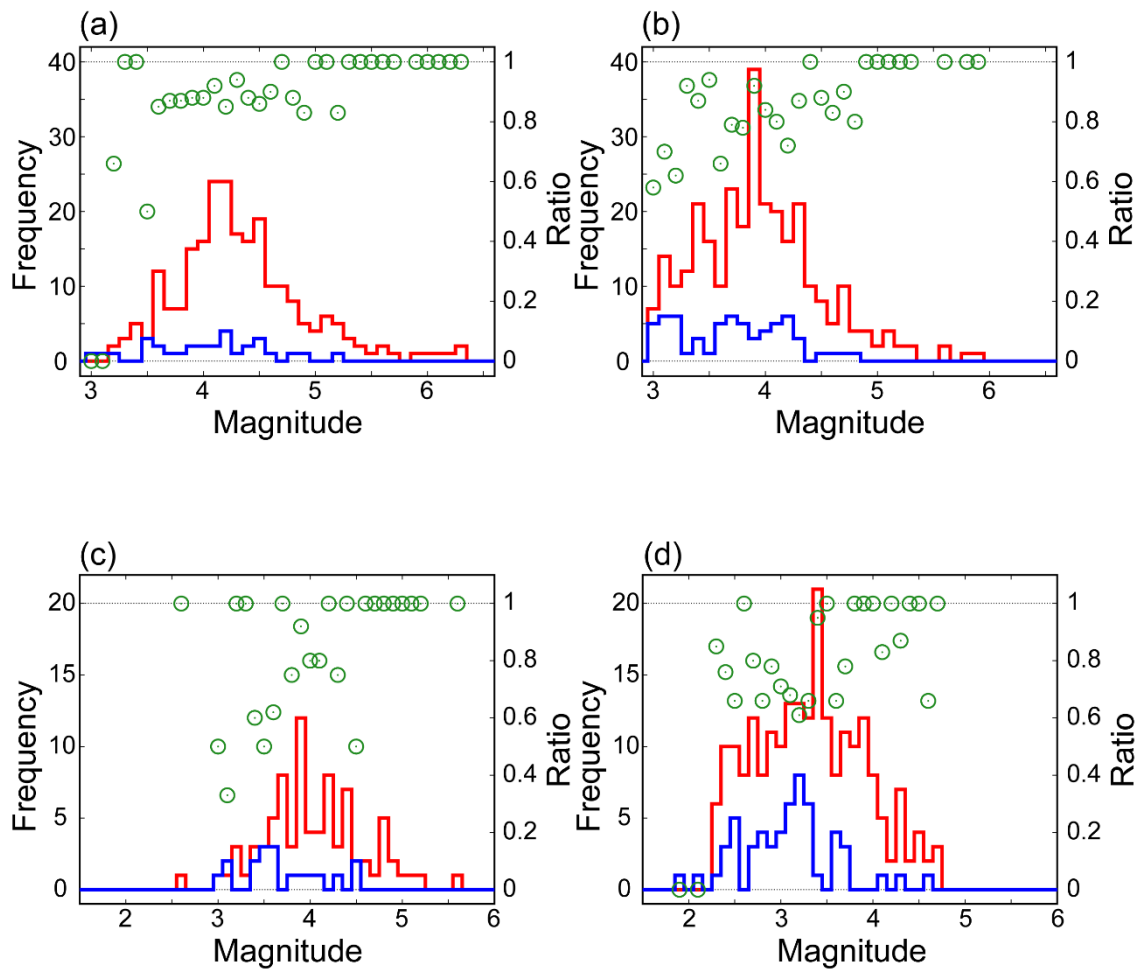


Figure 4.3. Frequency-magnitude distributions of the earthquakes obtained by the matching analyses using the same catalogs in Figure 4.2 for (a) the first and (b) the second sub-periods of aftershock observation. The same as in panels (a) and (b) using the catalog of Shinohara *et al.* [2011, 2012] of earthquakes within a band of 10 km on both sides of the plate interface for (c) the first and (d) the second sub-periods after the Tohoku earthquake. The red and blue histograms show the results of the matched and missed events, respectively. The green circles show the ratio of the number of matched events to the total number of events.

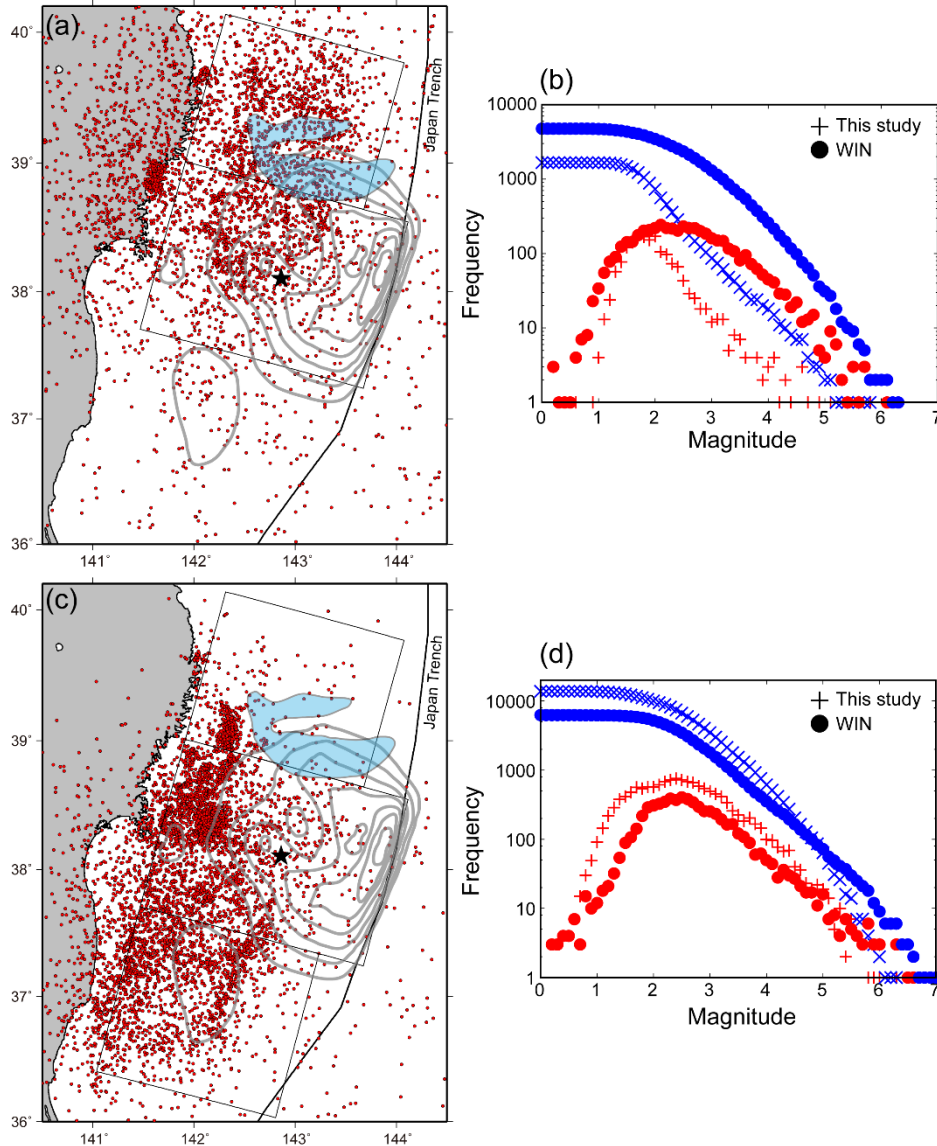


Figure 4.4. The result of the seismicity derived from the WIN auto-picking system for (a) the pre- and (c) post-Tohoku periods. Gray contours show the coseismic slip distribution of the 2011 Tohoku earthquake (outermost contour, 10 m; interval, 10 m) [Inuma *et al.*, 2012]. The star indicates its epicenter. The blue area denotes aseismic region described in Mochizuki *et al.* [2005]. Frequency-magnitude distributions for (b) the pre- and (d) post-Tohoku periods are shown in right panels. Red and blue closed circles show the non-cumulative and the cumulative distributions of the catalog derived from the WIN auto-picking, respectively, and those of this study are shown as red and blue crosses.

本図については、5年以内に雑誌等で刊行予定のため、非公開。

本図については、5年以内に雑誌等で刊行予定のため、非公開。

本図については、5年以内に雑誌等で刊行予定のため、非公開。

本図については、5年以内に雑誌等で刊行予定のため、非公開。

本図については、5年以内に雑誌等で刊行予定のため、非公開。

本図については、5年以内に雑誌等で刊行予定のため、非公開。

本図については、5年以内に雑誌等で刊行予定のため、非公開。

5. Frequency-Magnitude Relation of Seismicity

5.1 Review of Previous Studies

One of the important characteristics of seismicity is the frequency-magnitude relation of earthquakes. In general, it is well known that small earthquakes occur more frequently than large ones. Gutenberg and Richter [1944] found the power-law relationship, the Gutenberg-Richter (G-R) law, between frequency of earthquakes and their magnitudes as the following formula:

$$\log_{10} n(M) = a - bM, \quad (8)$$

where $n(M)dM$ is the frequency of earthquakes with magnitudes between M and $M + dM$, and a and b are constants. If all the earthquakes with magnitudes greater than or equal to M are obtained and listed in the catalog, the cumulative number of earthquakes with magnitudes greater than or equal to M is:

$$N(M) = \int_M^{\infty} n(M)dM. \quad (9)$$

Therefore, the original G-R equation can be also expressed as:

$$\log_{10} N(M) = A - bM, \quad (10)$$

where $A = a - \log_{10}(b \ln 10)$.

It is considered that the G-R law holds for a wide range of magnitudes from large earthquakes around the world to acoustic emissions [e.g., Nishikawa and Ide, 2014; Naoi *et al.*, 2014]. It means that the $\log_{10} N(M)$ - M plot lies on a straight line in general. However, there are some cases where the frequency-magnitude distribution (FMD) of earthquakes deviates from a straight line, such as the concave type, the convex type, and the polygonal-line type. For instance, the concave type has been observed even for the

complete earthquake catalog [e.g., Umino and Sacks, 1993], although the cause of the deviation from the G-R law is often due to the miss-detection of small earthquakes [e.g., Wiemer and Wyss, 2000]. In order to model the FMDs which does not obey the G-R law, many alternative equations have been proposed, including the truncated G-R equation [e.g., Utsu, 1972], the modified G-R equation [e.g., Utsu, 1978; Mabuchi *et al.*, 2003], and the two-range G-R equation [e.g., Gutenberg, 1956; Pacheco and Sykes, 1992]. In other approach, Kagan [1993, 1997] used the distribution of seismic moment based on a gamma distribution. Such representation of the FMDs as described above are well reviewed and compared with each other in Utsu [1999].

The physical meanings of the original G-R law have yet to be elucidated, but several theories have been proposed. One idea is the fractal nature of earthquakes which can be derived from the power-law relationship between the fault length and the number of earthquakes by assuming the G-R law [e.g., Aki, 1981]. Another is the branching model (based on the percolation model) for crack propagation which assumes that the seismic rupture starts from an individual crack, propagates, and terminates with a certain probability [e.g., Vere-Jones, 1976].

< *Introduction of the b -value* >

Under the assumption of the G-R law, the constant b in the formula (10) and (12) is called the b -value and an important parameter to characterize the FMD. The b -value itself is the relative number of small to large earthquakes. At the same time, the b -value has been widely studied how it links to other geophysical information in laboratory experiments, numerical simulations, and natural earthquakes.

Mogi [1962] showed that the spatial variation of the b -value associates with the degree of the material heterogeneities by experimental studies. Scholz [1968] conducted

rock fracture experiments and found that the b -value negatively correlates with the differential stress. Such relationship between the b -value and the differential stress was also suggested by Schorlemmer *et al.* [2005], which estimated the b -values with respect to each faulting type (normal, strike-slip, and thrust events) using the earthquake catalog for California. In contrast, Kagan [1991b] argued that the b -value would be universal in space and time if accurate magnitude determination, sufficient number of earthquakes, and homogeneous sampling of earthquakes are achieved, and that variations of the b -value are merely artifacts. Nonetheless, the spatial changes in the b -value have been also confirmed statistically significant in and around the rupture area of the past large earthquakes [e.g., Wiemer and Wyss, 1997], while its temporal changes have still not been systematically investigated though there are a few studies which reported the decrease of the b -value just before the occurrence of large earthquakes [e.g., Wyss, 1990; Nanjo *et al.*, 2012].

As the final introduction of the b -value studies, I describe previous results associated with the 2011 Tohoku earthquake. Nanjo *et al.* [2012] investigated both spatial and temporal changes in the b -values in the large coseismic slip zone of the 2011 Tohoku earthquake for the last two decades using the JMA catalog. They suggested the decrease in the b -value over the ten years before the occurrence of the Tohoku earthquake. Tormann *et al.* [2015] also estimated spatiotemporal variations of the b -values along the subducting plate using the FMDs of the JMA catalog. As the results, they indicated that the b -values in the source region of the Tohoku earthquake rapidly increased immediately after its occurrence, and recovered again within a few years.

5.2 Frequency-Magnitude Distribution and the b -value

< *Determination of the b -value and Catalog Completeness* >

The b -value of the G-R law is usually determined by using the maximum likelihood estimation (MLE). If the minimum magnitude M_c , above which the earthquake catalog is complete, is known, the b -value is calculated as follows [Aki, 1965]:

$$b = \frac{\log_{10} e}{\sum_{i=1}^N M_i / N - M_c}, \quad (11)$$

where N is the number of earthquakes to use, and M_i is the magnitude of the i th earthquake. Note that this equation is formulated under two assumptions. One is to consider that the target FMD follows the original G-R law. The other assumption is that all the earthquakes with magnitudes greater than M_c are included in the catalog. As I introduced in the previous section, there are circumstances when the FMD does not follow the original G-R law. In addition, the result of the b -value largely depends on the determination of M_c . Therefore, the method to determine M_c and the types of the FMD should be carefully considered.

In this study, I first assumed the original G-R law as the previous studies did, and compared the results with those of the previous ones. In order to estimate M_c and the b -value simultaneously, I employed the maximum curvature method [Wiemer and Wyss, 2000] which maximizes a fitting function between the observed and theoretical FMDs assuming the original G-R law. The fitting function $R(A, b, M_i)$ is defined as follows:

$$R(A, b, M_i) = 100 - \left(\frac{\sum_{M_i}^{M_{max}} |B_i - S_i|}{\sum_{M_i}^{M_{max}} B_i} \times 100 \right), \quad (12)$$

where A and b are the same as in equation (12), and B_i and S_i are the observed and theoretical cumulative number of earthquakes, respectively. First, I calculated the b -values using the MLE under the assumption of the original G-R law in $M \geq M_c$. At

this time, I adopted distance exponential weight (DEW) sampling to counting B_i in 0.1 magnitude bin width. This approach was proposed by Tormann *et al.* [2014] in which each earthquake is weighted as a function of distance r from the given grid point, and its weight $w(r)$ is: $w(r) = 0.7e^{-0.07r}$. Through the introduction of the DEW algorithm, the smoothing effect among neighboring grid points on the spatial distribution of the b -values, as Kamer and Hiemer [2015] indicated, can be reduced because this algorithm focuses on only the events near the grid points. Then, I calculated $R(A, b, M_i)$ and repeatedly performed such operations at each grid point with changing M_i . Finally, I selected $M_i + 0.2$ as M_c when R is maximized [Woessner and Wiemer, 2005]. I sampled earthquakes within 75 km radius around each grid point (here 20 km x 20 km) for the determination of M_c and the b -value with the requirements that the number of sampling events above M_c is 50 or more and the maximum value of R is 80% or more. The sampling range of 75 km is sufficiently larger than the error of epicenters (~20 km). I also confirmed that the results were robust to the choice of the sampling radius and the spacing of grid points. Here, the standard deviation of the b -value is derived by Shi and Bolt [1982] as follows:

$$\sigma(b) = 2.30b^2\sigma(\bar{M}), \quad (13)$$

where

$$\sigma^2(\bar{M}) = \frac{\sum_{i=1}^N (M_i - \bar{M})^2}{N(N-1)}. \quad (14)$$

In equation (15), \bar{M} is the mean magnitude among the earthquakes used to calculate.

< Results >

本節については、5年以内に雑誌等で刊行予定のため、非公開。

本節については、5年以内に雑誌等で刊行予定のため、非公開。

本節については、5年以内に雑誌等で刊行予定のため、非公開。

5.3 Statistical Evaluation of Frequency-Magnitude Distribution

本節については、5年以内に雑誌等で刊行予定のため、非公開。

本節については、5年以内に雑誌等で刊行予定のため、非公開。

本節については、5年以内に雑誌等で刊行予定のため、非公開。

本節については、5年以内に雑誌等で刊行予定のため、非公開。

本図については、5年以内に雑誌等で刊行予定のため、非公開。

6. General Discussion

6.1 Spatiotemporal Variation of Frequency-Magnitude Distribution

本節については、5年以内に雑誌等で刊行予定のため、非公開。

本節については、5年以内に雑誌等で刊行予定のため、非公開。

本節については、5年以内に雑誌等で刊行予定のため、非公開。

6.2 Future Studies

< Constraints on Focal Depths >

In this study, I originally developed the automated detection and location method and applied it to *P*-wave arrivals of local earthquakes. This method is also applicable in principle to *S*-wave arrivals of the earthquakes if tables of *S*-wave traveltimes are prepared. However, waveform coherence of *S* waves among stations is generally low because waveforms of *S*-wave arrivals of local earthquakes are often contaminated by *P*-coda waves. Furthermore, low waveform coherence among stations can be observed even on *P* waves as I explained in Section 4.2 although the proportion is low in comparison to that of *S* waves. Therefore, as I introduced in Section 3.1, automated methods using characteristic functions, instead of the original waveforms, are alternative approaches in order to reduce misdetection of earthquakes and locate hypocenters with better accuracy, especially in depth.

本節については、5年以内に雑誌等で刊行予定のため、非公開。

本節については、5年以内に雑誌等で刊行予定のため、非公開。

< Application to Other Networks >

As I described in Chapter 1, developments of seafloor observation instruments have been achieved over the past decades. Recently, a new earthquake and tsunami monitoring system, S-net (seafloor observation network for earthquakes and tsunamis along the Japan Trench), has been developed over the entire Japan Trench subduction zone at station intervals of about 30 km. S-net is operated by NIED and each station consists of seismometers and tsunami meters. One of the advantages of S-net is that this is not temporary, but a real-time permanent network. When S-net data is available, automated detection and location methods which can also incorporate OBS data is

essential. Therefore, the method developed in this study would be more useful for future studies of real-time hypocenter analysis with continuous seismic data.

本図については、5年以内に雑誌等で刊行予定のため、非公開。

本図については、5年以内に雑誌等で刊行予定のため、非公開。

本図については、5年以内に雑誌等で刊行予定のため、非公開。

7. Conclusions

In this study, I developed an automated method for detection and location of local earthquakes including small ones. The method consists of the STA/LTA trigger algorithm and the array-based waveform stacking which illuminates seismic sources of energy release. I applied the method to onshore (34 stations in total) and offshore seismic data (more than 160 stations in total) in the Japan Trench subduction zone before and after the 2011 Tohoku earthquake. The method of this study provides higher detection rate, compared with the conventional automatic phase picking and location method.

As a result of hypocenter determination of earthquakes around the plate interface, I obtained a more complete earthquake catalog even immediately after the Tohoku earthquake. The resulting number of earthquakes for the post-Tohoku period is about 1.8 times as many as that in the JMA catalog within a band of 5 km on both sides of the plate interface. The magnitudes of completeness for the pre- and post-Tohoku periods are approximately 2 and 3, respectively, as being derived when a fitting function between the observed and theoretical cumulative FMDs assuming the G-R law is maximized.

Seismicity results from October 2007 to June 2008 show a probable gap in the seismicity along 39°N. The observed low seismicity area around 39°N is coincident with the aseismic area where weak interplate coupling has been suggested by previous studies. The relatively active seismic area is adjacent to the aseismic area, corresponding to the down-dip side of the coseismic slip zone of the Tohoku earthquake. For the first three months after the occurrence of the Tohoku earthquake, the typical low

seismicity areas are located in the coseismic slip zone. Negative correlation between the cumulative seismic moment release and the amount of coseismic slip is also revealed for the same period. In contrast, several aftershock clusters are observed along the down-dip edge of the coseismic rupture region and near the trench axis. These results provide another constraint on the coseismic slip zone expected from seismicity and indicate the stress increase in its surrounding area.

In order to further understand the characteristics of seismicity, I investigated the frequency-magnitude distribution of earthquakes. In comparison with the previous study using the JMA catalog data, low b -value areas corresponding to low M_c are widely observed immediately after the Tohoku earthquake. The additional statistical analysis, under the assumption that the FMD is described by the G-R law and the detection rate depending on the magnitudes, indicates that the observed FMDs in these areas do not follow the G-R law in the range of large magnitudes ($M > 4$). Such breakdown of the G-R law for aftershocks of the 2011 Tohoku earthquake is first revealed. That deviation from the G-R law provides the difference in the b -value distribution between the catalog data of this study and that of the previous study.

In terms of spatiotemporal variations of the observed FMDs before and after the Tohoku earthquake, I revealed the regionalities of the FMDs which can be explained by heterogeneities of the stress field and frictional properties along the plate interface. Because these factors that influence on seismicity patterns may have changed during the Tohoku earthquake, this study contributes to providing constraints on relationship between the FMDs and the source region and its rupture process of the 2011 Tohoku earthquake.

Acknowledgments

First of all, I would like to express my deepest appreciation to Associate Professor Kimihiro Mochizuki for his generous support and encouragement during my PhD course. His helpful suggestions and insightful comments would have been absolutely necessary for my research. Through the fruitful discussions with him, I have learnt not only how to do research but also attitudes towards science.

I would like to offer my thanks to my defense committee members: Professors Takaya Iwasaki and Satoshi Ide and Associate Professors Masao Nakatani, Hiroshi Tsuruoka, and Ryosuke Ando. I am very grateful to Professors Masanao Shinohara and Ryota Hino and Dr. Shuichi Kodaira for constructive discussions that made valuable contributions to this thesis. My gratitude also goes to Professors Hajime Shiobara and Toshinori Sato, Associate Professors Yoshihiro Ito and Yoshio Murai, Assistant Professors Tomoaki Yamada and Hiroshi Yakiwara, and Drs. Kenji Uehira and Hiroaki Tsushima for giving me advice and encouragement and for collecting OBS data. The OBS observations were supported by the Ministry of Education, Culture, Sports, Science and Technology (MEXT) of Japan.

I would like to appreciate all the great discussions with Assistant Professor Takeshi Akuhara. I would also like to thank Professors Kazushige Obara and Naoshi Hirata, Associate Professors Shin'ichi Sakai, Takashi Iidaka, and Aitaro Kato, Assistant Professors Takuto Maeda and Akiko Takeo, and Dr. Koichiro Obana for their helpful advice and comments that improved this thesis. I have received generous encouragement from Associate Professor Yusaku Ohta, Assistant Professors Ryosuke Azuma, Yusuke Yamashita, and Naofumi Aso, Drs. Gou Fujie, Yojiro Yamamoto,

Takahiko Uchide, Shunsuke Takemura, Yuya Machida, Takashi Shinbo, and Kenji Hirata, and Messrs. Takeo Yagi, Hideji Abe, and Shuichi Suzuki. I also thank many colleagues in the University of Tokyo during my graduate studies: Messrs. Shinji Yoneshima, Daisuke Haijima, and Ken Ishihara, Ms. Yuriko Iwasaki, and Dr. Suguru Yabe.

Special thanks go to Professor Hitoshi Kawakatsu for giving me an opportunity to stay in the Institut de Physique du Globe de Paris. I would like to be deeply grateful to Drs. Jean-Pierre Vilotte, Pascal Bernard, Claudio Satriano, and Natalia Poiata, and Mr. Florent Aden-Antoniow for their supports and discussions during the internship, and for providing the codes of detection and location method using kurtosis functions.

I acknowledge JMA, NIED Hi-net, and NIED F-net for allowing me to use an earthquake catalog, continuous waveform data, and focal mechanism data, respectively. I appreciate Associate Professor Hiroshi Tsuruoka giving me the code of Ogata and Katsura [1993]. Earthquake catalogs given by Associate Professor Naoki Uchida and Mr. Wataru Nakamura have been a great help in this work. I also thank Associate Professor Kazuo Nakahigashi for giving me a depth model of the Pacific plate compiled by marine seismic observations. The figures in this thesis were obtained using gnuplot [<http://www.gnuplot.info/>], Generic Mapping Tools [Wessel and Smith, 1991], SeisGram2K [<http://alomax.free.fr/seisgram/SeisGram2K.html>], Matplotlib [Hunter, 2007], and Adobe Illustrator. This work was supported by JSPS KAKENHI Grant Number 15J11270.

Finally, my family and friends supported me every time, I thank them very much.

References

- Aki, K. (1965), Maximum Likelihood Estimate of b in the Formula $\log N = a - bM$ and its Confidence Limits, *Bull. Earthq. Res. Inst.*, *43*(2), 237–239.
- Aki, K. (1981), A Probabilistic Synthesis of Precursory Phenomena, in *Earthquake Prediction: An International Review*, edited by D. W. Simpson and P. G. Richards, pp. 566–574, American Geophysical Union, Washington, D.C.
- Allen, R. V. (1978), Automatic earthquake recognition and timing from single traces, *Bull. Seismol. Soc. Am.*, *68*(5), 1521–1532.
- Asano, Y. and T. Iwata (2012), Source model for strong ground motion generation in the frequency range 0.1–10 Hz during the 2011 Tohoku earthquake, *Earth, Planets Sp.*, *64*(6), 1111–1123, doi: 10.5047/eps.2012.05.003.
- Asano, Y., T. Saito, Y. Ito, K. Shiomi, H. Hirose, T. Matsumoto, S. Aoi, S. Hori, and S. Sekiguchi (2011), Spatial distribution and focal mechanisms of aftershocks of the 2011 off the Pacific coast of Tohoku Earthquake, *Earth, Planets Sp.*, *63*(7), 669–673, doi:10.5047/eps.2011.06.016.
- Baillard, C., W. C. Crawford, V. Ballu, C. Hibert, and A. Mangeny (2014), An Automatic Kurtosis-Based P- and S-Phase Picker Designed for Local Seismic Networks, *Bull. Seismol. Soc. Am.*, *104*(1), 394–409, doi:10.1785/0120120347.
- Das, S., and C. Henry (2003), Spatial relation between main earthquake slip and its aftershock distribution, *Rev. Geophys.*, *41*(3), 1013, doi:10.1029/2002RG000119.
- DeMets, C., R. G. Gordon, D. F. Argus, and S. Stein (1994), Effect of recent revisions to the geomagnetic reversal time scale on estimates of current plate motions, *Geophys. Res. Lett.*, *21*(20), 2191–2194, doi:10.1029/94GL02118.

- Frohlich, C. (1992), Triangle diagrams: ternary graphs to display similarity and diversity of earthquake focal mechanisms, *Phys. Earth Planet. Inter.*, 75(1–3), 193–198, doi:10.1016/0031-9201(92)90130-N.
- Fujie, G., J. Kasahara, R. Hino, T. Sato, M. Shinohara, and K. Suyehiro (2002), A significant relation between seismic activities and reflection intensities in the Japan Trench region, *Geophys. Res. Lett.*, 29(7), 1100, doi:10.1029/2001GL013764.
- Fujiwara, T., S. Kodaira, T. No, Y. Kaiho, N. Takahashi, and Y. Kaneda (2011), The 2011 Tohoku-Oki Earthquake: Displacement Reaching the Trench Axis, *Science*, 334(6060), 1240, doi:10.1126/science.1211554.
- Funasaki, J., and Earthquake Prediction Information Division (2004), Revision of the JMA Velocity Magnitude, *Q. J. Seismol.*, 67(1–4), 11–20 (in Japanese with English abstract).
- Geiger, L. (1910), Herdbestimmung bei Erdbeben aus den Ankunftszeiten, *Nachrichten von der Gesellschaft der Wissenschaften zu Göttingen, Math. Klasse*, 1910(4), 331–349 (in German).
- Geiger, L. (1912), Probability method for the determination of earthquake epicenters from the arrival time only, *Bull. St. Louis Univ.*, 8(1), 60–71.
- Grigoli, F., S. Cesca, M. Vassallo, and T. Dahm (2013), Automated Seismic Event Location by Travel-Time Stacking: An Application to Mining Induced Seismicity, *Seismol. Res. Lett.*, 84(4), 666–677, doi:10.1785/0220120191.
- Gutenberg, B. (1956), The energy of earthquakes, *Quarterly J. Geological Soc.*, 112(1–4), 1–14, doi: 10.1144/GSL.JGS.1956.112.01-04.02
- Gutenberg, B., and C. F. Richter (1944), Frequency of earthquakes in California, *Bull. Seismol. Soc. Am.*, 34(4), 185–188.
- Haijima, D. (2015), Seismic Activity and Velocity Structure in the Northern Hikurangi

- Subduction Zone offshore the North Island of New Zealand, *Master's Thesis*, 67 pp., the Univ. of Tokyo, Japan.
- Hasegawa, A., K. Yoshida, and T. Okada (2011), Nearly complete stress drop in the 2011 Mw 9.0 off the Pacific coast of Tohoku Earthquake, *Earth, Planets Sp.*, 63(7), 703–707, doi:10.5047/eps.2011.06.007.
- Hino, R., Y. Yamamoto, A. Kuwano, M. Nishino, T. Kanazawa, T. Yamada, K. Nakahigashi, K. Mochizuki, M. Shinohara, K. Minato, G. Aoki, N. Okawara, M. Tanaka, M. Abe, E. Araki, S. Kodaira, G. Fujie, and Y. Kaneda (2006), Hypocenter distribution of the main- and aftershocks of the 2005 Off Miyagi Prefecture earthquake located by ocean bottom seismographic data, *Earth, Planets Sp.*, 58(12), 1543–1548, doi:10.1186/BF03352658.
- Hirata, N., and M. Matsu'ura (1987), Maximum-likelihood estimation of hypocenter with origin time eliminated using nonlinear inversion technique, *Phys. Earth Planet. Inter.*, 47, 50–61, doi:10.1016/0031-9201(87)90066-5.
- Hunter, J. D. (2007), Matplotlib: A 2D Graphics Environment, *Comput. Sci. Eng.*, 9(3), 90–95, doi:10.1109/MCSE.2007.55.
- Ide, S. (2010), Striations, duration, migration and tidal response in deep tremor, *Nature*, 466(7304), 356–359, doi:10.1038/nature09251.
- Ide, S., A. Baltay, and G. C. Beroza (2011), Shallow Dynamic Overshoot and Energetic Deep Rupture in the 2011 Mw 9.0 Tohoku-Oki Earthquake, *Science*, 332(6036), 1426–1429, doi:10.1126/science.1207020.
- Igarashi, T., T. Matsuzawa, N. Umino, and A. Hasegawa (2001), Spatial distribution of focal mechanisms for interplate and intraplate earthquakes associated with the subducting Pacific plate beneath the northeastern Japan arc: A triple-planed deep seismic zone, *J. Geophys. Res.*, 106(B2), 2177–2191, doi:10.1029/2000JB900386.

- Iinuma, T., R. Hino, M. Kido, D. Inazu, Y. Osada, Y. Ito, M. Ohzono, H. Tsushima, S. Suzuki, H. Fujimoto, and S. Miura (2012), Coseismic slip distribution of the 2011 off the Pacific Coast of Tohoku Earthquake (M9.0) refined by means of seafloor geodetic data, *J. Geophys. Res.*, *117*(B7), B07409, doi:10.1029/2012JB009186.
- Kagan, Y. Y. (1991a), 3-D rotation of double-couple earthquake sources, *Geophys. J. Int.*, *106*(3), 709–716, doi:10.1111/j.1365-246X.1991.tb06343.x.
- Kagan, Y. Y. (1991b), Seismic moment distribution, *Geophys. J. Int.*, *106*(1), 123–134, doi:10.1111/j.1365-246X.1991.tb04606.x.
- Kagan, Y. Y. (1993), Statistics of characteristic earthquakes, *Bull. Seismol. Soc. Am.*, *83*(1), 7–24.
- Kagan, Y. Y. (1997), Seismic moment-frequency relation for shallow earthquakes: Regional comparison, *J. Geophys. Res.*, *102*(B2), 2835–2852, doi:10.1029/96JB03386.
- Kamer, Y., and S. Hiemer (2015), Data-driven spatial b value estimation with applications to California seismicity: To b or not to b, *J. Geophys. Res.*, *120*(7), 5191–5214, doi:10.1002/2014JB011510.
- Kanamori, H. (1977), The energy release in great earthquakes, *J. Geophys. Res.*, *82*(20), 2981–2987, doi:10.1029/JB082i020p02981.
- Kao, H., and S.-J. Shan (2004), The Source-Scanning Algorithm: mapping the distribution of seismic sources in time and space, *Geophys. J. Int.*, *157*(2), 589–594, doi:10.1111/j.1365-246X.2004.02276.x.
- Kato, A., and T. Igarashi (2012), Regional extent of the large coseismic slip zone of the 2011 Mw 9.0 Tohoku-Oki earthquake delineated by on-fault aftershocks, *Geophys. Res. Lett.*, *39*(15), L15301, doi:10.1029/2012GL052220.
- Katsumata, A. (2001), Magnitude determination of deep-focus earthquakes in and

- around Japan with regional velocity-amplitude data, *Earth, Planets Sp.*, 53(5), 333–346, doi:10.1186/BF03352390.
- Katsumata, A. (2007), Magnitude Determination of Deep-focus Earthquakes in and around Japan with Regional Velocity-amplitude Data (II), *Pap. Meteorol. Geophys.*, 58, 31–61, doi:10.2467/mripapers.58.31.
- Koketsu, K., H. Miyake, H. Fujiwara, and T. Hashimoto (2008), Progress towards a Japan Integrated Velocity Structure Model and Long-Period Ground Motion Hazard Map, in *Proceedings of the 14th World Conference on Earthquake Engineering*, Beijing, China.
- Koketsu, K., H. Miyake, and H. Suzuki (2012), Japan Integrated Velocity Structure Model Version 1, in *Proceedings of the 15th World Conference on Earthquake Engineering*, Lisbon, Portugal.
- de Kool, M., N. Rawlinson, and M. Sambridge (2006), A practical grid-based method for tracking multiple refraction and reflection phases in three-dimensional heterogeneous media, *Geophys. J. Int.*, 167(1), 253–270, doi:10.1111/j.1365-246X.2006.03078.x.
- Liao, Y.-C., H. Kao, A. Rosenberger, S.-K. Hsu, and B.-S. Huang (2012), Delineating complex spatiotemporal distribution of earthquake aftershocks: an improved Source-Scanning Algorithm, *Geophys. J. Int.*, 189(3), 1753–1770, doi:10.1111/j.1365-246X.2012.05457.x.
- Lomax, A., C. Satriano, and M. Vassallo (2012), Automatic Picker Developments and Optimization: FilterPicker—a Robust, Broadband Picker for Real-Time Seismic Monitoring and Earthquake Early Warning, *Seismol. Res. Lett.*, 83(3), 531–540, doi:10.1785/gssrl.83.3.531.
- Mabuchi, H., M. Ohtake, and H. Sato (2003), Possibility of Estimating the Maximum

- Earthquake Magnitude Based on a Modified G-R Model for Magnitude-Frequency Distribution: Spatial Distribution of Mc East off Northeast Japan, *Zisin (Journal Seismol. Soc. Japan. 2nd ser.)*, 56(3), 255–265 (in Japanese with English abstract).
- Miura, S., S. Kodaira, A. Nakanishi, T. Tsuru, N. Takahashi, N. Hirata, and Y. Kaneda (2003), Structural characteristics controlling the seismicity of southern Japan Trench fore-arc region, revealed by ocean bottom seismographic data, *Tectonophysics*, 363(1–2), 79–102, doi:10.1016/S0040-1951(02)00655-8.
- Mochizuki, K., M. Nakamura, J. Kasahara, R. Hino, M. Nishino, A. Kuwano, Y. Nakamura, T. Yamada, M. Shinohara, T. Sato, P. P. Moghaddam, and T. Kanazawa (2005), Intense PP reflection beneath the aseismic forearc slope of the Japan Trench subduction zone and its implication of aseismic slip subduction, *J. Geophys. Res.*, 110(B1), B01302, doi:10.1029/2003JB002892.
- Mogi, K. (1962), Magnitude-Frequency Relation for Elastic Shocks Accompanying Fractures of Various Materials and Some Related Problems in Earthquakes (2nd Paper), *Bull. Earthq. Res. Inst.*, 40(4), 831–853.
- Mori, J., and R. E. Abercrombie (1997), Depth dependence of earthquake frequency-magnitude distributions in California: Implications for rupture initiation, *J. Geophys. Res.*, 102(B7), 15081–15090, doi:10.1029/97JB01356.
- Nakamura, W., N. Uchida, and T. Matsuzawa (2016), Spatial distribution of the faulting types of small earthquakes around the 2011 Tohoku-oki earthquake: A comprehensive search using template events, *J. Geophys. Res.*, 121(4), 2591–2607, doi:10.1002/2015JB012584.
- Nakatani, Y., K. Mochizuki, M. Shinohara, T. Yamada, R. Hino, Y. Ito, Y. Murai, and T. Sato (2015), Changes in seismicity before and after the 2011 Tohoku earthquake around its southern limit revealed by dense ocean bottom seismic array data,

- Geophys. Res. Lett.*, 42(5), 1384–1389, doi:10.1002/2015GL063140.
- Nanjo, K. Z., N. Hirata, K. Obara, and K. Kasahara (2012), Decade-scale decrease in b value prior to the M9-class 2011 Tohoku and 2004 Sumatra quakes, *Geophys. Res. Lett.*, 39(20), L20304, doi:10.1029/2012GL052997.
- Naoi, M., M. Nakatani, S. Horiuchi, Y. Yabe, J. Philipp, T. Kgarume, G. Morema, S. Khambule, T. Masakale, L. Ribeiro, K. Miyakawa, A. Watanabe, K. Otsuki, H. Moriya, O. Murakami, H. Kawakata, N. Yoshimitsu, A. Ward, R. Durrheim, and H. Ogasawara (2014), Frequency–Magnitude Distribution of $-3.7 \leq M_w \leq 1$ Mining-Induced Earthquakes Around a Mining Front and b Value Invariance with Post-Blast Time, *Pure Appl. Geophys.*, 171(10), 2665–2684, doi:10.1007/s00024-013-0721-7.
- Neidell, N. S., and M. T. Taner (1971), SEMBLANCE AND OTHER COHERENCY MEASURES FOR MULTICHANNEL DATA, *GEOPHYSICS*, 36(3), 482–497, doi:10.1190/1.1440186.
- Nishikawa, T., and S. Ide (2014), Earthquake size distribution in subduction zones linked to slab buoyancy, *Nat. Geosci.*, 7(12), 904–908, doi:10.1038/ngeo2279.
- Nishizawa, A., T. Kanazawa, T. Iwasaki, and H. Shimamura (1992), Spatial distribution of earthquakes associated with the Pacific plate subduction off northeastern Japan revealed by ocean bottom and land observation, *Phys. Earth Planet. Inter.*, 75(1–3), 165–175, doi:10.1016/0031-9201(92)90127-H.
- Obana, K., G. Fujie, T. Takahashi, Y. Yamamoto, Y. Nakamura, S. Kodaira, N. Takahashi, Y. Kaneda, and M. Shinohara (2012), Normal-faulting earthquakes beneath the outer slope of the Japan Trench after the 2011 Tohoku earthquake: Implications for the stress regime in the incoming Pacific plate, *Geophys. Res. Lett.*, 39(7), L00G24, doi:10.1029/2011GL050399.

- Obana, K., S. Kodaira, M. Shinohara, R. Hino, K. Uehira, H. Shiobara, K. Nakahigashi, T. Yamada, H. Sugioka, A. Ito, Y. Nakamura, S. Miura, T. No, and N. Takahashi (2013), Aftershocks near the updip end of the 2011 Tohoku-Oki earthquake, *Earth Planet. Sci. Lett.*, 382, 111–116, doi:10.1016/j.epsl.2013.09.007.
- Obara, K. (2002), Nonvolcanic Deep Tremor Associated with Subduction in Southwest Japan, *Science*, 296(5573), 1679–1681, doi: 10.1126/science.1070378.
- Ogata, Y., and K. Katsura (1993), Analysis of temporal and spatial heterogeneity of magnitude frequency distribution inferred from earthquake catalogues, *Geophys. J. Int.*, 113(3), 727–738, doi: 10.1111/j.1365-246X.1993.tb04663.x.
- Okada, Y., K. Kasahara, S. Hori, K. Obara, S. Sekiguchi, H. Fujiwara, and A. Yamamoto (2004), Recent progress of seismic observation networks in Japan —Hi-net, F-net, K-NET and KiK-net—, *Earth, Planets Sp.*, 56(8), xv–xxviii, doi:10.1186/BF03353076.
- Pacheco, J. F., and L. R. Sykes (1992), Seismic moment catalog of large shallow earthquakes, 1900 to 1989, *Bull. Seismol. Soc. Am.*, 82(3), 1306–1349.
- Poiata, N., C. Satriano, J.-P. Vilotte, P. Bernard, and K. Obara (2016), Multiband array detection and location of seismic sources recorded by dense seismic networks, *Geophys. J. Int.*, 205(3), 1548–1573, doi:10.1093/gji/ggw071.
- Rawlinson, N., M. de Kool, and M. Sambridge (2006), Seismic wavefront tracking in 3D heterogeneous media: applications with multiple data classes, *Explor. Geophys.*, 37(4), 322–330, doi:10.1071/EG06322.
- Ringdal, F. (1975), On the estimation of seismic detection thresholds, *Bull. Seismol. Soc. Am.*, 65(6), 1631–1642.
- Rosenberger, A. (2010), Real-Time Ground-Motion Analysis: Distinguishing P and S Arrivals in a Noisy Environment, *Bull. Seismol. Soc. Am.*, 100(3), 1252–1262,

doi:10.1785/0120090265.

Saragiotis, C. D., L. J. Hadjileontiadis, and S. M. Panas (2002), PAI-S/K: A robust automatic seismic P phase arrival identification scheme, *IEEE Trans. Geosci. Remote Sens.*, *40*(6), 1395–1404, doi:10.1109/TGRS.2002.800438.

Satake, K., Y. Fujii, T. Harada, and Y. Namegaya (2013), Time and Space Distribution of Coseismic Slip of the 2011 Tohoku Earthquake as Inferred from Tsunami Waveform Data, *Bull. Seismol. Soc. Am.*, *103*(2B), 1473–1492, doi:10.1785/0120120122.

Sato, M., T. Ishikawa, N. Ujihara, S. Yoshida, M. Fujita, M. Mochizuki, and A. Asada (2011), Displacement Above the Hypocenter of the 2011 Tohoku-Oki Earthquake, *Science*, *332*(6036), 1395, doi:10.1126/science.1207401.

Scholz, C. H. (1968), The frequency-magnitude relation of microfracturing in rock and its relation to earthquakes, *Bull. Seismol. Soc. Am.*, *58*(1), 399–415.

Scholz, C. H. (2015), On the stress dependence of the earthquake b value, *Geophys. Res. Lett.*, *42*(5), 1399–1402, doi: 10.1002/2014GL062863.

Schorlemmer, D., S. Wiemer, and M. Wyss (2005), Variations in earthquake-size distribution across different stress regimes, *Nature*, *437*(7058), 539–542, doi:10.1038/nature04094.

Shi, Y., and B. A. Bolt (1982), The standard error of the magnitude-frequency b value, *Bull. Seismol. Soc. Am.*, *72*(5), 1677–1687.

Shinohara, M., R. Hino, T. Yoshizawa, M. Nishino, T. Sato, and K. Suyehiro (2005), Hypocenter distribution of plate boundary zone off Fukushima, Japan, derived from ocean bottom seismometer data, *Earth, Planets Sp.*, *57*(2), 93–105, doi:10.1186/BF03352553.

Shinohara, M., T. Yamada, K. Nakahigashi, S. Sakai, K. Mochizuki, K. Uehira, Y. Ito,

- R. Azuma, Y. Kaiho, T. No, H. Shiobara, R. Hino, Y. Murai, H. Yakiwara, T. Sato, Y. Machida, T. Shinbo, T. Isse, H. Miyamachi, K. Obana, N. Takahashi, S. Kodaira, Y. Kaneda, K. Hirata, S. Yoshikawa, K. Obara, T. Iwasaki, and N. Hirata (2011), Aftershock observation of the 2011 off the Pacific coast of Tohoku Earthquake by using ocean bottom seismometer network, *Earth, Planets Sp.*, 63(7), 835–840, doi:10.5047/eps.2011.05.020.
- Shinohara, M., Y. Machida, T. Yamada, K. Nakahigashi, T. Shinbo, K. Mochizuki, Y. Murai, R. Hino, Y. Ito, T. Sato, H. Shiobara, K. Uehira, H. Yakiwara, K. Obana, N. Takahashi, S. Kodaira, K. Hirata, H. Tsushima, and T. Iwasaki (2012), Precise aftershock distribution of the 2011 off the Pacific coast of Tohoku Earthquake revealed by an ocean-bottom seismometer network, *Earth, Planets Sp.*, 64(12), 1137–1148, doi:10.5047/eps.2012.09.003.
- Sun, T., K. Wang, T. Fujiwara, S. Kodaira, and J. He (2017), Large fault slip peaking at trench in the 2011 Tohoku-oki earthquake, *Nat. Commun.*, 8, 14044, doi:10.1038/ncomms14044.
- Suzuki, K., R. Hino, Y. Ito, Y. Yamamoto, S. Suzuki, H. Fujimoto, M. Shinohara, M. Abe, Y. Kawaharada, Y. Hasegawa, and Y. Kaneda (2012), Seismicity near the hypocenter of the 2011 off the Pacific coast of Tohoku earthquake deduced by using ocean bottom seismographic data, *Earth, Planets Sp.*, 64(12), 1125–1135, doi:10.5047/eps.2012.04.010.
- Takanami, T., and G. Kitagawa (1988), A new efficient procedure for the estimation of onset times of seismic waves, *J. Phys. Earth*, 36(6), 267–290, doi:10.4294/jpe1952.36.267.
- Toda, S., J. Lin, and R. S. Stein (2011), Using the 2011 Mw 9.0 off the Pacific coast of Tohoku Earthquake to test the Coulomb stress triggering hypothesis and to

- calculate faults brought closer to failure, *Earth, Planets Sp.*, 63(7), 725–730, doi:10.5047/eps.2011.05.010.
- Tormann, T., S. Wiemer, and A. Mignan (2014), Systematic survey of high-resolution b value imaging along Californian faults: Inference on asperities, *J. Geophys. Res.*, 119(3), 2029–2054, doi:10.1002/2013JB010867.
- Tormann, T., B. Enescu, J. Woessner, and S. Wiemer (2015), Randomness of megathrust earthquakes implied by rapid stress recovery after the Japan earthquake, *Nat. Geosci.*, 8(2), 152–158, doi:10.1038/ngeo2343.
- Uchida, N., and T. Matsuzawa (2013), Pre- and postseismic slow slip surrounding the 2011 Tohoku-oki earthquake rupture, *Earth Planet. Sci. Lett.*, 374, 81–91, doi:10.1016/j.epsl.2013.05.021.
- Umino, N., and I. S. Sacks (1993), Magnitude-frequency relations for northeastern Japan, *Bull. Seismol. Soc. Am.*, 83(5), 1492–1506.
- Urabe, T., and S. Tsukada (1992), WIN—A workstation program for processing waveform data from microearthquake networks, in *Programme and Abstracts of the Seismological Society of Japan*, 2, 331, Tsukuba, Japan (in Japanese).
- Utsu, T. (1972), Aftershocks and Earthquake Statistics (3) : Analyses of the Distribution of Earthquakes in Magnitude, Time and Space with Special Consideration to Clustering Characteristics of Earthquake Occurrence (1), *J. Fac. Sci. Hokkaido Univ. Ser. 7, Geophys.*, 3(5), 379–441.
- Utsu, T. (1978), Estimation of Parameters in Formulas for Frequency-Magnitude Relation of Earthquake Occurrence: In Cases Involving a Parameter c for the Maximum Magnitude, *Zisin (Journal Seismol. Soc. Japan. 2nd ser.)*, 31(4), 367–382 (in Japanese with English abstract).
- Utsu, T. (1999), Representation and Analysis of the Earthquake Size Distribution: A

- Historical Review and Some New Approaches, *Pure Appl. Geophys.*, 155(2), 509–535, doi:10.1007/s000240050276.
- Vere-Jones, D. (1976), A branching model for crack propagation, *Pure Appl. Geophys.*, 114(4), 711–725, doi:10.1007/BF00875663.
- Waldhauser, F., and W. L. Ellsworth (2000), A Double-Difference Earthquake Location Algorithm: Method and Application to the Northern Hayward Fault, California, *Bull. Seismol. Soc. Am.*, 90(6), 1353–1368, doi:10.1785/0120000006.
- Wessel, P., and W. H. F. Smith (1991), Free software helps map and display data, *Eos, Trans. Am. Geophys. Union*, 72(41), 441–446, doi:10.1029/90EO00319.
- Wiemer, S., and M. Wyss (1997), Mapping the frequency-magnitude distribution in asperities: An improved technique to calculate recurrence times?, *J. Geophys. Res.*, 102(B7), 15115–15128, doi:10.1029/97JB00726.
- Wiemer, S., and M. Wyss (2000), Minimum Magnitude of Completeness in Earthquake Catalogs: Examples from Alaska, the Western United States, and Japan, *Bull. Seismol. Soc. Am.*, 90(4), 859–869, doi:10.1785/0119990114.
- Withers, M., R. Aster, C. Young, J. Beiriger, M. Harris, S. Moore, and J. Trujillo (1998), A comparison of select trigger algorithms for automated global seismic phase and event detection, *Bull. Seismol. Soc. Am.*, 88(1), 95–106.
- Woessner, J., and S. Wiemer (2005), Assessing the Quality of Earthquake Catalogues: Estimating the Magnitude of Completeness and Its Uncertainty, *Bull. Seismol. Soc. Am.*, 95(2), 684–698, doi:10.1785/0120040007.
- Wyss, M. (1990), Changes of mean magnitude of Parkfield seismicity: A part of the precursory process?, *Geophys. Res. Lett.*, 17(13), 2429–2432, doi:10.1029/GL017i013p02429.
- Yamada, T. et al. (2009), Intensive observations using long-term ocean bottom

- seismometers; Cases of off-Sanriku and off-Hitachi, in *Abstracts of the Japan Geoscience Union Meeting 2009*, pp. S149-P011, Chiba, Japan.
- Yamada, T., K. Nakahigashi, A. Kuwano, K. Mochizuki, S. Sakai, M. Shinohara, R. Hino, Y. Murai, T. Takanami, and T. Kanazawa (2011), Spatial distribution of earthquakes off the east coast of the Kanto region along the Japan Trench deduced from ocean bottom seismographic observations and their relations with the aftershock sequence of the 2011 off the Pacific coast of Tohoku Earthquake, *Earth, Planets Sp.*, 63(7), 841–845, doi:10.5047/eps.2011.06.045.
- Yilmaz, Ö. (2001), *Seismic Data Analysis: Processing, Inversion, and Interpretation of Seismic Data*, Society of Exploration Geophysicists.
- Yokota, Y., K. Koketsu, Y. Fujii, K. Satake, S. Sakai, M. Shinohara, and T. Kanazawa (2011), Joint inversion of strong motion, teleseismic, geodetic, and tsunami datasets for the rupture process of the 2011 Tohoku earthquake, *Geophys. Res. Lett.*, 38(7), L00G21, doi:10.1029/2011GL050098.
- Yoshida, Y., H. Ueno, D. Muto, and S. Aoki (2011), Source process of the 2011 off the Pacific coast of Tohoku Earthquake with the combination of teleseismic and strong motion data, *Earth, Planets Sp.*, 63(7), 565–569, doi:10.5047/eps.2011.05.011.